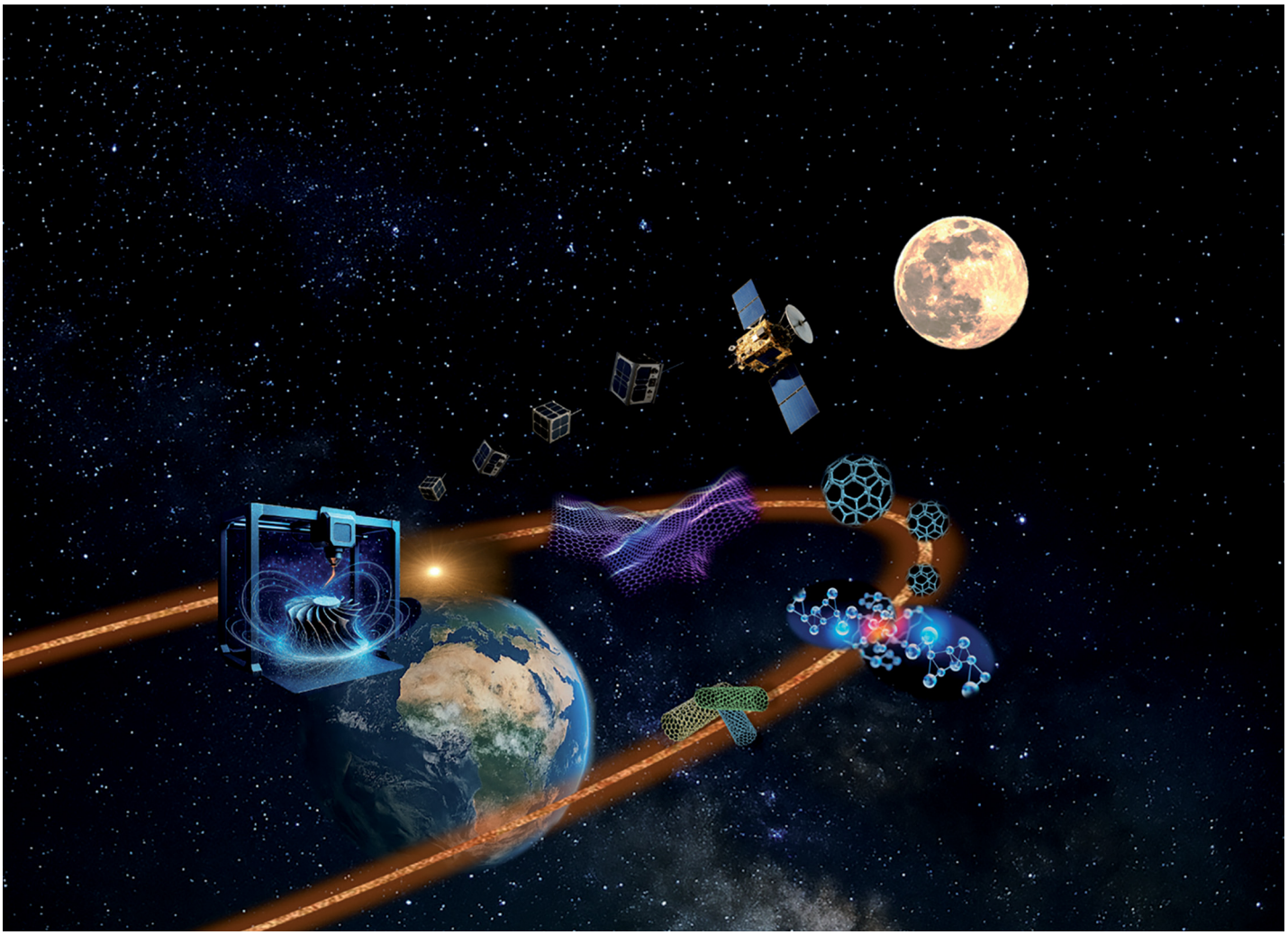

Showcasing a review from Professor Liberata Guadagno's group at the Laboratory of Chemistry for Technology, University of Salerno, Fisciano, Italy

Additive manufacturing of polymers and composites for applications in aerospace and aeronautics

The significant role of additive manufacturing (AM) in transforming the production methods of aerospace and aeronautical real components has been investigated in light of new approaches, such as artificial intelligence and machine learning. The design of composite and nanocomposite smart polymers for "IN-SPACE" and "FOR-SPACE" applications processed *via* different 3D printing technologies has been discussed.

Cover image generated with AI.
Image reproduced by permission of Francesca Aliberti, Liberata Guadagno from *Mater. Horiz.*, 2025, **13**, 532.

As featured in:

See Francesca Aliberti, Liberata Guadagno *et al.*, *Mater. Horiz.*, 2026, **13**, 532.

ROYAL SOCIETY OF CHEMISTRY

rsc.li/materials-horizons

Registered charity number: 207890

Materials Horizons

ROYAL SOCIETY OF CHEMISTRY

REVIEW

View Article Online
View Journal | View Issue

Cite this: *Mater. Horiz.*, 2026, **13**, 532

Additive manufacturing of polymers and composites for applications in aerospace and aeronautics

Francesca Aliberti,*[a] Raffaele Longo,[a] Marialuigia Raimondo,[a] Roberto Pantani,[a] Luigi Vertuccio[b] and Liberata Guadagno*[a]

This comprehensive review emphasizes the significant role of additive manufacturing (AM) in transforming the production methods of aerospace and aeronautical real components. Reducing part assembly and manual interventions and related expenses, together with the possibility of just-in-time production of customised geometry and material-saving structures, are the main reasons for aeronautical interest in 3D printing technology. From a broader perspective, 3D printing allows not only the production of parts on Earth that are intended for deployment in space missions later (FOR-space 3D printing), but also onboard production and maintenance (IN-space 3D printing). New approaches, such as artificial intelligence and machine learning, have emerged as powerful tools for optimized designs, quality control, and process parameter definition, able to consider performance criteria, material properties, and manufacturing constraints. In this context, the present review explicitly examines the working principles, material requirements, and process parameters of prominent 3D printing methods in aerospace and aeronautics, including fused filament fabrication (FFF), direct ink writing (DIW), stereolithography (SLA), materials jetting (MJ), and selective laser sintering (SLS). Particular attention is given to polymeric composites and nanocomposites and their smart functions (*e.g.*, piezoresistivity, piezoelectricity, self-healing, and electro-thermal heating). In addition to these points, one of the main goals of the present review is to analyse the real-world examples from industry leaders such as NASA and Boeing, illustrating practical implementations. Reviewing the industrial advancements makes the reader aware of how much AM technology has been developed on an industrial scale in highly exigent sectors, paving the way to understanding the future trends of research activities. Within this scope, at the end of the review, a comparison of the different technologies, and their advantages and disadvantages is presented together with the future challenges to be addressed.

Received 22nd July 2025,
Accepted 5th November 2025

DOI: 10.1039/d5mh01403d

rsc.li/materials-horizons

Wider impact

3D printing technologies are revolutionizing the ways of producing and processing materials, leading to smart and lean manufacturing and enhancing the quality of customized items with complex and lightweight shapes. In the aeronautical and aerospace fields, additive manufacturing is attracting considerable attention for its versatility in producing nanosatellites, advanced internal parts (*e.g.*, sensors, antennas, and printed electrical circuits), and components for maintenance purposes, thereby minimizing mass, cost, and time. To these "FOR space" applications, the new frontier of "IN space" purposes has been added in the last few years. "In space" 3D printing enables the manufacturing of components directly on board by recycling materials or applying off-Earth resources. In the near future, this approach is expected to revolutionize the manufacturing system for tools used in space missions, leading to a change in the organization and distribution of space on board space shuttles. Considering that aerospace research is the driving force behind numerous scientific and technological advancements in various industrial sectors and daily life, this review highlights the main challenges still to be addressed, providing a cue for forthcoming innovations.

1. Introduction

3D printing is an additive manufacturing (AM) process able to create three-dimensional objects by the addition of building materials layer-by-layer, producing complex geometries and

[a] *Department of Industrial Engineering, University of Salerno, Via Giovanni Paolo II 132, Fisciano (SA), Italy. E-mail: falibert@unisa.it, lguadagno@unisa.it*
[b] *Department of Engineering, University of Campania "Luigi Vanvitelli", via Roma 29, Aversa (CE), Italy*

hollow constructions potentially without material waste, unlike subtractive manufacturing techniques like casting, grinding, milling, *etc.*, which remove bits of the block of metal,[1] plastic,[2] or ceramic[3] material to create the desired item.[4] In the era of digitalization, AM technology is driving the growth of digital fabrication, exploiting the potential of information and communication technologies (ICT), contributing to the so-called fourth industrial revolution.[3] AM processes are based on the interconnection of software, sensors, processors, and communication technologies, whose complex and fascinating study falls within the main topics of Industry 4.0, aiming to create intelligent and interconnected factories that improve efficiency, flexibility, and productivity. Unlike traditional manufacturing processes, in 3D printing, not only the visualization of the product but also the process itself is first conceived in the digital world and then brought into reality, thanks to the preliminary computer-aided design (CAD) and computer-aided manufacturing (CAM) phases. Geometrical information in the form of a CAD model is sent to the slicing software (Standard Tessellation Language .stl file). In the CAM phase, process parameters are set in such a way as to reduce the use of the supporting material, decrease printing time, improve mechanical properties, and avoid deformations, residual stress, and potential defects. The result of the CAM phase is a sequence of instructions (known as "G-code") that defines the machine path. Once the object is printed, post-processing treatments can be performed to improve its mechanical properties or the finishing quality before the final checks. The several steps of 3D printing, generally common to all the techniques, are summarized in Fig. 1. 3D printing of an object does not only mean paying attention to all the process phases, but also choosing the material appropriately.

In most cases, the criteria for selecting materials for 3D printing are precisely dictated by the function that the piece must perform in its field of application.[5] To correctly select the material, it is necessary to know the peculiar characteristics and behavior of all the categories of applicable materials, such as mechanical properties, density, viscosity, rheological, thermal, and electrical properties, and possibly response to UV rays, workability, and response to humidity and chemical exposure.[6] 3D printing materials for aeronautical and aerospace applications are primarily categorized into three types: polymeric, ceramic, and metallic.[7–12] Often, these materials are not used in pristine composition. The vast demand for lightweight and high-performance engineering materials in the transportation sector (*e.g.*, the automotive and aerospace fields) has driven research activity on composite and nanocomposite materials.[13–15] This review mainly focuses on polymeric nanocomposites processed *via* 3D printing technologies. If on the one hand the possibility to process different classes of materials (such as polymers, metals and ceramics) has boosted the development of a large variety of 3D printing technologies, on the other hand the need for obtaining high-performing 3D printed parts, both in terms of mechanical and functional properties, continuously pushes the scientific research community to broaden the materials catalogue.

Among all the 3D printing technologies reported in Table 1 according to the standard terminology for additive

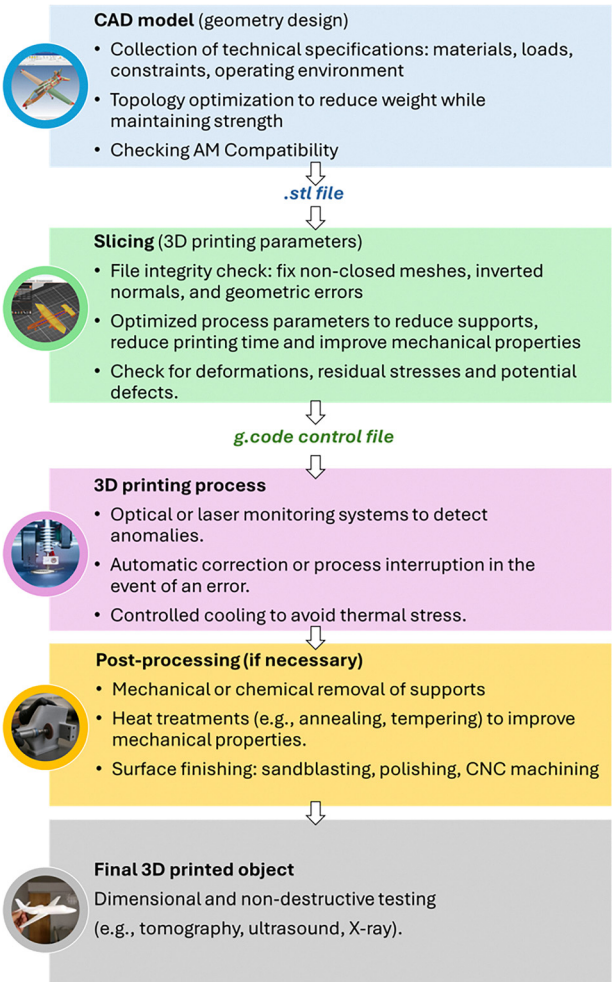

Fig. 1 Scheme of the 3D printing process.

manufacturing Technologies ASTM F2792,[16] Fused filament fabrication (FFF), direct ink writing (DIW), stereolithography (SLA), materials jetting (MJ) and selective laser sintering (SLS) have emerged as the most promising technologies for processing polymeric composites and nanocomposites in the aeronautical and aerospace sectors.[17] Although binder jetting (BJ) can be used with polymeric materials, it is primarily applied to ceramic or metallic powders, with a polymer serving only as a binder between particles.[18] Similarly, although laminated object manufacture (LOM) enables the production of continuous fiber-reinforced thermoplastic composites,[19] in the aeronautical and aerospace sectors, it is primarily applied to ceramic and metallic materials, as evidenced by NASA reports.[12,20] Today, this technology is used mainly to bond metal tapes together through a process known as ultrasonic welding, also referred to as ultrasonic additive manufacturing. For these reasons, BJ and LOM are not discussed in the present review.

1.1. Aerospace and aeronautical industry's interest in 3D printing

3D printing technologies embody the principles of lean manufacturing (LM), among which is the elimination of all

Table 1 Overview of AM technologies and applied materials: bold cells indicate 3D printing processes of polymers suitable for aerospace and aeronautical applications reviewed in this paper. "x" indicates which material (polymeric, metallic, or ceramic) is used for a determined 3D printing technology, both in the research and industrial fields

		Materials		
ASTM F2792 process class	Individual process	Polymers	Metal	Ceramic
Binder jetting	3D Printing	x	x	x
Directed energy deposition	Laser engineered net shaping (LENS)		x	x
	Directed light fabrication (DLF)		x	
	Direct metal deposition (DMD)		x	
Material extrusion	Fused filament fabrication (FFF)	**x**	x	x
	Multiphase jet solidification (MJS)		x	
	Robocasting			x
	Freeze-form extrusion fabrication (FEF)			x
	Direct ink writing (DIW)	**x**	x	x
Material jetting	Multijet/polyjet modeling (MJ/PJ)	**x**		
Powder bed fusion	Laser beam melting (LBM)		x	
	Selective laser sintering (SLS)	**x**	x	x
	Direct metal laser sintering (DMLS)		x	
	Electron beam AM (EBAM)		x	
Sheet lamination	Laminated object manufacture (LOM)	x	x	x
	Plate diffusion brazing (PDB)		x	
Vat photo-polymerization	Stereolithography	**x**	x	x

unnecessary sources of process waste, to reduce costs, improve efficiency, increase flexibility, and maximize the generation of value to customers.[21] Due to the process variability and high product variety, 3D printing cannot be appropriately defined as lean manufacturing yet. To proceed in this direction, it is necessary to bring the AM from formative to large-scale production.[21] As it is continuously spreading in the market, this technology is not far from this goal. According to the statistics of Global Market Insights, the industrial 3D printing market size has been valued at USD 17.1 billion in 2024, and the compound average growth rate (CAGR) has been estimated to increase by 24.7% between 2025 and 2034. Currently, the market share of the aerospace and defense sector is higher than 20%. Such interest in 3D printing technologies is mainly due to the following reasons:

• Reduced part assembly and expenses: conventional manufacturing requires putting together numerous intricate parts. In contrast, 3D printing allows for the production of unified structures, minimizing the use of separate components and connectors. As a result, the cost of labor required to assemble those components is reduced, together with the number of tools held in the inventory, and the costs associated with documentation, inspection, and production.[22]

• Fast prototyping and design optimization: 3D printing enables engineers to create and evaluate prototypes, accelerating the testing phase quickly. This iterative approach streamlines the development process, shortening the time needed to improve and finalize components for space applications.[23]

• Small batch manufacturing: 3D printing offers a budget-friendly option for producing low-cost parts in limited quantities, removing the requirement for costly molds or tools that are not practical for small production runs.[22]

• Just-in-time production: components can be fabricated as needed, reducing reliance on large stocks of spare parts. Shipping spare parts could be expensive, and storing them can occupy usable space, necessary for more frequently used components.[23]

• Customized geometries and material-saving structures: 3D printing makes it possible to produce intricate shapes and internal structures that are difficult or unachievable with conventional manufacturing (*e.g.*, injection molding). This capability leads to a low buy-to-fly ratio (the weight ratio between the raw material and the weight of the final component). The result is a lighter component that preserves its efficiency for intended functions. Such complex structures can be obtained with the use of topology optimization algorithms.[22]

Lower mass and expenses, material-saving structures, and just-in-time production even result in a considerable decrease in CO_2 emissions. This list of advantages is limited to the aeronautical sector and to the production of 3D printed objects, thought to be applied to spacecraft. However, in the context of space exploration and operations, the distinction between "FOR space" and "IN space" 3D printing is mandatory. It depends on where and how AM technologies are utilized. The "FOR space" approach exploits the standard additive manufacturing processes to create parts on Earth that are intended for deployment in space missions later. In this case, the primary concern is to ensure that the 3D printed part has a suitable material and design to endure extreme environmental conditions like intense radiation, severe temperature changes, and physical stress. On the contrary, "IN space" 3D printing is revolutionizing how goods are produced and resources are utilized beyond Earth.[24] It means producing components within the space environment, in microgravity, and on demand. In this case, at least two other advantages have to be considered:

• Onboard production and maintenance: equipping spacecraft and space stations with 3D printers allows for the fabrication and repair of parts directly in space. This is a crucial advantage for extended missions, as it minimizes dependence on Earth-based resupply for essential components.

• Enabling future space settlement: 3D printing is expected to play a key role in supporting human colonization of the

Moon, Mars, and other celestial bodies by allowing the construction of shelters, equipment, and infrastructure using materials found on-site.

''IN space'' production is driving innovation both in the process field and materials science. New recycling technologies on board have been experimented with to reduce the need for new sources and material waste, as well as the exploitation of materials from space itself, a concept known as in-space resource utilization (ISRU), introduced by NASA. In addition, the simultaneous development of microgravity additive manufacturing and robotic precision assembly led to the construction of Archinaut, the first free-flying system developed by NASA in collaboration with Made In Space, Inc., able to construct and assemble all functional elements of a space habitat. Finally, in a broader context, it has the potential to facilitate the on-site production of food and medicine, allowing extended space missions to support human life independently of resupply missions from Earth.[24] All these aspects contribute to significantly lowering payload mass and associated launch costs.

1.2. Design strategy of 3D printed parts in aerospace and aeronautics

The aerospace industry demands lightweight, high-performance materials capable of withstanding extreme environmental conditions. Traditional manufacturing methods limit design flexibility, while AM offers enhanced capabilities for design optimization, including weight reduction, structural integrity, and aerodynamic efficiency. Through computational tools, topology optimization, and lattice structures, engineers can create complex, high-performance geometries that endure the stresses of flight. AM also allows for integrated functional features, reducing the need for assemblies and simplifying production. However, AM introduces new design constraints, such as building orientation, support structures, and material compatibility, which must be addressed early in the design process. Tools like finite element analysis (FEA) and iterative simulations help validate and refine designs.[25] W. M. Van Den Brink *et al.*[26] developed a novel method proposed for continuous fiber reinforced 3D printed design using the finite element approach. The thermoplastic and the fiber are meshed independently and are combined using numerical algorithms. From the independent meshes, the local element stiffness response is calculated, and the stress, strain, and deformation of the components can be predicted. The approach is very flexible; the fiber mesh can be adjusted independently so that the local reinforcement design can be changed and optimized. The mechanical properties of the fibers, thermoplastic material, and layer adhesion are calibrated using test data at the coupon level.[26] Maintaining consistent quality, including minimizing defects like porosity and warping, is critical. This requires advanced monitoring systems and strict process controls.

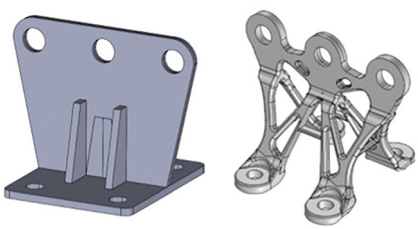

Fig. 2 Examples of original and optimized designs of 3D printed parts: aerospace bracket. Adapted with permission from ref. 30. Copyright 2021 MDPI.

Furthermore, aerospace AM parts must undergo rigorous certification by regulatory bodies (*e.g.*, FAA, EASA), involving standardized testing, material databases, and demonstrated traceability.[25] The challenge for designers is to harness the full potential of additive manufacturing to create parts that not only satisfy user requirements but also offer added value for manufacturers. In this regard, design for additive manufacturing (DfAM) is essential, as it provides the framework for developing high-quality, cost-effective components that meet functional demands while aligning with the specific constraints of AM technologies. However, the lack of comprehensive knowledge, tools, design rules, processes, and methodologies tailored for AM remains a significant technical barrier to its widespread adoption across the industry.[27] The design strategy for 3D printed parts involves the following points:[28]

- Strategy for geometry: topology optimization (part size, thin sections, geometrical features, such as fillets, sharp edges, sharp angles, and narrow holes) and parameter optimization (support structures, building orientation, path planning; printing speed, and layer thickness);
- Strategy for quality (distortion, shrinkage and warping, surface finish, stability, and post-processing);
- Strategy for materials (type of material, mechanical properties, printing object with multiple materials, such as combining rigid and flexible materials);
- Strategy for sustainability (part cost, energy consumption, environmental condition resistance).

To these, standardization, prevention of corrosion, recycling, durability, thermal stability, heat dissipation, and maintenance are added.[29] Yisheng Chen *et al.*[30] designed a 3D printed lightweight aerospace bracket optimized for fatigue performance using topology optimization. A CAD-reconstructed model was created to meet fatigue testing requirements and avoid stress concentration (see Fig. 2a). By applying a multi-load case optimization approach and parameter sweeping, the new bracket achieved a 37% mass reduction. Both simulations and physical fatigue tests validated the design, demonstrating that combining topology optimization with additive manufacturing is effective for developing lightweight, fatigue-resistant aerospace structures.[30] The principles of DfAM were adopted by Airbus, which optimized the Eurostar E3000 satellite.[31] The newly designed 3D-printed bracket can be up to 35% lighter and potentially 40% more rigid than the conventional versions.[31] Additionally, it is produced as a single, unified piece, eliminating the need for a complex assembly that previously required multiple aluminum parts and as many as 44 rivets.[31] Another example is the lightweight, optimized steel node created by the R&D team at Arup, a global engineering

consultancy.[31] This design showcases both geometric optimization and a significant reduction in material waste, achieving a mass decrease of over 40%. Similarly, the antenna support designed and manufactured in Europe for the Sentinel-1 Earth-observation satellite showed a mass reduction of 56%.[31] Advanced software based on bio-inspired design, multi-objective optimization, and thermo-mechanical analysis addresses challenges like thermal distortion and unsupported features.[32] An essential avenue for further study involves the incorporation of AI and ML algorithms within the design optimization process. These technologies offer the potential to automate design workflows, reducing manual intervention, and are also able to generate optimized designs based on performance criteria, material properties, and manufacturing constraints. They adapt dynamically to evolving design requirements and restrictions. Advanced computational techniques can enable intelligent systems that learn from data and iteratively improve design outcomes, leading to more efficient and functional printed products.[33]

D. Goto *et al.*[34] optimized the geometry of stiffeners through curvilinear 3D printing to improve resistance to buckling using a machine learning approach. Inspired by the structure of spider webs, a composite skin-stiffener design was developed. A dataset was created for regression analysis, capturing buckling stresses across varying design features. Using this dataset, deep neural networks were trained to generate regression models. These models were then integrated with sequential quadratic programming, an optimization technique, to identify the ideal values of design parameters that would maximize the ratio of buckling stress to stiffener volume. The optimized design demonstrated a notable enhancement in buckling performance, achieving approximately 163% higher buckling stress compared to traditional straight-stiffener structures of equivalent weight. The machine learning (ML) approach can be exploited not only for design optimization but also for quality control and process parameter definition. R. D. Sajjad *et al.*[35] in their study integrated ML and 3D printing to develop a user-friendly graphical interface (GUI) that predicts printing quality based on input parameters—without requiring actual printing. This approach reduces material waste and pre-print preparation time. The authors created a dataset of 224 samples using nine CAD designs printed at varying temperatures (15–40 °C) and pressures (5–30 psi). They introduced a novel ''complexity index'' to quantify design intricacy and developed four custom labeling methods to compare printed outputs with CAD images. Eight ML models were trained and optimized, with gradient boosting regression achieving the best performance (R^2 = 0.954) in predicting print outcomes. Yang Yuan *et al.*[36] demonstrated that the Kriging and Cuckoo search (CS) algorithm was able to predict the correct combination of process parameters in the FFF process to improve the mechanical properties of 3D printed polylactic acid (PLA) parts. Through experimentation and modeling, the samples printed using optimized parameters achieved a tensile strength improvement (~12.7%) over average values, demonstrating how process parameter optimization enhances mechanical performance, which is highly relevant for aerospace-grade polymer components. K. Garanger *et al.*[37] proposed integrating specifications directly into the manufacturing process using semantic annotations of AM files. The authors introduced the idea of embedding semantic layers in 3D printing files. These layers contain material specifications and control laws that guide the manufacturing process. The semantic layer enables real-time monitoring and feedback control. The system can adapt build parameters on-the-fly to correct deviations during printing. This allows the printed part to evolve dynamically to meet global specifications. Current approaches often rely on open-loop ML models, which are limited to predicting part properties without offering any quality control. S. T. Tariku *et al.*[38] introduced a novel approach that combines both open-loop and closed-loop ML models to monitor and optimize the influence of processing parameters on part quality. Using experimental 3D printing data, an open-loop classification model is developed to map the relationship between processing parameters and resulting part characteristics. Building on this, a closed-loop control system is created by integrating the open-loop ML model with a fuzzy inference system, enabling the generation of optimized processing parameters. This integrated system marks a significant step toward implementing effective closed-loop control in additive manufacturing. A wider range of ML approaches applied to 3D printing is considered by G. D. Gogh *et al.*[39] and I. Rojek *et al.*[40] in their review. In light of the great potentialities offered by AM technologies in the aeronautical and aerospace sectors, the present review discusses the most used 3D printing methods and the advancement of materials science in these fields. Based on Scopus research, selecting 3D printing, polymer*, aeronautic, aerospace, polymer nanocomposite*, automotive, and additive manufacturing as keywords, only a few review articles appear (55 from 2016 to 2024) (see Fig. 3). Although real cases of 3D-printed polymeric components produced by global leaders in aerospace and aeronautical fields (*e.g.*, NASA, Boeing) have been occasionally cited in different articles, a list of them is still missing. Fig. 3 shows that the aerospace and aeronautical sectors have been considered as application fields together with other sectors (*e.g.*, biomedical, construction, and energy) by a total of 46 reviews. However, among them, only 12[22,31,41–50] are strictly dedicated to the aerospace and aeronautical sectors (red bars in Fig. 3). In addition, 9 reviews are focused on the automotive sector. Reviewing the industrial advancements makes the reader aware of how much AM technology has been developed on an industrial scale in highly exigent sectors. This gives an idea of the technology levels reached until now and paves the way to understanding the possible evolution in these fields. Herein, firstly, the main material categories (*e.g.*, thermoplastics, thermosettings, elastomers, composites, and nanocomposite materials, including smart polymers) are introduced. Then, the most used AM technologies are presented in terms of working principle, process parameters, and the suitable materials properties. For each AM method, 3D-printed polymeric components applied in aerospace and aeronautical sectors are described. At the end of this review, the advantages and

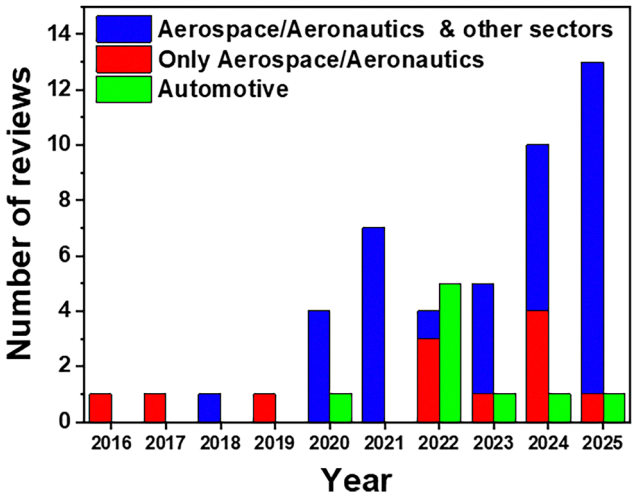

Fig. 3 Number of published reviews per year considering the following keywords: 3D printing, polymers, aerospace sector or aeronautical sector, or automotive sector by Scopus.

disadvantages, challenges, and future trends emerging from the comparison among the different AM technologies are discussed.

2. Polymeric materials in 3D printing processes

Polymers represent the most commonly used material group in AM due to their ease of processing, affordability, and the broad spectrum of adjustable mechanical, thermal, and electrical characteristics that can be tailored through their chemical composition. Additionally, they can be easily modified by blending or incorporating additives and fillers.[51] Polymeric materials are categorized into three distinct classes based on the impact of temperature on their chemical structure and mechanical properties: thermoplastics, thermosets, and elastomers. A brief description of these classes of pristine materials has been reported below, while the schemes of their chemical structures and the typical mechanical properties are schematized in Fig. 4.

2.1. Thermoplastic matrices for 3D printing

Thermoplastic polymers are characterized by long carbon-based chains that stay together thanks to weak chemical interactions between pendant functional groups decorating them. Macromolecular chains can be organized in the amorphous phase, characterized by a disordered arrangement, and the crystalline phase, consisting of ordered structures (crystals). In amorphous thermoplastic materials, no crystals are present (Fig. 4a), and by increasing the temperature above the glass transition temperature (T_g), the polymeric chains constituting the amorphous phase pass from a rigid behavior (glass state) to a soft one (rubber phase), gaining higher mobility. Amorphous polymers become processable in the viscous state at approximately 20 °C above the glass transition temperature.[52] In the case of semi-crystalline thermoplastic materials, both the amorphous phase and crystals are present (Fig. 4a). When the amorphous phase starts to soften near the glass transition temperature, crystals do not soften. Chains that compose crystals start to unfold only gradually near the melting temperature. Since no chemical bonding occurs among the chains, the fluidification of thermoplastics is an entirely reversible process.[53] Chemical bonds within macromolecular chains can be destroyed only at very high temperatures, resulting in degradation. In the detailed case of AM technologies based on material extrusion (*e.g.*, FFF and DIW), macromolecular degradation could also occur due to the combined effect of shear stress and high temperature, that is, thermo-mechanical degradation. While this phenomenon is well studied in

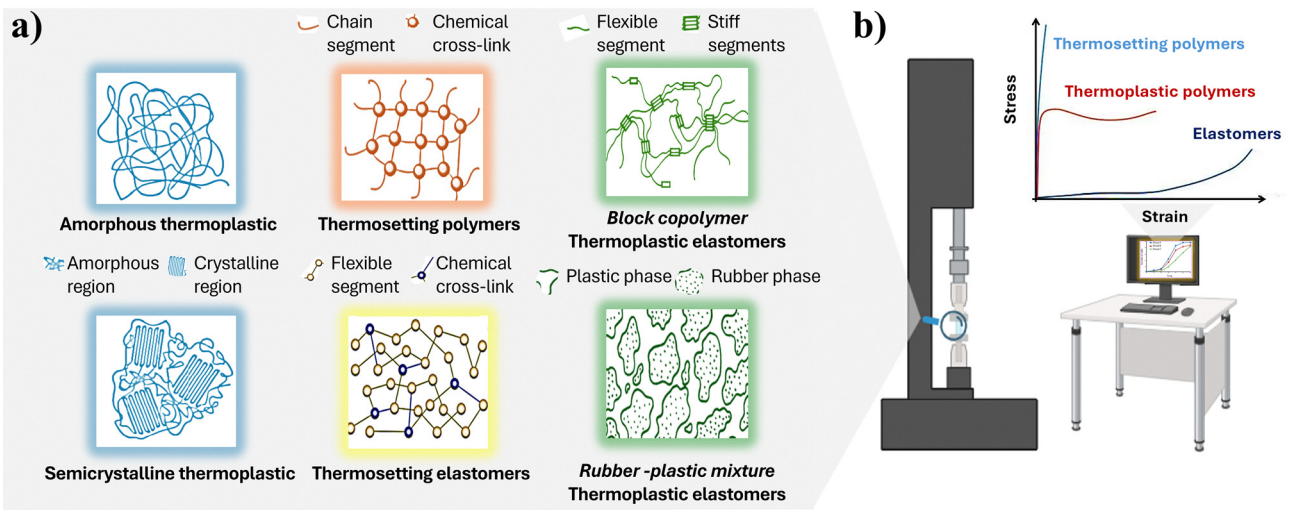

Fig. 4 (a) Schemes of chemical structures of amorphous and semi-crystalline thermoplastic polymers, thermosetting polymers and elastomers, and thermoplastic elastomers (block copolymers and rubber–plastic mixture); (b) typical stress–strain curves of thermosetting and thermoplastic polymers and elastomers (TPE).[65–67]

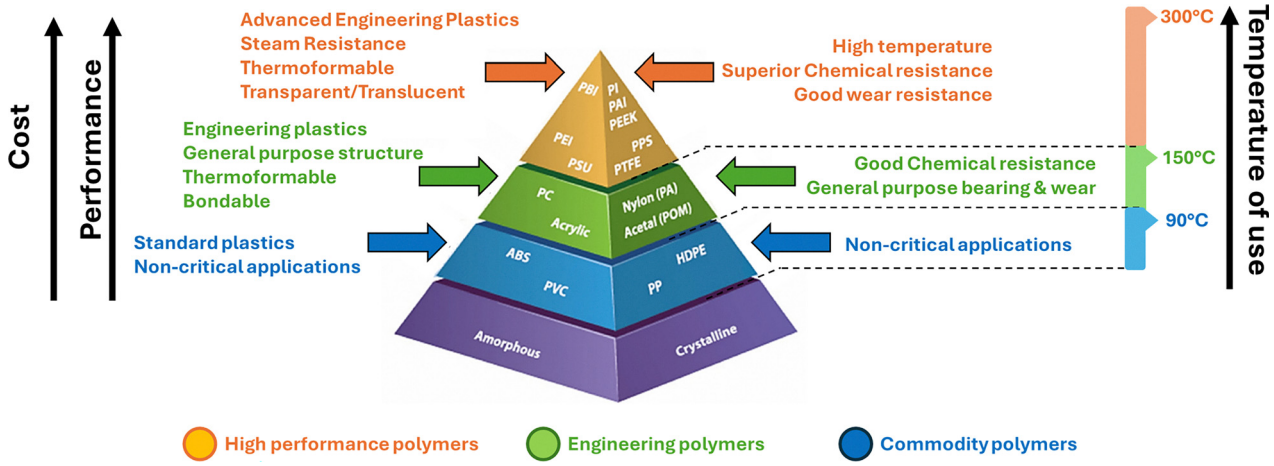

Fig. 5 Classification of thermoplastics based on temperature and performance.[81]

conventional processing (*i.e.*, compression/injection molding), in AM it still needs to be deeply investigated. Degradation phenomena during AM are well reviewed by D. V. A. Ceretti *et al.* in their work.[54] Since thermoplastics represent a broad category of materials, they are commonly classified according to their temperature of use, on which the cost and the performance depend, as illustrated in Fig. 5. In the field of 3D printing, polylactic acid (PLA),[55] acrylonitrile butadiene styrene (ABS),[56] and high-density polyethylene (HDPE)[57] are the most used commodity plastics, while polycarbonates (PC),[58] polyamide or nylon (PA),[59] polyphenyl sulfone (PPSF),[60] polymethyl methacrylate (PMMA)[61] and polyethylene terephthalate glycol-modified (PETG)[48] belong to engineering materials widely employed in the AM process due to their associated properties such as toughness and strength, UV stability, good chemical resistance, and high fatigue resistance along with the high impact strength.[62,63] Engineering polymers are superior to commodity thermoplastics when the application needs higher mechanical strength, elevated temperature tolerance, chemical stability, and resilience against specific mechanical and environmental conditions.[64] Their improved performance, therefore, denotes higher expenses and a decrease in both the volume and variety of production.

It is worth noting that these enhanced properties make engineering thermoplastics suitable for applications in structural elements, bearings, and wear-related uses. In contrast, commodity thermoplastics remain limited to non-structural applications because they do not meet the mechanical requirements necessary for load-bearing structures.[68] However, to improve the performance of commodity thermoplastics as well as their 3D printability, polymer blending is a common strategy, even when it is desired to combine properties derived from two or more different polymers or to avoid defects in the final object.[58,69–71] At the summit of the pyramid represented in Fig. 5, there are high-performance polymers (HPPs) characterized by an extended working temperature range, high chemical resistance, and notable tensile stress enhancements. These superior qualities imply their elevated cost. Polytetrafluoroethylene (PTFE),[72] polyether ether ketone (PEEK),[73] polyetherimide (PEI),[74] Ultem 9085,[75] which is a thermoplastic blend of PEI and PEEK, acrylonitrile styrene acrylate (ASA),[76] and Nylon 12[77] belong to the category of HPPs usually applied in 3D printing for the aerospace sector. Indeed, this last category of thermoplastic materials is the best candidate for application in the aeronautical and space industries due to their outstanding performance. In addition to their mechanical properties, HPPs are suitable for cabin interiors due to their high chemical and thermal resistance, as well as their flame retardancy and low smoke emission. In this way, these materials comply with fire safety regulations and ensure passenger reliability.[78] In the last few years, the ablation performances of 3D-printed HPP materials, such as PEEK, Ultem, and PEI, have been investigated for use as thermal protection systems for spacecraft.[79] Thanks to the availability of polymers of this type, the use of AM-produced products in aircraft has become widespread, as illustrated clearly in Fig. 6.

Thermoplastic polymers are primarily used in FFF, SLS, and DIW technologies because they can be melted multiple times or dissolved in specific solvents.

2.2. Thermosetting matrices for 3D printing

Thermoset materials form from a mixture of monomers or precursors and hardeners, both of which contain functional groups that can react with each other. The polymerization reaction forms a high-density crosslinking network composed of covalent chemical bonds throughout the entire material (Fig. 4a). It follows that thermosets are amorphous polymers. Since there are no chains packed into crystals by increasing the temperature, thermosets undergo only the glass transition temperature (from glass to rubber phase), but no melting occurs. If the temperature rises to high values, thermosetting polymers directly degrade, breaking the chemical bonds.[53,80] Thermosetting can be processed only in the form of an uncured mixture before polymerization starts.

To overcome the issue related to the conventional recycling process (mechanical[82] or thermochemical recycling[83]) a lot of

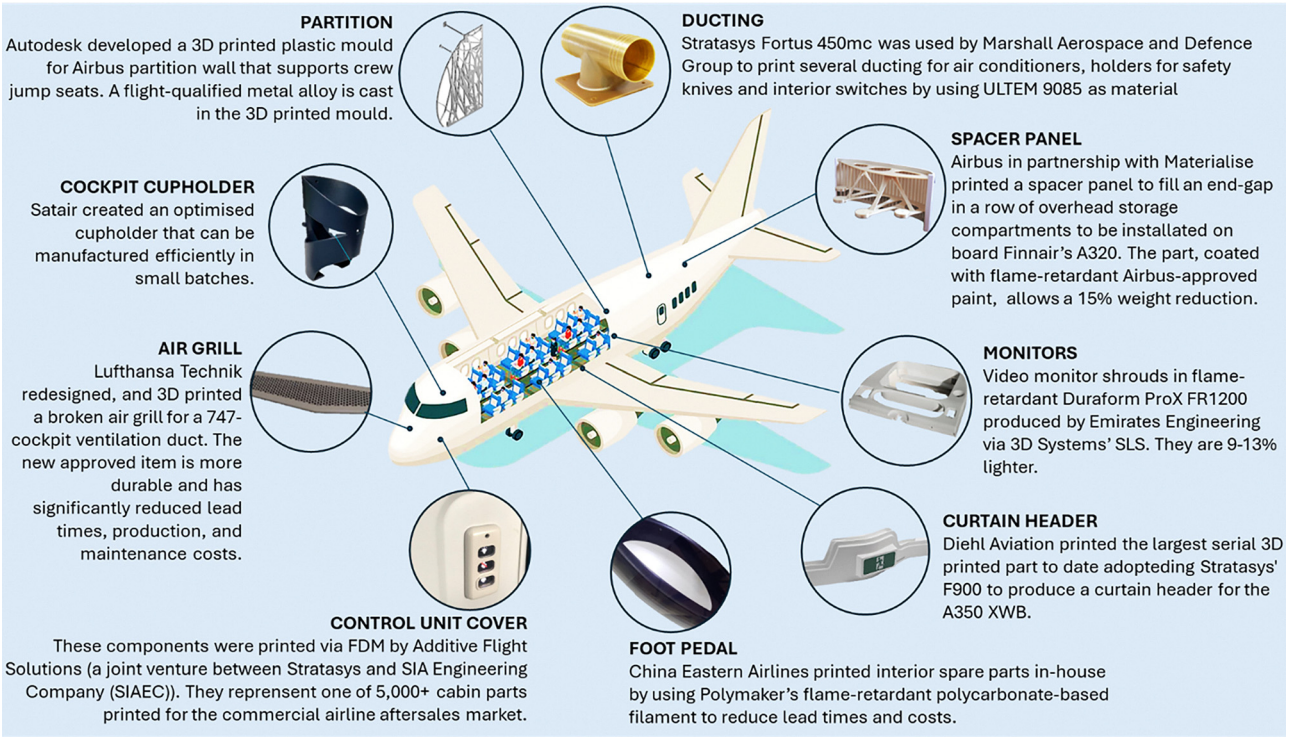

Fig. 6 AM-produced products used as components in aircraft.[100]

research activity is currently focused on new recycling processes[84–86] and on designing a new chemical structure to make thermosetting resins recyclable,[86–88] such as a dynamic-covalent resin (*e.g.* covalent adaptive network CANs),[89,90] vitrimers and self-healable thermosets,[91–93] not only to avoid using solvents or complicated procedures, but also to ensure material quality after recycling or to prolong the lifetime and reduce maintenance costs.

Since thermosets can be processed only once, starting from a monomer mixture, SLA, MJ, and some categories of DIW technologies are the most commonly used 3D printing processes for this type of polymeric matrix. However, there is no shortage of attempts to extend thermosets to the extrusion-based techniques (*e.g.*, FFF) by experimenting with composite vitrimer-containing epoxy inks, whose rheological properties can be adjusted by adding modifiers such as nano-clay[94] or graphene oxide (GO).[95] The majority of thermosetting resins used in 3D printing technology are cured with a light source (UV or laser); for this reason, raw thermosetting materials are often photopolymers (also called photoresins). Photopolymerization offers several key benefits compared to traditional polymerization methods, including lower energy usage, minimal material waste, rapid curing times, and reduced reaction temperatures.[96] Photopolymerization may occur through two different mechanisms: radical photo polymerization and cationic photoreaction, depending on the uncured mixture composition. It consists of three steps: generation of radicals, initiation, and propagation. During the first step of radical photo-polymerization, the photoinitiator absorbs the energy from the light source of the 3D printer to form reactive radical species, which induce the initiation of photopolymerization.

In cationic photoreaction, the initiator is a thermally stable molecule that decomposes under an energy source to form a mixture of cations or radical cations.[51] Typically, photoinitiators are classified into two types: type I and type II. Type I photoinitiators consist of individual molecules that generate radical fragments through cleavage upon light exposure. In contrast, type II photoinitiators involve a sensitizer molecule that absorbs light and a co-initiator (or synergist); when energized, the synergist transfers a hydrogen atom to the excited sensitizer, leading to radical formation.[97] The patented and commercially available photoinitiators are summarized in Table 2, and the choice mainly depends on the characteristics of the 3D printer energy source (*e.g.*, wavelength). Bagheri *et al.*[98] reviewed photoinitiators based on their light absorption properties. As regards monomers, acrylates and epoxides are most commonly used in the industrial field for photocuring. To ensure a high final quality of photocured acrylate resin, Murphy *et al.*[99] in their patent suggested mixing acrylate with methacrylates (*e.g.*, viscosity oligomeric diacrylate or dimethacrylate in liquid acrylate or methacrylate) because acrylates alone cause distortion problems, while methacrylates cure too slowly. To improve the mechanical properties, urethane-acrylates and DGEBA (bisphenol A diglycidyl ether) are often combined.[51] In cases where the chosen monomers have high viscosity, reactive diluents can be added. Although acrylates have the advantage of fast curing, they suffer from the problem of substantial shrinkage during the process. On the contrary, epoxides show less shrinkage (2–3% volumetric) than acrylates.[51]

Table 2 Photoinitiators and monomers used in energy-assisted 3D printing technologies. Chemical structures are shown by S. C. Ligon *et al.*[51] and A. Bagheri *et al.*[98] in their works

Photoinitiator		Monomers				
Type I	Type II	Acrylate	Epoxide	Hybrid acrylate/epoxy	Vinyl-ether	Oxetanes
D1173	Tertiary amines with at least one alkyl substituent	Urethane-D(M)A	DGEBA	GMA	CDVE	DSO
I184		DEGEBA-D(M)A	ECC	ECMA	TTVE	
TPO		DPGDA*	VCDE			
I651		TTA*	ESBO			
I369		PETA*	CPDE			
BAPO		DCPDA*	Polyols			
Ivocerin		TAEI*	DSO			

This class of monomers has gained more interest in the aerospace and aeronautical sectors due to their higher T_g value and mechanical properties compared to acrylates. Better mechanical properties, increased precision, and a reduced shrinkage rate are all benefits provided by epoxy-based resins.

The molecular architecture, which is influenced by the concentration of the photoinitiator, the composition of the monomers, and the curing conditions, is intimately linked to the mechanical behavior of thermosetting polymers. Commonly, epoxides cure *via* cationic chain growth, which leads to a high number of cross-linking points along the polymer backbone, increasing both the mechanical modulus and the brittleness of these materials.[51] However, their disadvantage is slower kinetics; thus, a prolonged light-time exposure is necessary for polymerization to cure.[101] Consequently, to increase their rate of polymerization, the majority of epoxy-based resins also contain acrylate monomers in their composition.[102] Monomers characterized by functional groups involved in diverse curing reaction mechanisms are often mixed.[103–105] Since epoxides and acrylates could undergo different reaction mechanisms, the result would be an interpenetrating network (IPN) rather than a copolymer.[23] Together with the main photoinitiators, monomers used in energy-assisted 3D printing technologies are listed in Table 2, and their molecular structures are shown by S. C. Ligon *et al.*[51] and A. Bagheri *et al.*[98] in their works.

2.3. Elastomeric matrices for 3D printing

Elastomers represent the third class of polymers. Typically, elastomers are above their T_g at room temperature, since they generally manifest a T_g in the range of −50 to −70 °C. The main peculiarity of elastomers is their high extensibility (up to 1000%) (Fig. 4b), from which they recover rapidly as soon as the applied stress is removed. Once again, the macroscopic behavior of the material depends on its chemical structure (Fig. 4a). The high stretchability and the capability of strain recovery are due to the fact that elastomers are composed of macromolecules held together by a few and distributed covalent bonds, in the case of thermosetting elastomers (TSE), or physical links in thermoplastic elastomers (TPE). In TSE, chemical cross-links are introduced into the materials through the vulcanization process, making them challenging to reprocess and recycle, similar to thermosetting materials.

In TPE, physical links are due to a block copolymer structure or rubber–plastic mixture[53] (see Fig. 4a). Both in the case of covalent bonds and physical bonds, these knots in the structure facilitate recovery after the stress is removed. TPE may be characterized by two softening temperatures (T_s), one for the flexible blocks or soft phase and another for the stiff blocks or stiff phase. Above the T_s of the hard phase, the reinforcing action of this phase disappears, and TPE materials become processable. Upon cooling, the mechanical behaviors of TPE are restored.[53] Additively manufactured elastomers offer promising applications in flexible parts such as built-in shock absorbers, ergonomic grips, living hinges, integrated seals, and other components that rely on the distinctive flexibility and resilience of elastomeric materials.[106] In the aeronautical and aerospace sectors, they offer the possibility to improve strength and weight efficiency in structural components, for increasing the reliability of aerospace gaskets and seals, for overcoming issues with vibration dampening,[107] as adhesives for flexible connections, and for preventing extreme temperatures, as well as for advancement in smart materials.[108] In the field of 3D printing, elastomers are commonly applied in FDM, SLA, and SLS technologies.[109] However, since they can behave like thermoplastics (TPE) or thermosets (TSE) from a thermal point of view, some examples of elastomers in DIW and MJ are also documented in the literature. Setter *et al.*[110] exploited the potential of MJ technology to combine a TSE acrylate-based photopolymer with TSE polyurethanes in the same device, investigating the bonding strength between the two phases. Currently, Tango Plus, Ninja Flex, PRO Series Flex, Poly FlexTM, and styrene–butadiene rubber (SBR) are the rubber-like and copolymeric elastomers available on the market for 3D printing.[109] The complete list of commercial elastomers for 3D printing is reported by Herzberger *et al.*[111] However, research on the development of new elastomers continues to progress, aiming to enhance mechanical performance, melt processability, and recyclability.[112] Three classes of elastomers suitable for 3D printing, whose characteristics are reported in Table 3, can be distinguished: silicon elastomers, polyurethane elastomers, and liquid crystalline elastomers (LCEs). Silicon polymers—also known as siloxanes or silicones—are built from repeating -Si(R)$_2$O- units, with many of their distinctive properties arising from the unique chemistry of the silicon–oxygen (Si–O) bond. Silicon elastomers are relatively low-cost and retain their mechanical and electrical characteristics across a

Table 3 Different categories of elastomers and their characteristics

Category	Characteristics	Ref.
Silicon elastomers	• Biocompatibility • Optical transparency • Resistance to chemical agents • Electrical insulation • No-flammability • Non-UV absorbing • Low surface tension • Water impermeability • High oxygen permeability • Low elastic modulus • Ultimate strains above 300% • Broad operative temperature, from approximately −50 °C to +300 °C	109, 111 and 127
Polyurethane elastomers	• Stable up to around 80–120 °C • Excellent thermal insulation (thermal conductivity typically between 0.02 and 0.03 W m^{-1} K^{-1}) • High resistance to oils, solvents, and oxidation • Tunable mechanical properties according to soft segment (SS) oligomer type and hard segment (HS) content	111
Liquid crystalline elastomers	• External stimuli responsiveness due to the liquid crystal phase to the isotropic phase transition • High energy dissipation capability	128

broad temperature spectrum, from approximately −50 °C to +300 °C. However, using them at temperatures below −50 °C becomes problematic due to the crystallization behavior of polydimethylsiloxane (PDMS), which tends to crystallize between −75 °C and −100 °C and melt near −50 °C. They are covalently crosslinked networks composed of polysiloxanes.[111]

TPU is synthesized through the reaction of polyols (which may be polyester-, polyether-, or polycarbonate-based), diisocyanates, and short-chain diols. Typically, the soft segment originates from the polyol component, while the hard segment is formed by the combination of a diisocyanate and a chain extender. Thermally, flexible TPUs are stable up to around 80–120 °C, while some rigid variants can withstand temperatures up to 150 °C. In its foamed form, polyurethane provides excellent thermal insulation due to its low thermal conductivity, typically between 0.02 and 0.03 W m^{-1} K^{-1}. It also offers good resistance to oils, solvents, and oxidation, although its hydrolysis resistance varies with the type of polyol used. TPU is known for its durability, maintaining performance under mechanical stress, weather exposure, and fatigue. It is highly processable, suitable for molding, casting, spraying, and 3D printing in both thermoplastic and photocurable forms. Polyurethane adheres well to various substrates, and its surface can be modified to enhance specific properties. Additionally, medical-grade formulations of PU are biocompatible, making them suitable for use in healthcare applications.[113,114]

LCEs are lightly crosslinked, flexible polymer networks that incorporate liquid crystalline mesogenic units along either their main chains or side chains. These materials uniquely blend the structural order and dynamic behavior of liquid crystals with the elastic, deformable nature of rubber-like polymers.[111] They demonstrate reversible changes in their mechanical and optical behavior when transitioning from a liquid crystalline phase (such as the nematic phase) to an isotropic phase, triggered by external stimuli like temperature, light, or electric fields.[111] The capability to fabricate LCEs in three dimensions through additive manufacturing is particularly appealing for the development of artificial muscles, soft actuators and robots, sensors, advanced medical devices, and adaptable functional structures.[115]

Elastomers have attracted the attention of Boeing and NASA in the development of morphing structures, where an elastomer skin is used to bridge the span-wise gap between the flap and wing.[116,117] Although elastomers allow for better interlayer adhesion than common thermoplastics in extrusion-based AM technologies (*e.g.*, FFF), the main challenge is the high pressure required to push them out of the nozzle. This is because TPE elastomers exhibit high viscosity due to their peculiar chemical structure and low elastic modulus, resulting in filament buckling in the nozzle.[118] To overcome this process limitation, TPE could be blended with a common thermoplastic,[119] filled with fibers,[120] or nanoparticles.[121] In addition, high viscosity is also a drawback for TSE used in SLA, energy-assisted DIW, and MJ, causing slower print times or warpage defects. In that case, reactive diluents could be added to the elastomeric mixture.[111] However, elastomers remain particularly suitable for producing 3D-printed lightweight lattice structures for structural health monitoring of aircraft.[122] The addition of carbon nanotubes or other conductive fillers (*e.g.*, graphene) makes elastomers one of the best candidates for developing piezoresistive smart materials for self-sensing applications,[123] as will be clear in the following paragraphs.

Table 4 resumes the advantages and disadvantages of the three classes of polymeric materials, thermoplastics, thermosets, and elastomers employed in aerospace and aeronautical applications.[65,66,85,124]

2.4. Polymeric composites and nanocomposites for aeronautical and aerospace applications

Composites are made by combining two or more different materials to achieve properties that individual materials alone cannot provide. They offer benefits like high strength, stiffness, low thermal expansion, and resistance to harsh environments. The main components of a composite are the

Table 4 Advantages and disadvantages of thermoplastics, thermosets, and elastomers[65,66,85,124]

Materials	Advantages	Disadvantages
Thermoplastics	• Rapid processing	• High viscosity
	• High ductility	• High processing temperature (250–400 °C)
	• High energy absorption capability	• High processing pressure
	• High fracture toughness	• Poor creep resistance
	• High impact resistance	
	• Lower moisture absorption	
	• Recyclability	
Thermosets	• Low processing temperature (up to 200 °C)	• Narrow processing window
	• Low viscosity	• Low ductility
	• Good compression properties	• Low fracture toughness
	• Good fatigue resistance	• Low impact resistance
	• Good creep resistance	• High moisture absorption
	• High resistance to solvents	• Limited shelf life
	• Good fiber wetting for composites	• Not recyclable
		• Poor weldability
Elastomers	• Low processing temperature	• Low processing time
	• High ductility and flexibility	• Poor creep resistance
	• High fracture toughness	• Low Young's modulus
	• High impact resistance	• Low tensile strength

matrix (thermoplastic, thermosetting, or elastomeric one), which binds and supports the reinforcement, and the second phase, which carries most of the load due to its strength and stiffness.[125] According to the dimensions of the reinforcement, it is possible to distinguish continuous fiber-reinforced polymer composites (CFRPs) from polymer nanocomposites (PNCs). Nowadays, composite polymers account for approximately 50% of the overall structural composition of an airplane.[126] CFRPs are made from fibers like carbon, glass, aramid, or natural fibers embedded in a thermosetting matrix. They are preferred over metals for their light weight, fatigue and corrosion resistance, and high strength and stiffness. Glass fibers are cheaper and moderately strong, used mainly in interior aerospace parts, while carbon fibers offer superior strength and stiffness, ideal for primary structures.

However, recycling long carbon fibers is still challenging, often resulting in short, non-woven recycled carbon fibers (rCFs) due to fiber breakage during the recycling process[84] (*e.g.*, mechanical recycling or reactor limitation in solvolysis), with an unavoidable reduction in the mechanical properties of composites based on rCFs.[129] To reduce the environmental impact of CFPs, biobased and biodegradable natural fibers, such as hemp, sisal, jute, and flax, are currently under investigation. Although they are eco-friendly, natural fiber materials in reinforcements come with some critical shortcomings, such as hydrophilicity, poor moisture resistance, and weak fiber/matrix adhesion. But these drawbacks have significant room for improvement using innovative resins, additives, coatings, and surface modification techniques of fibers.[130] Thermosetting CFRPs are widely studied in terms of mechanical performance, traditional and advanced processes, thermal and electrical properties.[2,13,131,132] To remedy the brittle nature, poor resistance to crack initiation, and insufficient toughness of thermosetting CFRPs, even thermoplastic CFRPs have been studied, especially in recent decades.

However, thermosetting CFRPs still account for the vast majority of the composites industry.[133] This is because thermoplastic CFRPs currently do not match the mechanical performance of thermosetting composites, and their manufacturing process is complex. The main challenge lies in effectively impregnating long fibers or nonwoven fabrics with the highly viscous molten thermoplastic matrix. As a result, they are not yet suitable for use in structural or load-bearing applications. To move in this direction, researchers and global leaders in the aerospace and aeronautical sectors consider high-performing thermoplastics (such as poly aryl ether ketone (PAEK), and poly ether imide (PEI)) for fiber composites. Conventional composite fabrication techniques typically depend on high-cost molding tools to shape fiber and resin materials. To mitigate these substantial tooling expenses, large-scale production is often required, which inherently limits economic feasibility for low-volume or customized manufacturing. Additionally, these traditional processes constrain the geometry of the final components, favoring simpler shapes (mostly laminates). The significant investment in tooling presents a considerable barrier to producing complex composite structures or implementing design modifications.

In contrast, AM offers enhanced design flexibility and is well-suited for rapid prototyping and iterative product development.[134] AM technologies for CFRPs are mainly based on preimpregnated (in the case of thermosettings) or pre-extruded (in the case of thermoplastics) fibers. Although there is industrial interest in additively manufactured CFRPs, there are still limitations to overcome before industrialization, which are mainly related to the fiber/matrix bonding or interlayer bonding.[134] Industrial sectors are also investing in PNC materials. Different from CFRPs, where the fiber content is usually around 60%, in PNC materials, the properties can be improved at low filler loadings. This occurs because nanofillers offer a higher surface area than long fibers, leading to a high interface area between the filler and matrix. Nanofillers can be classified according to their dimensional structure: zero-dimensional (0D) fillers, meaning that all three dimensions fall within the 1–100 nm range, like nanosilica or carbon-black; one-dimensional (1D) fillers like nanofibers and nanotubes having two nanometric dimensions; and two-dimensional (2D) fillers, which include nanosheets or nanoplatelets like graphene where only the thickness is nanometric. The capability to form a homogenous network at a nanoscale level strongly depends on the shape and aspect ratio of the nanoparticles, how they are produced (*e.g.*, the purity), and the type of polymeric matrix influencing the interfacial bonding. For example, a larger aspect ratio allows for lower filler content to reach superior performance as a lightweight and flexible electromagnetic shielding material,[135] and a lower content of carbon nanotubes

(1D) is sufficient to increase the electrical conductivity than expanded graphite (2D) in the same matrix.[136] Nanoclay[137] and nanosilica[138] are mainly used to improve flame retardancy and thermal stability, together with mechanical and barrier properties. The inclusion of nanoparticles can improve the barrier properties of the material since the shape, size, degree of dispersion, and especially the type of particle–polymer interaction affect the transport properties of gases.[49] Metal nanoparticles[139] (aluminum or silver nanoparticles) are studied for their high hardness and wear resistance. However, they do not contribute to reducing weight or corrosion issues.

Among nanofillers, carbon-based ones are the most commonly applied, such as carbon nanotubes (CNTs),[140] graphene (GF), graphene oxide (GO),[141] and carbon black (CB),[142] because they could simultaneously improve electrical, mechanical, thermal, and gas barrier properties, and even contribute to reducing the weight. They are also suitable for conferring enhanced photooxidative stability to thermoplastic polymers,[143–145] thereby contrasting the vulnerability of amorphous or semicrystalline thermoplastic polymers, which are susceptible to UV degradation.[146,147] More recently, publications featuring MXenes[148] (atomically thin layers of transition metal carbides, nitrides, or carbonitrides) have increased significantly in 2023 since they refer to materials exhibiting high electron density and electrical conductivity, making them attractive for use in electronics and energy storage applications.[149] Modern aircraft like the Boeing 787 and Airbus A380 face significant challenges in simultaneously achieving strong mechanical properties and effective electromagnetic performance. One critical aspect is shielding against electromagnetic interference (EMI), which involves absorbing and deflecting electromagnetic waves to prevent system disruption. To address this, conductive nanocomposites have emerged as promising materials due to their ability to withstand intense radiation, minimize human exposure, and safeguard structures from lightning. CFRPs also show great potential for use in these protective applications.[126] Although nanoparticle concentration remains usually low (below 1–5% by weight for thermosetting and below 20% by weight for thermoplastics), PNCs face the issue of nanoparticle agglomeration and processing challenges due to increased viscosity also limiting the scalability. Specific studies on polymeric composites and nanocomposites in 3D printing technologies explore various aspects not explicitly related to their application in the aeronautical and aerospace sectors.[2,13,131,132] While significant progress has been made in developing recyclable matrices and recovery techniques for conventional CFRPs, additional research is needed to address the critical challenge of a circular economy for nanocomposites. Physical, thermal, and chemical approaches for thermosets, particularly focused on carbon fiber recovery from CFRPs, become more challenging to apply in the case of PNC, because of nanoparticle agglomeration and surface chemistry preservation at the nanoscale.[150] Comparing CFRPs and PNC, if on the one hand, CFRPs guarantee better load-bearing capabilities; on the other hand, multifunctionality or smart properties are prevalently obtained by using nanofillers. For this reason, long or short fibers impregnated with a nanocomposite matrix are the way to benefit from both types of reinforcements. Peculiar cases of 3D printed polymeric composites and nanocomposites for specific applications in the aeronautical and aerospace sectors will be discussed for each related AM technology in Section 3.

2.5. Smart materials and multifunctional materials

A new generation of smart materials has overcome conventional functional and structural materials. They are so-called because they can change their shape or properties due to external or internal stimuli,[151] such as heat, stress, or pressure, as well as current, voltage, light, pH variation, or a magnetic field. Smart materials can act as a sensor or an actuator, depending on whether they sense or respond to changes in the external environment. Examples of smart materials are strain-sensitive materials,[152] electrorheological, magnetorheological, shape memory materials, self-healing materials, electrostrictive materials, magnetostrictive materials, piezoelectric materials, and electro-thermal heated materials.[153] Moreover, multi-functional materials can be designed by simultaneously combining more than one function, for example, strain-sensing ability for strain detection with shape memory ability to restore the initial shape. The need for thermal management of structural components, structurally capable solar panels, and habitat structures, as well as wear resistance, vibration dampening, radiation shielding, acoustic attenuation, and the potential to create functional components ''IN space'' are the reasons behind NASA's interest in multifunctional materials.[18] The aeronautical and aerospace sectors have mainly focused attention on electro-thermal heating, strain sensitivity, piezoelectric properties, and self-healing.

2.5.1. Electro-thermal heated materials. Electrically conductive polymeric composites can heat up when an electrical stimulus is applied (*e.g.*, power or voltage) due to the Joule effect. Beyond the metals, well known to be excellent conductors, today, polymer composite heating systems are being developed to reduce weight and avoid corrosion problems by predominantly using carbon-based fillers. Heating structures are functional for de-icing purposes, promoting healthy living, mitigating hazards, and industrial processing in the aerospace and aeronautical fields.[154–157] To design nanomaterials suitable for electro-thermal heating, electrical conductivity must fall within the range of 10^{-6} to 1 S m^{-1}. However, pure polymer matrices typically exhibit extremely low conductivity, around 10^{-16} to 10^{-13} S m^{-1}. As conductive filler content increases, the composite's conductivity rises sharply at the electrical percolation threshold (EPT), the point where a continuous conductive network forms, shifting the material from insulating to semiconducting behavior.[158] This transition occurs when the distance between filler particles approaches the ''tunnelling distance'', enabling electron flow. Beyond the EPT, further filler addition leads to moderate conductivity increases, reaching a plateau between 10^{-2} and 1 S m^{-1}. Factors such as polymer type, synthesis method, filler aspect ratio, agglomeration, distribution uniformity, and alignment significantly influence the

EPT and resulting conductivity.[159,160] The lower value of EPT of CNT-nanocomposites than that of EG-based materials is widely documented in the literature; however, it remains difficult to establish which one is the most efficient when the same electrical stimulus and the same electrical conductivity of the nanocomposites are considered. This is because the heating performance is prevalently governed by intrinsic electrical and thermal properties of the filler (susceptible to the production process and the presence of defects), the morphology (semi-crystalline or amorphous), and the molecular weight of the matrix and the degree of intercalation between the filler and macromolecules.[161] In aeronautics, heating structures are functional for de-icing purposes and for new energy-saving processing methods for the production of CFRPs.[162,163] Electro-thermal heating is often combined with super hydrophobicity to reduce friction on runback supercooled water droplets, disfavoring their adhesion on the surface.[164] Developing electro-thermal heated materials is fundamental not only to overcome the current methodology (*e.g.*, anti-icing liquid, pneumatic type) limited by one-shot or land-based use, but also for unmanned vehicles (UAVs), which have a complex structure. Further research is necessary for anti-icing/deicing systems for UAVs, since it is less developed and less widespread than on airplanes.[165] In this last case, the AM technology is much more affordable, as in the case of robotic components, due to the facilitation of the usually reduced dimensions of devices and components.[166,167]

2.5.2. Piezoresistive materials. Resistive-type sensors, also named piezoresistive sensors (PRS), are often nanocomposites in which conductive nanoparticles (mainly CNTs or EG) constitute a conductive network in the insulating polymeric matrix. Any deformation or micro-damage causes interruptions in the conductive network, leading to an increase in the electrical resistance. The electrical resistance value recorded at a macroscale level corresponds to the sum of two contributions at a nanoscale: the electrical resistance faced by the electrons along the conductive nanoparticle (intrinsic characteristic of the filler) and that encountered at the interface between one nanoparticle and the other, namely, tunnelling resistance. When the material is under strain, the contact area and the distance between conductive nanoparticles changes, inducing a variation in the tunnelling resistance, constituting the reason for the strain sensitivity of the material. Moreover, strain sensitivity depends on the filler characteristics (shape, dimension, orientation) and on its concentration.[136] Use of self-sensing materials in 3D printing is wide due to the large number of application fields such as robotics, medicine, civil engineering, automotive, electronics, and wearable electronics. In the specific case of the aerospace and aeronautical sectors, piezoresistive materials are used for structural health monitoring. Monitoring the structural integrity of critical aircraft components such as the fuselage, wings, and cockpit, which are parts regularly subjected to severe environmental stresses, including fluctuating temperatures, bird or hail impacts, and lightning strikes, contributes to improving the aircraft's safety, functionality, and dependability.[168] In this context, 3D printing technologies are useful to the development of sensors with tailored characteristics (*e.g.*, sensitivity to the strain) and adaptable designs[166] overcoming the limitation of traditional inspection techniques.[168,169] However, piezoresistive sensors face performance issues due to their sensitivity to surface conditions and environmental factors. Although research studies on improving the PRS performance (sensitivity, signal-to-noise ratio, resolution, detectable ranges, *etc.*) have been performed, challenges such as damage location, high production costs, limited scalability, and poor reproducibility also hinder their practical use. Similarly, while flexible and stretchable piezoresistive devices have made significant progress in labs, commercial adoption is limited by low reproducibility, particularly difficulties in controlling crack density and depth.[170]

2.5.3. Piezoelectric materials. In the field of structural health monitoring, piezoelectric properties have also been exploited.[171] The piezoelectric effect refers to the capability of specific materials to produce an electric charge when mechanical stress is applied. In contrast, the inverse piezoelectric effect occurs when these materials undergo deformation in response to an electric field. As a result, applying voltage to these materials can cause a structure to bend, stretch, or fold (actuator).[172] Piezoelectric materials (PEMs) are usually made of an active piezoelectric component (made of $BaTiO_3$, lead zirconate titanate (PZT), PVDF (polyvinylidene fluoride)) dispersed into a passive polymer matrix (*e.g.*, epoxy, silicone, PVDF–TrFE), only used to encapsulate, support, or transfer stress to the embedded piezoelectric component. The most common configurations are:[173]

- 0–3 composites: where the first phase (*i.e.*, the ''0'' in ''0–3'') is enclosed in all three dimensions within a continuous matrix. In this case, particles or short fibers of piezoelectric material are dispersed in a polymer matrix.
- 1–3 composites: where the first phase (in the form of a long-fiber and with connectivity in one dimension) is embedded in a matrix that has continuous connectivity across all three dimensions.
- 2–2 composites: laminar structures with alternating piezoelectric and polymer layers in such a way that both phases exhibit connectivity in two dimensions.

To exhibit macroscopic piezoelectric properties, poling is a crucial post-processing step. It is applied to ferroelectric or piezoelectric materials to align their internal random electric dipoles in a common direction and ''activate'' piezoelectricity. Poling typically involves applying a strong electric field to the material under controlled temperature and environmental conditions. Among the traditional poling methods (corona, contact, and thermal poling), the *in situ* poling is experimented in the 3D printing process. Hoejin Kim *et al.*[174] demonstrated the feasibility of *in situ* poling through a high electric field during 3D printing of $BaTiO_3$ in PVDF. For PEMs, there are different modes on which SHM function is based, such as modal analysis, acoustic emission, lamb-wave, and strain-based methods simultaneously by adjusting driving frequencies and sampling rates.[175] K. Johannes and D. Mayer[176] applied networks of piezoelectric patch actuators and sensors

to excite and detect flexural waves across an A320 fuselage element. By comparing undamaged *vs.* artificially damaged states, the developed networks were able to effectively detect cracks as small as 30–60 mm in panels and as small as 10 mm in stringers. In aircraft cabins, wings, or turbine blades, piezo actuators can actively dampen vibrations by generating counter-vibrations. NASA proposed embedded piezoelectric ceramics (Navy Type-II PZT) in the form of monoliths (non-flexible patch) and fibers (flexible patch) into a polymer matrix fiber composite blade material to decrease turbomachinery blade vibration either through a passive damping, or as part of an active vibration control system.[177] From the technical report, it emerges that the main limitation is that embedded piezoelectric elements may have adequate strength for implementation and new methods for reducing interlaminar stresses between the composite and piezoelectric elements should be investigated. Acoustic emission sensors, which are a type of passive piezoelectric sensor, have been applied by Airbus to the wing of an A320 to detect damage earlier than conventional non-destructive test methods. The mechanical energy of vibrations can also be converted into electrical energy for low-power devices (*i.e.*, energy harvesting) directly by piezoelectric materials.[178] As regards aerospace, piezoelectric actuators allow for the precise control of satellites' or micro-thrusters' motion with a fast response time. Piezoelectric material can be used to harvest energy from the surface of an aircraft structure when any force is exerted on the surface.[178] PEMs suffer similar limitations to PRS. For both of them, other open research areas are mainly new integration methods into the hosting structure and infrastructure systems with local AI/ML data-processing.[175]

2.5.4. Self-healing materials. A self-healing material can recover its integrity after damage.[179] In general, this self-responsive functionality makes polymeric materials suitable to mitigate the consequences of debris impact in aeronautical and aerospace applications by properly designing a multilayer composite and/or self-sealing layers in reservoirs.[180–183] To overcome these shortcomings, self-healing materials can be appropriately designed to repair damage initiation and to avoid crack propagation up to spatial scales of micrometres or several millimetres, both in thermoplastic material and in thermosetting composite structures.[181,184–186] In addition, self-healing materials have the advantage of repairing themselves without adding new material, avoiding the increase in weight, prolonging the life of materials, and reducing their maintenance costs, especially in the transport sectors. Three driving factors have boosted the research toward self-healing polymers: extreme environmental conditions, rapid growth of the aviation market, and the need for materials with low environmental impact.[187,188] However, their application in engineering contexts that demand moderate to high mechanical performance is still in its early stages. The lack of end-use is primarily due to stringent aviation standards and a long validation period. Self-healing materials can be classified in two main ways. The first classification is based on the need for external stimuli: autonomous systems heal automatically at room temperature, while non-autonomous systems require external triggers like heat, light, electrical, chemical, or mechanical stimuli. The second classification depends on chemical composition: intrinsic systems heal due to the properties of a single material, whereas extrinsic systems need an added healing agent to enable the repair process.[189] All the mechanisms currently studied of self-healing polymers are summarized in Fig. 7.[190] Shape memory polymer composites (SMPCs), although classified as a self-healing materials, are more devoted to the recovery of deformation (such as bending strain) rather than repairing a crack. The presence of nanofiller in shape memory materials overcomes the limitations of low stiffness, low modulus, and low recovery load. In aerospace structures such as solar arrays, deployable

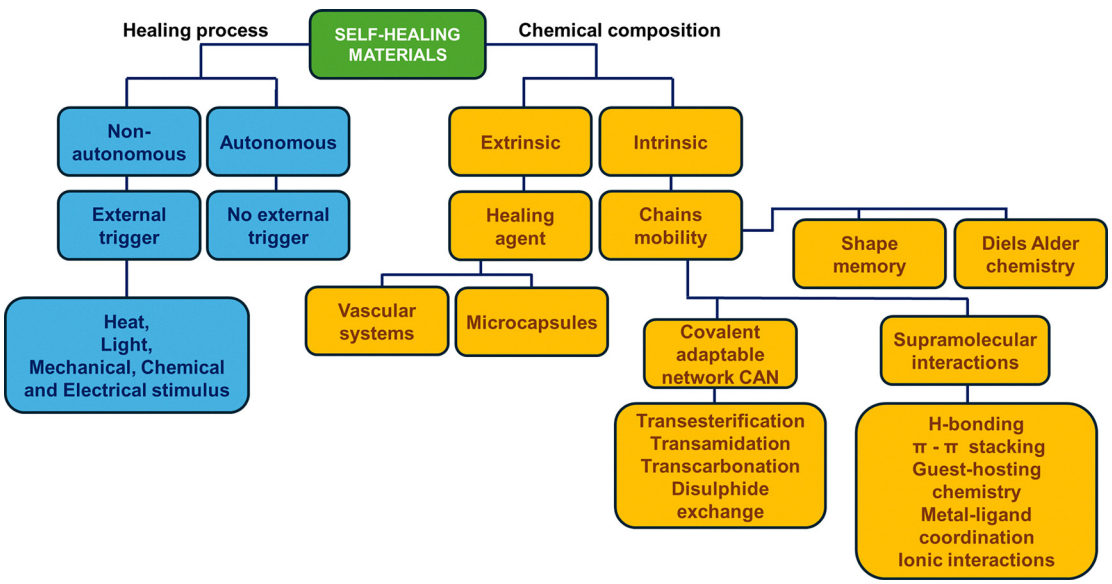

Fig. 7 Classification of self-healing materials.

panels, cells, booms, self-deployable structures, reflector antennas, and more, can regain their standard shape in response to an external environmental change.

Several reviews are present regarding the history, developments, applications, and future scope of SMPCs.[191,192] 3D printing of SMPCs has been coined as 4D printing, meaning the geometrical design of the object could change over time, which is the fourth dimension. Currently, printed SMPCs can be used as the cell core of sandwich structures as a substitute for metallic microlattices, which are slowly produced, or for deployable structures and morphing wings, able to change their shape during flight to adapt to different aerodynamic conditions, thereby optimizing the vehicle's performance and efficiency in aerospace and aeronautics.[92] Also advanced materials can be used for 4D printed SMPs, such as recyclable resins[193] and biobased vitrimers.[194–196] Although SMPs usually exhibit better shape memory effect with a lower price than shape memory alloys, due to larger deformation upon programming, the main limitation to overcome is the lack of complete and efficient constitutive models based on viscoelasticity in complex geometries for 4D printing structures.[197] SMPCs face key challenges in strength, durability, thermal stability, and recovery efficiency, especially under the harsh conditions of space. To address these issues, future research should focus on developing advanced materials and manufacturing techniques.[197] In the case of 3D printed objects, a self-healing function could remedy failures due to mechanical wear (cyclic load). Typically, 3D printed components present discontinuities, which represent internal weak points.[198] For example, in the FFF and SLS processes, discontinuities are due to adhesion problems governed by poor macromolecular interdiffusion at the interface of filaments in FFF objects[198] and of the particles in the SLS parts.[199]

Another example is given by SLA products, where weak points are due to a gradient of curing degree,[200] which could appear between one printed layer and the following. A healing action activated at these points would ensure a more extended durability and a higher reliability of the component.[201] Currently, there are few examples of 3D-printed self-healing materials being applied in aeronautics and aerospace. Most self-healing materials used in 3D printing are essentially elastomers employed for the development of self-healing actuators,[202] due to their ability to snap back after impact.

3. 3D printing technologies in the aerospace and aeronautical sectors

3.1. Fused filament fabrication (FFF)

Fused filament fabrication (FFF) is undoubtedly the most widely used 3D printing technique in the industrial field for processing thermoplastics, their composites, and nanocomposites. FFF is also known as fused deposition modeling (FDM), which was coined by Stratasys. The FFF working principle is the deposition of molten thermoplastic material on a movable printing bed according to the digital instructions suggested to the printer.

Once deposited, the building material solidifies, maintaining the given shape so that no light source or bonding agent is needed to compact it. A common FFF printer features a printing head that can feed material as pellets or as a spooled filament with precise diameter dimensions (Fig. 8a). This means that, on the one hand, it is possible to use commercial materials directly available on the market. Still, on the other hand, if the material has been formulated in the laboratory, it is necessary to produce the filament through an extrusion line.[203] When fed as a spooled filament, the material is directed through a thin nozzle by a motor and associated rollers, allowing it to be directed towards a specific location. In the case of pelletized material, a small screw is positioned in the channel (see Fig. 8b). Electrical resistance heats the nozzle, causing the material to melt. At the same time, the already solid material continues to be carried downwards and pushes the melt material to exit from the die on the mobile platform.[204]

The printing head builds a 3D object layer by layer according to a sliced CAD model moving along the x direction, while the printing bed goes back and forth along the y direction, as shown in Fig. 8a. Once the layer is completed, the printing head moves upward (in the z direction) to allow the deposition of a new layer.[203] FFF technology offers the possibility to allocate two printing heads on the printer, one for the building material and the other for the supporting material. In fact, in the case of an object with voids or prominences, during the printing process, some parts can collapse without any support. The supporting material is often a soluble or weak material that can be easily removed manually at the end of the printing process. The double head enables multi-material FFF, allowing for the achievement of high mechanical properties in specific parts of the item.[205] The FFF process allows for the printing of

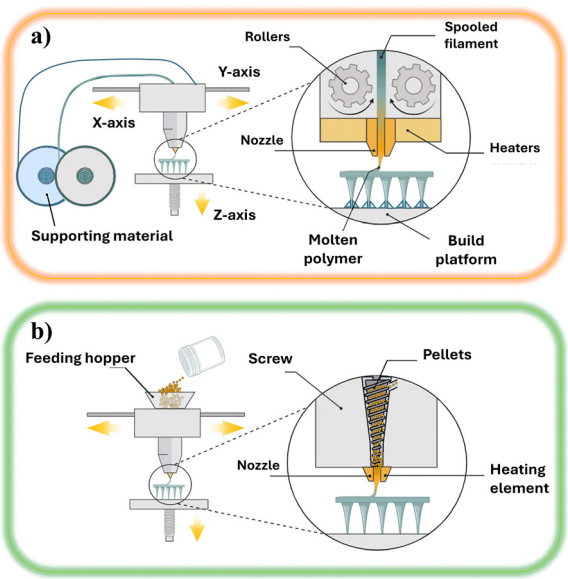

Fig. 8 (a) Schematic representation of FFF printing; (b) printing head of the FFF printer for the spooled filament and for pelletized material.

continuous fibers (*e.g.*, long carbon fibers, metallic wires, aramidic, and glass fibers). Markforged developed a double-barrel printing head, one of which is used for long fibers, while the other is used for building materials. In cases where supports are needed, they are made from the same building material, and to facilitate removal, the printing parameters for the supports (such as infill density and infill pattern) are set in a way that allows them to be easily detached from the main part.

3.1.1. FFF process parameters and material properties. To successfully print an object using FFF technology, several parameters must be set appropriately, some of which strongly depend on the type of building material. Build orientation means the position of the object on the platform. In the CAM phase, the operator can change the orientation of the object by rotating it from 0° to 360° around each of the three axes in space: x, y, and z, thereby changing its position on the printing bed. Layer height refers to the thickness of each layer that is deposited. At the same time, the nozzle diameter determines the thinner cross-section that the molten material must flow through just before it is deposited on the building platform. Layer height and nozzle diameter determine the shape of the deposited filament (*e.g.*, its width), thereby influencing the air voids entrapped in the final product. The porosity of the printed parts can be managed using the infill density (the printed portion of the volume to the total volume of the item), infill pattern (the schematic path of the deposition), air gaps (which assumes 0 value if filaments are just adjacent one to each other, negative values for overlapping them resulting in a denser structure, or positive value when filaments are deposited apart one to each other). Mechanical properties are affected not only by porosity but also by other FFF parameters, such as raster angle, which determines the direction of filament deposition during layer printing, and interlayer adhesion, which is governed by the extrusion temperature (the maximum temperature reached in the nozzle). To increase the interdiffusion phenomenon between deposited filaments, TPE is a potential candidate as an additive due to its good adhesive properties.[205–207] Bed temperature, along with extrusion and chamber temperature, significantly affects the cooling rate of the deposited material. The cooling rate plays a pivotal role in the dimensional stability of semicrystalline polymers (*e.g.*, PEEK, PBT, PP). Since crystals are compact structures absent in amorphous polymers, the reduction in specific volume upon cooling of semicrystalline polymers is more consistent than the specific volume reduction in the amorphous ones.[208] When the crystallization rate is very high, in the temperature interval between T_m and T_g, macromolecular chains pack into crystals very rapidly. To limit shrinkage and warpage in 3D printed objects, it is necessary to have a cooling rate higher than the crystallization rate. To address the problem of dimensional stability and detachment from the building plate, it is possible to act on other parameters such as brim (number of outlines around the specimens and attached to it), contours (number of perimeters already forming the piece), and raft (few layers characterized by infill density lower than 100% before starting to print the sample). To predict the quality of the first layer and the adhesion property between the molten material and the bed, printing a skirt (a certain number of contours around the base of the piece without touching it) could be a good practice. In the event of adhesion or warpage issues, the printing process can be stopped before it starts, allowing for optimization of the process parameters in advance. Finally, printing speed and printing flow rate are two fundamental parameters that are often confused with each other. While the printing speed refers to the velocity of the printing head movements, the printing flow rate represents the quantity of material exiting the nozzle per second. The flow rate must be appropriately synchronized with the printing speed to prevent issues with dimensional stability, optimize process time, and ensure the complete melting of the materials.[209] M. Golab *et al.*[210] reviewed experimental studies conducted over the past 25 years that have aimed to improve the quality of FFF printed parts *via* printing parameter optimization. The effects of these parameters on the final quality of FFF-printed objects are summarized in Table 5.

During the extrusion process, polymeric chains undergo shear stress and relaxation phenomena, necessitating the investigation of rheological properties such as viscosity, yield stress, and elastic modulus to estimate printability. Material requirements for the FFF process are essentially the following: (1) highly thixotropic and shear thinning behavior, (2) appropriate viscosity to guarantee the extrusion and the formation of continuous filaments, (3) a quick rise in viscosity following deposition to keep the shape of the 3D printed object, (4) after exiting the nozzle, the material must have enough mechanical strength to support the structures that are printed later and to avoid delamination both during and after printing.[94] Das *et al.* demonstrated that interlayer weld and chain diffusion depend on the entire printing process (dynamics inside the nozzle, stand-off region, and print bed), especially on bed and chamber temperatures, as well as the period of material staying above T_g compared to the polymer relaxation time.[226] Other works in the literature suggest the use of TPE as an additive to increase the interdiffusion phenomenon between deposited filaments due to its good adhesive properties.[205–207] Phan *et al.*,[227] in a separate study, analyzed pressure drop data using rheological models to quantify heat transfer in the FFF process, highlighting it as a key factor limiting the increase of production speed. As mentioned earlier, heat transfer is crucial during the cooling phase to prevent shrinkage or warpage defects. A strategy that allows for the improvement of dimensional stability and at the same time modifies the thermal properties of the materials (*e.g.*, coefficient of thermal expansion), is the addition of fillers such as nano clay,[228] carbon fiber,[229] glass fibers,[204] graphene,[230] and carbon nanotubes.[231,232] However, the incorporation of fillers could cause some issues during the process. An excess of nanofiller concentration results in a discontinuous extrusion or material inhomogeneity due to the nozzle partially clogging.[230] Although carbon and glass fiber can limit warpage, the interface properties between the thermoplastic matrix and the fiber surface also need to be investigated.[233] To improve rheological properties, polymer

Table 5 FFF process parameters and their effect on the properties of the final printed objects

Process parameters	Effects on	Ref.
Building orientation	• Mechanical properties • Surface accuracy	205 and 211
Layer height	• Contact area between layer interfaces • Process duration • Surface quality	212
Nozzle diameters	• Width of deposited filaments • Layer height (0.5–0.75 times nozzle diameters) • Die swelling phenomenon • Porosity • Processability of nanocomposites (clogging concern)	213
Infill density	• Air voids • Final mechanical • Material consumption • Load-bearing capability of the final object,	214
Air gap	• Overlapping percentage between adjacent filaments • Density and compactness of the final object	215 and 216
Infill pattern	• Process duration • Infill density • Material consumption • Mechanical properties	216 and 217
Raster angle/printing direction	• Mechanical properties • Electrical properties in conductive nanocomposites	166, 167, 218 and 219
Extrusion temperature	• Interlay adhesion • Material viscosity • State of stress in the channel • Die swell phenomenon • Cooling phase	220
Bed temperature	• First layer adhesion of the building platform • Limiting shrinkage defects • Interdiffusion phenomenon between deposited filaments • Cooling phase	205–207 and 221
Chamber temperature	• Cooling phase • Warpage defects	222–224
Contours	• Dimensional stability • Minimizing distortions and strengthening the parts	Based on the author's experience
Brim	• First layer adhesion in case of poor adhesion • Limiting warpage phenomenon	Based on the author's experience
Raft	• Piece removal in case of high first-layer adhesion on the building platform	Based on the author's experience
Skirt	• Understanding of printability before printing the piece	Based on the author's experience
Printing speed	• Process duration • Air voids • Mechanical performances	225
Printing flow rate	• Dimensional stability • Extrusion speed • Melting capacity	209

blending is another alternative approach. For example, Chen *et al.*[69] added poly(methyl methacrylate) (PMMA) and methacrylate–butadiene–styrene (MBS) to ABS, demonstrating that the higher Mass flow rate (MFR) of the ABS/PMMA blend led to better 3D printability of ABS.

Integrating dynamic covalent chemistry into thermoset polymers offers a promising strategy to enhance their processability using FFF. This approach addresses the long-standing challenge of reprocessing and reshaping thermosets by enabling reversible crosslinking. Such dynamic bonding improves the adaptability and 3D printability of these materials.[94] In one example, Voit and colleagues[234] designed polymers that undergo crosslinking through Diels–Alder reactions between furan and maleimide groups. They investigated both the printability and structural quality of the printed objects. Thanks to the temperature-dependent, reversible nature of the crosslinks, the material's viscosity could be controlled by adjusting the temperature. During printing, the polymer was extruded at elevated temperatures, achieving a low viscosity of around 0.8 Pa s. To solidify the material post-extrusion, a steady stream of cool air was applied to increase viscosity and stabilize the printed form.

Most of the thermoplastic materials introduced in Section 2.1 are used in the FFF process. In light of the process parameters discussed earlier, Fig. 9 provides a schematic summary of the mechanical properties and printability of thermoplastic materials in FFF printing.

Table 6 reports the list of polymeric composites and nanocomposites already available on the market for the FFF process, while the findings of the recent research activity on them have been summarized in Table 7. Billah *et al.*[236] designed large-scale 3D printed electro-thermal heated moulds for out-of-oven autoclave application through co-extrusion of the polymer matrix and a long carbon fiber. H. Pei *et al.*[237] developed a

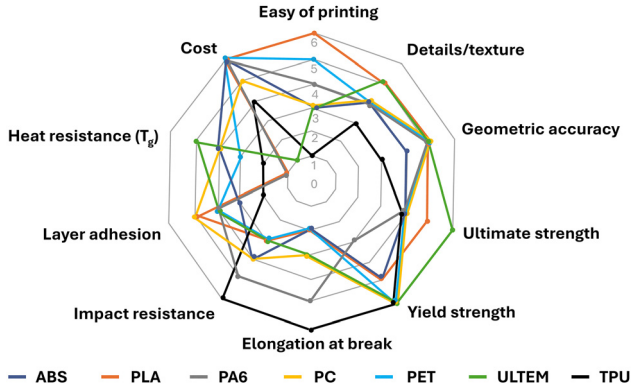

Fig. 9 Printability and mechanical properties of the most used thermoplastic materials in the FFF process. Reproduced with permission from ref. 235. Copyright 2021 Springer Nature.

highly piezoelectric nanocomposite energy harvester using poly(vinylidene fluoride) (PVDF) enhanced with tetraphenylphosphonium chloride (TPPC) nanoparticles. Experimental results showed that adding TPPC significantly increased the polar β-phase content, reaching around 83.8%. By utilizing an FFF printer, the researchers were able to create complex porous structures within the harvester, improving both its flexibility and piezoelectric performance. Notably, with just 5 wt% TPPC added, the 3D-printed device achieved an open-circuit voltage of up to 6.62 V—about five times greater than that of pure PVDF. In another study, a multi-nozzle FFF printer was employed to fabricate a strain sensor for aerospace applications by combining neat PEI (as the substrate) and CNT/PEI composites (as conductive traces) in two strain gauge patterns in a single step. The authors demonstrated that sensors with 3 wt% CNTs had good conductivity and exhibited reliable piezoresistive behavior during cyclic tensile tests.[238] Shinde *et al.*[239] obtained an 81% healing efficiency (estimated on mechanical properties) by coating the HIPS filament with Double-walled microcapsules, environmentally filled self-healing with friendly ethyl phenylacetate solvent (healing agent). A system trying to include three functionalities (electro-thermal heating, piezoresistive properties, and shape memory) was developed by W. Ye *et al.*[240] Coaxial carbon fiber PLA/TPU filament was printed *via* FDM in the form of a honeycomb structure. The variation of electrical resistance was monitored during the compression test. At the same time, during the compression test, the sample was cooled down to freeze the compressed shape. Once the load was removed, by applying a voltage to the carbon fiber reinforced material, the temperature increased due to the Joule heating effect, and the strain energy stored in the matrix material was released, recovering the initial shape of the sample. Luan *et al.*[241] designed a 3D printing self-healing and self-sensing device. In more detail, a hollow structure of PLA was printed *via* FDM, and during the printing process, thanks to a double printing head, a continuous carbon fiber was deposited as structural reinforcement and a sensing element. Structural states such as strain and damage can be identified by measuring the electrical resistance of the continuous carbon fiber tow. The self-healing functionality was brought to the system by incorporating the curing agent into hollow structures within the thermoplastic matrix. An approaching crack ruptures the internal channels, which release the curing agent that flows into the crack plane through a capillary action or an external pressure. Subsequently, the polymerization of the curing agent bonds the crack faces. The main disadvantage of this system is due to the fact that self-sensing ability could be compromised after the first self-healing cycle. In addition to these peculiar cases of smart composites and nanocomposite thermoplastic materials processed *via* the FFF, other examples of smart materials and their functionalities for the aerospace and aeronautical sectors are reported in Table 7.

Table 6 Commercially available thermoplastic composite filaments and thermoplastic composites with information on the manufacturing companies and product names

Commercially available thermoplastic composite filaments	
Company	Product
3DXTech	3DXNano TM ESD ABS + carbon nanotubes filaments
	3DXNano TM ESD PETG + carbon nanotubes filaments
	Carbon XTM carbon fiber Ultem 3D printing filament
	Carbon fiber based filament (matrix: Ultem, PC, Nylon, PLA, PETG, ABS)
Functionalize F-electric	Functionalize F-electric filament (PLA & carbon nanotube)
Filabot	MWCNT1 multi-walled carbon nanotube pellets
	Graphite infused filament–ABS matrix-based filament
Black magic 3D	Conductive graphene filament (matrix used: HIPS, nylon, PLA)
	Ferro-magnetic PLA
	G6-impact HIPS-carbon fiber-graphene filament
Octofiber	UPM Formi-PLA, cellulose polylactic acid
	Octofiber carbon filament, PETG and high-modulus carbon fiber
	Octofiber bronze metal filled PLA
	Octofiber copper metal filled PLA
Owens-corning	XSTRAND GF30-PA6, Glass fiber polyamide (grade PA6)
	XSTRAND GF30-PP, Glass fiber polypropylene
	XSTRAND GF30-PC, Glass fiber polycarbonate
Innofil3D	PET carbon fiber
	AzureFilm PET CF, PET filled with carbon fibers
Carbodeon	Udiam-PLA, nanodiamonds polylactic acid
	Cicla 3D nano-infused copper antibacterial PLA filament

Although smart materials are widely used, their application in 3D printing for aerospace and aeronautical applications remains limited. This is mainly due to the difficulties in scalability, integration environment requirements, and trade-off between the efficiency of smart properties and structural/mechanical characteristics. This aspect will be clear in the following sections, where only a few examples of real parts with smart properties are reported.[242]

In the last few years, the research field of aerospace has focused attention on how process parameters and materials properties could change in a microgravity environment in the case of "IN space" printing. The first 3D printer was sent to the

Table 7 Effect of filler in FFF-printed polymer composites

Composition	Properties	Ref.
ABS-copper particles ABS-iron particles PE-copper particles PLA-bronze particle PLA-copper particles	Improved tensile properties, electrical and thermal conductivity; decrease in the thermal expansion coefficient and increase in thermal resistance	248–253
ABS-$BaSrTiO_3$	For a ceramic polymer composite with 50 wt% (15 vol%) solid loading, a relative permittivity ε_r = 6.05, $Q \times f$ = 10 433 GHz and dielectric loss tan δ = 0.007 were obtained (reduced dielectric losses compared to standard laminates currently used in the radiofrequency (RF) and telecommunications industry). Hemispherical dielectric lens based on ABS-$BaSrTiO_3$ composite increased the antenna gain by 3.86 dBi.	254
PETG-TiO_2 particles	Relative permittivity increased by 50% for a composite filled with 20 wt% of ceramic particles (ε_r = 2.5 ÷ 4.4) against pure PETG; TiO_2 filling transformed the PET-G from ductile to brittle material; improved damping behavior	255 and 256
PC-nano silica	Improved mechanical properties: elastic modulus of 0.63 GPa (16% increased), tensile strength of 62.02 MPa, elongation at break of 21.89% and specific optical properties (higher transmittance of UV light) at low concentration; formation of voids	257
ABS-short carbon fibers PA-short carbon fibers PLA-chopped fibers PC-short carbon fibers PEI-chopped fibers PAEK (polyaryletherketone)-short carbon fibers	Increase in the tensile strength, flexural modulus, and interlayer adhesion strength in flexure tests; building orientation influence on voids distribution, material hardness, and stiffness; weak interfacial adhesion between the fibers and the matrix; fiber pullout; improved thermal stability; improved inter-layer strength.	258–266
PA6-recycled carbon fibers PLA-recycled carbon fibers PEEK-recycled carbon fiber PPS-recycled carbon fiber	Low porosity and excellent fiber orientation; enhancement of flexural strength and surface roughness; improved electrical and thermal conductivity; significantly improved crashworthiness, good chemical resistance	267 and 268
PA6-continuous carbon fiber PLA-continuous carbon fiber PEEK-continuous carbon fiber PA-6/PLA-continuous carbon fiber	High tensile strength up to 358 MPa; improved mechanical properties and surface quality of final parts; ultrahigh flexural modulus and strength (125.7 GPa and 1901.1 MPa, respectively), high tensile modulus and strength (133.1 GPa and 1513.8 MPa, respectively); scalable fabrication of composite aerofoil with high fiber content (>50%)	269–272
ABS-short glass fibers PLA-continuous glass fibers PEEK-glass fibers	Increase in the tensile and flexural strength, reduced warpage defect; increased surface roughness; enhanced impact strength; necessity of improving interfacial bonding between fiber and polymer adding compatibilizer; enhanced thermal stability.	273–275
PA-short carbon fiber/glass fiber layers	Improved mechanical, thermal, and flame-retardant properties	257
PLA-natural fibers	Tensile Strength improvement, increase in the storage modulus and elastic modulus; clogging, inhomogeneous distribution	276–278
PC-cellulose nanofiber ABS-cellulose nanocrystal PLA-cellulose nanofibers	Improvement of mechanical performance at low filler concentration; increase in water absorption and surface roughness; higher crystallinity and reduced composite defects.	279–281
PEEK-tungsten particles PLA-tungsten carbide PP-tungsten carbide	Improvement of dielectric permittivity and X-ray and gamma-ray radiation shielding; improvement of tensile and flexural strength and microhardness, indicating a possible high resistance to wear.	282–284
PLA-montmorillonite HDPE-montmorillonite	Improved thermal stability; improved tensile and flexural modulus and strength.	228 and 285
PLA-polyhedral oligomeric siloxane (POSS)	Improved flexural strength (by 22%), flexural modulus (by 9%), and toughness (by 17%) compared to pure PLA.	286
SEBS/PP blend-carbon black	Filler segregation in the SEBS phase. 40 PP/60 SEBS (w/w) blend composition behaved as a TPE. At loadings of carbon black (7.5 phr), tensile strength and Young's modulus increased by ~28% and ~33%, respectively, compared to the unfilled blend, while the elongation at break reduced by ~4.5%.	287
TPE-carbon black TPE-graphene	The surface-modified CB/TPE composite showed about four times more wear resistance and 26% improvement in tensile strength as compared to bare TPEE resin. The graphene/TPEE composite with only 1 wt% graphene exhibited an elevenfold increase in wear resistance and 43% improvement in the tensile strength owing to the high dispersibility and lubricating effect of the two-dimensional graphene filler.	288

International Space Station (ISS) by NASA and Made In Space. ABS was produced in many pieces, which were then returned to Earth for analysis and examination. The study revealed that microgravity did not lead to significant effects on the polymer parts. The expedition demonstrated the application of 3D printing, namely the FFF process, in a microgravity

environment.[243] Since then, a new scenario has emerged, involving an initiative to recycle materials on board using foam and films used to package cargo as a potential feedstock for manufacturing.[244] The few experimental examples of FFF printed objects IN space were reported in a NASA article.[245] The confined environment of a space station hinders the use of highly volatile species; for this reason, the FFF process is one of the most studied ones. The suitability of the FFF process for microgravity conditions stems from the favorable surface tension and viscosity of the molten thermoplastic, which allow the material to be extruded and adhere effectively to the initial surface without the need for gravity. 3DP, POP3D, MELT, AMF, REFABRICATOR, and IMPERIAL are the successful candidates of a project led by the USA, Italy, Europe, and China studying FFF manufacturing on ISS flight.[246]

The polymers utilized range from common types like PLA and ABS to advanced, high-performance thermoplastics such as PEEK and PEI-based Ultem®. Based on the materials processed to date, 3D printers designed for microgravity environments can achieve extrusion temperatures that are suitable for printing materials like Ultem® and PEEK, typically around 380 °C. Developing suitable AM technologies for space remains a significant challenge due to the difficulty in replicating space conditions—such as microgravity, vacuum, and extreme temperatures—on Earth. Various platforms, including laboratory setups, parabolic flights, sounding rockets, and re-entry missions, have been used to simulate these environments. While these platforms provide valuable insights and contribute to technological progress, they also face limitations, particularly in terms of experiment duration and iteration speed under microgravity. The influence of space-related physical parameters varies: for example, the absence of gravity has a minimal impact on material properties but significantly affects manufacturing processes and technologies.[247] Conversely, vacuum conditions have a strong influence on materials but less on the process itself. A deeper, parameter-specific understanding is essential for designing practical experiments and selecting the most suitable simulation platforms to advance AM development for space applications.

3.1.2. FFF printed parts in the aeronautical and aerospace sectors. The Air Force Institute of Technology (AFIT) in Ohio stated that the use of the FFF-based industrial 3D printer from Stratasys not only has the capability to print aircraft parts but also the material is certified for use on both Federal Aviation Administration (FAA) and the U. S. Department of Defense (DOD) governed aircraft.[289] In a 2016 technical report, AFIT demonstrated that FFF technology allows for the printing of a replica of the honeycomb structure using ULTEM 9085, reducing maintenance costs and time. There would be no more than a 24-hour downtime (considering 10 minutes for the piece design and 10 hours to manufacture it) as a result of the repair process. The technicians would be freed up to work on other tasks while the 3D printer created the unique honeycomb part, as 3D printing does not require labor to construct the item. This case study[290–294] is reported in Fig. 10a. However, FFF can be used not only for maintenance purposes but also for developing advanced micropropulsion systems. AM offers the opportunity to package propulsion systems in innovative ways that can minimize mass and optimize the utilization of space within small satellite and nanosatellite (CubeSats) class systems. California Polytechnic State University at San Luis Obispo (Cal Poly) and Stanford University developed a class of nanosatellites characterized by a standard size and form factor (Fig. 11) in 1999; for this reason, they are known as CubeSats. "One unit" or "1U" of a standard CubeSat measures 10 × 10 × 10 cm; however, the dimensions of this call of satellites can be extended to larger sizes, including 1.5, 2, 3, 6, and even 12U. According to NASA declarations, CubeSats have emerged as an affordable solution for conducting scientific research, testing innovative technologies, and exploring complex mission strategies involving constellations, swarms, and distributed architectures.[290] An image of the actual CubeSat is reported in Fig. 10g. Creating the first completely 3D printed small satellite was the goal of a consortium of innovative experts in AM comprising Northrup Grumman Technical Services, University of Texas at El Paso (UTEP), Configurable Space Microsystems Innovations & Applications Center (COSMIAC), NASA Glenn Research Center (GRC), and Youngstown State University. In more detail, this group of researchers utilized an advanced FFF technique to produce complex geometries. A method was developed to interrupt the printing process and insert components into specific cavities. To maximize the available internal space for functional purposes, these components could be directly inserted into the wall of the small satellite, resulting in an even smaller, more efficient carrier vehicle. This allows for increased experiment and instrument capability by providing added volume in a confined, small satellite space.[292,293] Once the cavities are completely formed, the printing process stops, and protective caps are placed around the sensors and inserted in the cavities. After a visual inspection, the printing process is resumed to complete the device (Fig. 10b). Similarly, a FFF printed skeleton was designed by UTEP to integrate solar panel coverglass with interconnected cells in a 3U CubeSat prototype, providing the desired voltage and current range for charging an onboard battery (Fig. 10c).[292] Moreover, the same research group attempted to develop a communication system that prints the antennas into the walls of the spacecraft for both downlink to the ground and space-to-space communications. The antenna was fabricated by printing a polycarbonate plate after a two-arm Archimedean spiral was introduced by embedding wire into the plastic (Fig. 10d). In this scenario, parameters such as the inner and outer circumferences (which determine the frequency band), the number of spiral turns (or flare rate), and the feed structure can all be readily adjusted using the previously described printing method.[292] In the context of "Printing the Complete CubeSat" within the NASA STMD Small Satellite program, a micro-pulsed plasma thruster (μPPT) was chosen to be embedded into a materials extrusion-built part *via* FFF. To insert a μPPT into a polycarbonate sample body, the sample panel was first printed, then the μPPT was embedded, wires were placed, and finally, the sample was sealed with further printing over the μPPT. The

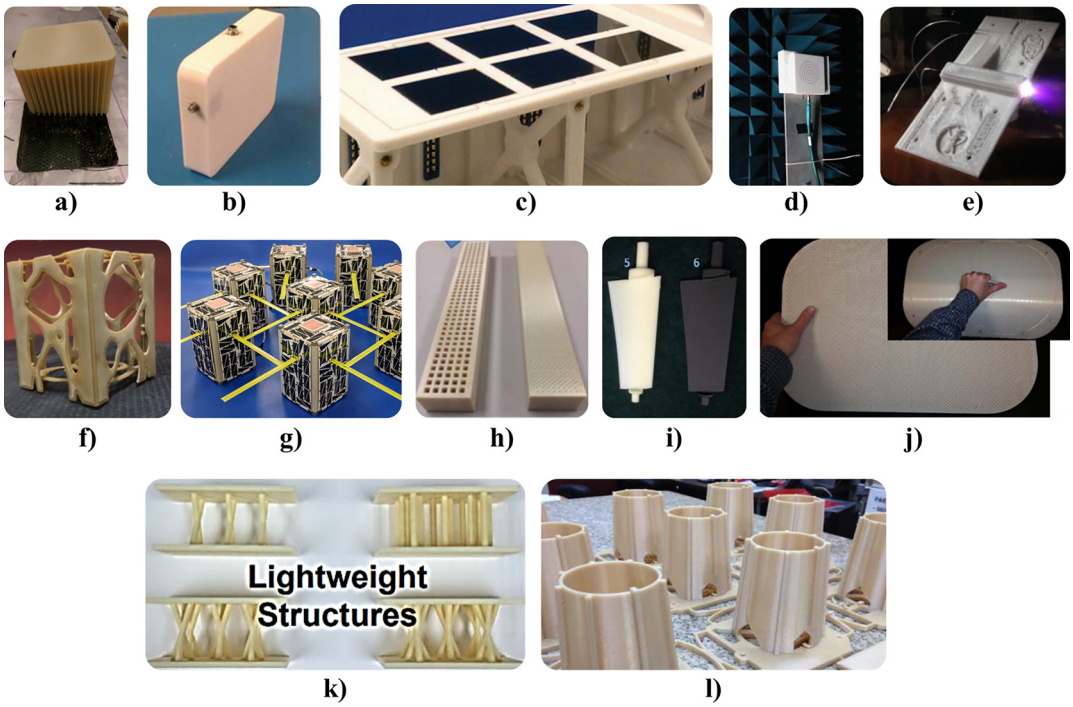

Fig. 10 Examples of FFF printed parts for aerospace applications: (a) 3D printed ULTEM 9085Honeycomb for maintenance purposes;[289] (b) embedded sensors with exterior connector access in a completely 3D-printed device;[292] (c) completed 3U CubeSat prototype with an embedded copper wire connecting a solar panel, interconnected cell array, to the power bus;[292] (d) embedded two-arm Archimedean spiral in polycarbonate printed parts for communication purposes;[292] (e) photograph of the printed μPPT thruster panel firing under vacuum conditions;[296] (f) 3D printed PEEK optimized nanosat. Reproduced with permission from ref. 294. Copyright 2020 MDPI; (g) image of the real CubeSat used by NASA;[290] (h) acoustic liner rest articles;[11] (i) inlet guide vanes made of ABS and Ultem 1000 with and without chopped carbon fiber reinforcement;[11] (j) engine panel access door;[11] (k) lightweight structures;[11] (l) COSMIC-2 anatenna.[291]

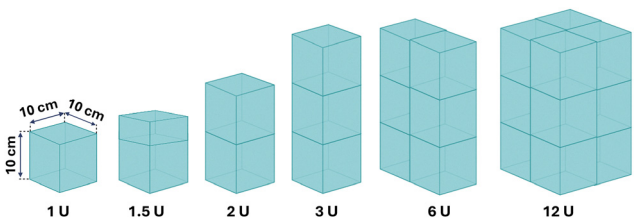

Fig. 11 Standard sizes and form factor of nano- and microsatellites named CubeSats.[290]

final item is shown in Fig. 10e. It was demonstrated that a μPPT can survive the printing/embedding process and can operate without significant degradation to the surrounding material.[293] Rinaldi *et al.*[294] studied a topology optimization method (TOm) to reduce the weight of CubeSats. Due to the complexity of material distribution generated by TOm and the constraints of conventional fabrication processes, FFF was used to overcome these issues. The FFF-printed optimized nanosat is reported in Fig. 10f. The authors analyzed all phases of the production process, including thermomechanical design, raw material selection, printing process tuning, and manufacturing. When working with composite inlet guide vanes, researchers observed that incorporating 10% chopped fibers into Ultem 1000 significantly raised the material's viscosity. This adversely affected the compounding performance of the extruder, resulting in high porosity in both the extruded filaments and the final FDM-printed composite parts. As a result, they recommended exploring thermoset polyimides, which offer higher thermal performance and lower viscosity, through selective laser sintering (SLS) for future studies on composite 3D printing materials.[295] NASA Jet Propulsion Laboratory (JPL) has developed COSMIC-2, a satellite technology to capture a revolutionary amount of radio occultation data from GPS and GLONASS. One of the critical components of the COSMIC-2 design was the antenna arrays. It was a medium-sized project that required 30 antennas.

JPL sought an alternative to conventional processes and materials (astroquartz) to complete the project on schedule and within budget. Thus, minimizing manufacturing costs and assembly time was essential. NASA JPL, in collaboration with Stratasys, succeeded in printing COSMIC-2 antenna (shown in Fig. 10(l)) arrays *via* the FFF process of ULTEM 9085 resin. The truncated conical surface was designed with an inclination angle lower than 45° to allow the self-supporting of the structures, saving machine run time and reducing the risk of breaking during manual support removal.[291] Moreover, NASA designed the Desert RATS (a Rover) having about 70 of its parts manufactured *via* AM, and in particular, the front bumpers, flame-radiant housings and vents, complex electronics, camera

mounts, and large pod doors are made of PC and ABS, produced *via* the FFF technique.[17]

Regarding the aeronautical sector, various attempts to utilize FFF technology for producing lightweight components suitable for non-structural applications are documented in the literature. S. KobenKo *et al.*[78] studied the feasibility of replacing current metallic aircraft interior parts with a high-strength-to-weight-ratio, flame-retardant, and high-performance thermoplastic Ultem 9085. The authors produced two real-world examples, considering the actual dimensions: a class divider and a seat-folding table. The class divider is an aircraft interior part connected to the ceiling and used to separate the different ticket class sections. It has a complex geometry and is typically composed of two metal parts that are initially machined using a subtractive numerical control process and then joined. Fig. 12a reports the class divider in metals and the sample produced by the authors *via* FFF technology. This part has been demonstrated to be able to sustain the maximum stress without clearly breaking, according to the findings of mechanical testing that involved a vertical downward pull and a horizontal forward push. Additionally, the test revealed that the part had no residual deformations. As a non-engineering structural component, the seat folding table could support a force of 900 N at most when loaded at the tip. In this way, the authors have demonstrated that FFF technology could substitute conventional processes, reducing the number of components needed for the fabrication of the interior part. Large-format additive manufacturing has attracted the attention of big companies in the aeronautical sector.[297] An example is the collaboration between Airbus and Materialize to install 3D-printed panels on board Finnair's A320 aircraft, produced with flame-retardant Airbus-approved materials and featuring a bionic-optimized design, which reduces the original weight of this part by 15%.[298] Additive Flight Solutions, a joint venture between Stratasys and SIA Engineering Company (SIAEC), recently received AS9100D quality management certification for the supply of 3D printed parts to the aerospace market, with most parts produced *via* the FFF process. Currently, FFF and SLS 3D printing processes are the most commonly used for the interior parts of airplanes, as reported in the technical report of the Air Force Institute of Technology of the United States.[289]

V. Acanfora *et al.*[299] proposed a new approach to achieving very high weight reduction in sandwich panels using the FFF process. The core structure of sandwich panels, made of polypropylene (PP), was designed to maximize their performance in terms of energy-to-weight ratio and impact load damping by varying the infill density, while the external face sheets are composed of carbon fiber reinforced polymers (CFRPs). A photo of the sample is shown in Fig. 12b. Three different configurations of the inner part were studied: a reference configuration with 100% infill density, a solution of alternating layers filled at 30% with layers filled at 100%, and a third configuration obtained by alternating a 100% full layer with two 30% infilled layers. At the same time, the raster angle was set equal to $\pm 45^{\circ}$ for each layer in all configurations. The authors found that on the one hand, the mass reduction due to the different infill density increases the ability to dissipate impact energy through flexural deformation, but on the other hand, the infill parameter mainly affects the stiffness of the sandwich panel, which is the maximum for the 100% full-layer configuration and gradually decreases as the lightening process increases. The key point of their work remains the possibility of combining a 3D-printed thermoplastic honeycomb with CFRP to reduce the weight of the structure and increase the absorbed energy during impact tests. Another field in the aeronautical sector suitable for FFF printing technology is that of unmanned aerial vehicles (UAVs), where a human operator is not required. They find application in the military, private, and public sectors. E. Balasubramanian *et al.*[300] conducted a stress analysis of the significant weight contributors among the structural components of a UAV quadcopter to redesign it with a lightweight structure, aiming to improve performance in terms of a shorter take-off range and longer flight endurance without compromising operational safety. Quadcopter configurations, consisting of a suspended fuselage under a set of four fixed-pitch propellers, each of which is powered by a brushless motor, are shown in Fig. 12c. The authors successfully reduced the number of

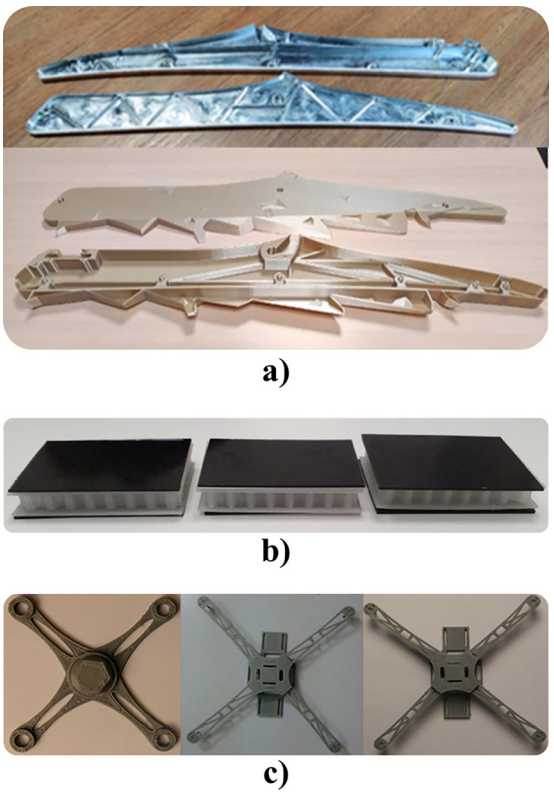

Fig. 12 Examples of FFF printed parts for aeronautical applications: (a) inside view of two halves of a class divider in metals and 3D printed Ultem 9085. Reproduced with permission from ref. 78 Copyright 2022 MDPI; (b) sandwiched shock-absorber configurations made of inner PP 3D printed honeycomb and CFRP skin. Reproduced with permission from ref. 299. Copyright 2023 Elsevier; (c) design iterations of a PLA quadcopter frame printed *via* FFF. Reproduced with permission from ref. 300. Copyright 2019 Inderscience Enterprises Ltd.

parts and weight by approximately 22% and 18%, respectively, compared to the original design of a surveillance quadcopter. Moreover, the electrochemical deposition of a copper–nickel layer on FFF-printed PLA substrates allowed for a more than 10% increase in tensile, flexural, and impact performance. S. Ramirez *et al.*[301] stated that manufacturing UAVs using FFF technology also provides an aerodynamic advantage. More specifically, the anisotropic roughness characteristic of the FFF printed part plays a key role in reducing the drag coefficient. The most favorable case is when the deposited filaments are parallel to the flow line; thus, the model orientation during printing is crucial. The authors also found that the size of the riblets generated with a layer thickness of 0.254 mm maximized the efficiency. In this way, an aerodynamic efficiency improvement of 10% was achieved compared to profiles with a smooth surface. S. Brischetto *et al.*[302] designed an innovative multirotor UAV able to easily and quickly change its configuration from 3 to 8 arms with variable legs. Due to the complexity of this UAV, the authors utilized FFF technology to produce an inexpensive kit of PLA and ABS-printed parts for building the modular drone. Although the authors achieved this goal, they proposed a further improvement by using a high-performance composite material based on carbon filler, integrating electronics directly into the structure using conductive filaments embedded in the arms. Moreover, the Singapore Centre for 3D Printing employed FFF to produce reinforced high-strength-to-weight UAV wings with carbon, glass, and Kevlar fibers into the PA.[303]

Although FFF is already applied to manufacturing and maintaining aerospace components using materials like ABS and ULTEM, its extension to composites and nanocomposite materials for the production of vehicle components remains confined to the research stage, especially for smart materials. Industrial application of these advanced materials will require substantial progress in scaling up laboratory findings, seen in paragraph 2.1.1, to meet the performance and reliability standards of aerospace production.

3.2. Direct ink writing

Direct ink writing (DIW), also known as liquid deposition modeling (LDM), shares commonalities with FFF technology since in both cases, the material is extruded through a nozzle;[304] however, unlike FFF, it is not a molten thermoplastic polymer but a viscous liquid. In the field of polymeric materials, the extruded liquid can be a polymeric solution or a thermosetting resin. However, this technology also allows for printing metals[305–308] and ceramics,[309–313] as well as their derived nanocomposites.[307] Since a wide range of materials can be printed *via* DIW, different curing procedures exist, diversifying the typologies of DIW machines already available on the market. More specifically, DIW technologies are categorized into three classes: extrusion-based (in a strict sense), continuous droplet-based, and energy-assisted DIW.[314] In continuous droplet-based DIW, also referred to as aerosol DIW,[315] there is a stream of ink droplets or segregated droplet deposition, whereas ink is extruded continuously *via* the nozzle in extrusion-based DIW and energy-assisted DIW.[314] The other difference between these classes of DIW is how the solidification of the deposited ink occurs. In the energy-assisted DIW, an external energy source is provided to the deposition site, while in the extrusion-based DIW and continuous droplet-based DIW, no external energy source is required. The three main categories and the different DIW technologies belonging to them are summarized in Fig. 13. Continuous inkjet direct writing (CIJ-DIW), drop-on-demand direct writing (DOD-DIW), and aerosol jet direct writing (AS-DIW) are all continuous droplet-based direct writing methods. Continuous inkjet (CIJ) printing operates by directing a pressurized stream of liquid through a nozzle, where a piezoelectric element vibrating at high frequencies breaks the stream into uniformly sized and spaced droplets,[316] as illustrated in Fig. 13. By precisely controlling the voltage and frequency applied to the piezoelectric component, a stable droplet stream is achieved. When a conductive substance is present in the ink, specific droplets can be electrically charged. These charged droplets are then deflected by high-voltage plates to create desired patterns on a substrate. Meanwhile, droplets that remain uncharged are collected by a recycling system for reuse.[191] The droplets' size is about twice the orifice diameter; typically, for an orifice of $\sim$50–80 μm, the drop size is $\sim$100–160 μm. However, some systems may produce droplets in the range from 20 μm to 1 mm ($\sim$0.5 μL). Commercial CIJ systems have a frequency of 80–100 kHz; however, industrial setups can exceed 250 kHz, with drops traveling up to 20 m s^{-1}.[317] In the DOD-DIW process, the printheads generally feature numerous nozzles, ranging from around 100 up to 1000, although some specialized versions may include only one. Unlike CIJ systems, where drops are formed by external fluid pressure, DOD printing generates droplet motion using internal energy sources positioned near each nozzle. In this process, the fluid exits the nozzle as a jet, which then breaks apart due to surface tension, forming one or more droplets.[191] DOD printers can be categorized into four main types based on how the pressure pulse is produced: thermal, piezoelectric, electrostatic, and acoustic. Among these, the majority of commercially available DOD printers operate using either thermal or piezoelectric mechanisms.[191] In this case, droplet diameter typically matches the nozzle size, often ranging from 10 to 50 μm. The DOD frequency is usually of several kHz (1–20 kHz), depending on the ink properties.[318] In the AS-DIW method, an active ink in the reservoir is spread by an atomizer and transported from the reservoir to the deposition head by nitrogen as the carrier gas. This technology is widely studied for the fabrication of interconnects, sensors, and thin-film transistors. Laser-assisted direct writing (Laser-DIW) and Ultraviolet-assisted direct writing (UV-DIW) constitute the group of energy-assisted DIW technologies. In both cases, the energy source power is the primary process parameter to ensure a compact and mechanically performing object; otherwise, a post-curing heating step may be necessary. The working principle of Laser-DIW involves extruding and depositing the material onto a substrate, followed by rapid heating with a laser source to ensure solidification. To be sensitive to the laser source, the material generally comprises two main

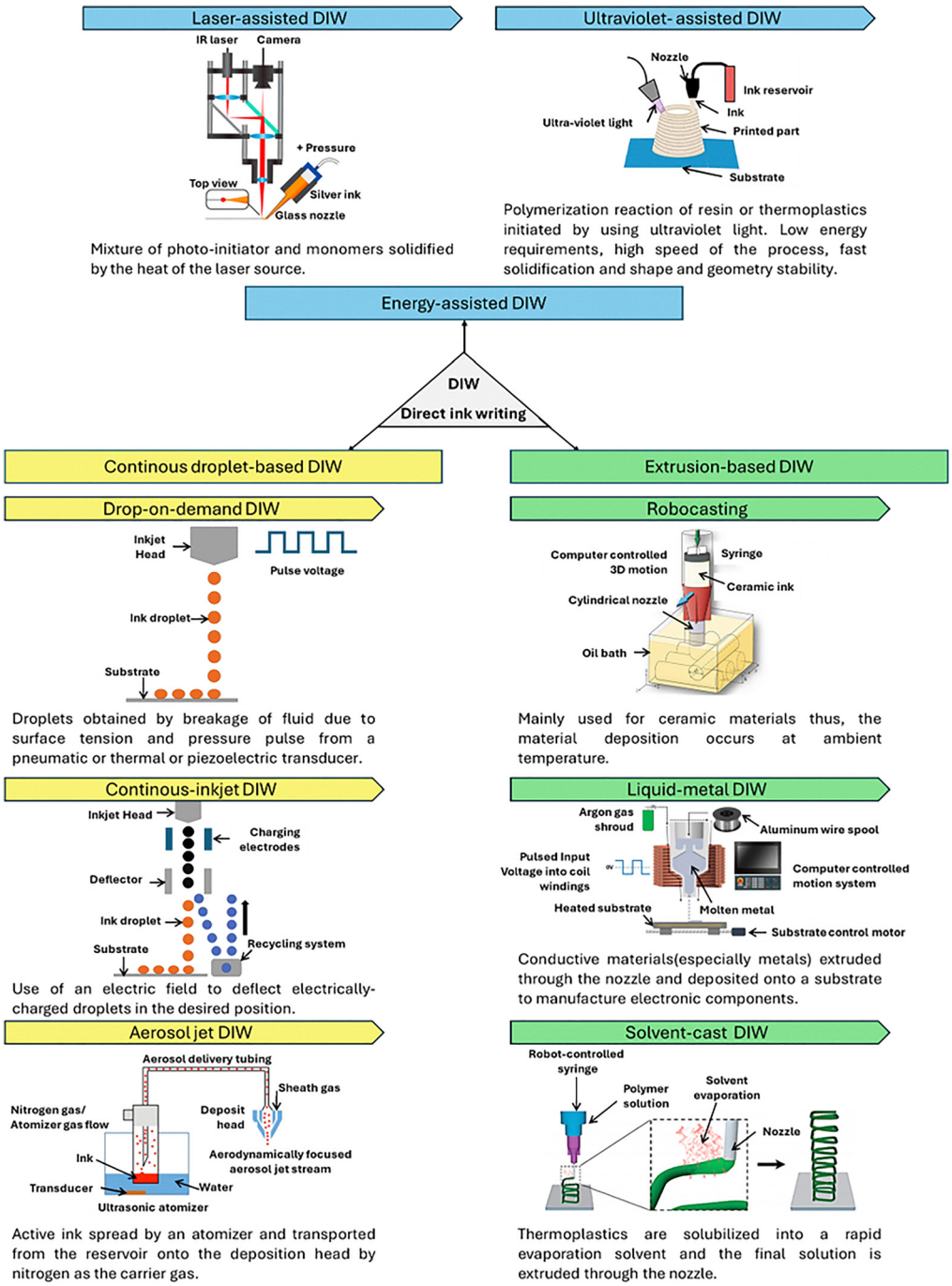

Fig. 13 Classification of DIW technologies and their peculiarities. Laser assisted DIW, ultraviolet-assisted DIW, and solvent-cast DIW reproduced with permission from ref. 314. Copyright 2021 Elsevier. Drop-on-demand DIW, Continuous inkjet DIW reproduced with permission from ref. 322. Copyright 2022 PCM. Aerosol jet reproduced with permission from ref. 323. Copyright 2017 IOP Publishing. Robocasting reproduced with permission from ref. 324. Copyright 2018 Elsevier. Liquid metal DIW reproduced with permission from ref. 325. Copyright 2021 MDPI.

components: a photoinitiator, which activates the polymerization, and a mixture of reactive monomers. However, L-DIW is mainly applied for metals (*e.g.* conductive interconnects, 3D metals architectures (springs, coils), small antennas/spirals). In the UV-DIW process, the working principle is the same as in Laser-DIW; however, the polymerization reaction of resin or thermoplastics is initiated by using ultraviolet light. Due to its low energy requirements, high speed of the process, fast solidification, and stability in shape and geometry, UV-DIW is widely used to produce coatings, electronics, robotics, and optics, among other applications. Robocasting, Liquid metal direct writing (LM-DIW), and solvent-cast direct writing (SC-DIW) are extrusion-based DIW processes. Robocasting is very similar to the FFF process, as the material flows through a nozzle and is deposited on a plate. However, it is mainly used for ceramic materials; thus, material deposition occurs at

Table 8 A comparison of different DIW technologies in terms of resolution, applications, advantages and disadvantages and practical applications

DIW Technology	Resolution	Main applications	Advantages/disadvantages	Ref.
Laser-assisted DIW	Up to micron/sub-micron	Microstructures, functional coatings, electronics, and biomedical devices (*e.g.*, microelectrodes for biosensors, printed RF microantennas). Prevalently used with metals.	High precision/high cost and complex setup	326,327
UV-assisted DIW (UVA-DIW)	~100 μm	Complex structures, polymeric materials, soft robotics, and flexible electronics (*e.g.*, soft robotic arms, microvalves printed in UV resin)	Good structural control/limited to photo-reactive materials	328
DoD-DIW (drop-on-demand)	~20–50 μm	Printed electronics, sensors, and microfluidics (*e.g.*, RFID circuits, piezoelectric sensors printed on PET)	High precision and low waste/low printing speed	329
Continuous Inkjet DIW	~50–100 μm	Ceramics, artifacts, and coatings (*e.g.*, functional coatings on solar panels, ceramic decorations)	Suitable for large areas/lower deposition control	314
Aerosol Jet DIW	~10 μm	Flexible electronics, printed circuits, and sensors (*e.g.*, circuits on curved surfaces, tactile sensors on smart gloves)	High resolution, versatile/expensive, and complex handling	330
Robocasting	~100–500 μm	Dense ceramics, metal composites, and porous structures (*e.g.*, ceramic heat exchangers, bone scaffolds printed in bioceramics)	Suitable for ceramic materials/requires sintering, and limited resolution	331
Liquid–metal DIW	~50–100 μm	Flexible electronics, circuits, and interconnects (*e.g.*, printed circuits on textiles, interconnects for wearable electronics)	High conductivity/complex handling and metal oxidation	332
Solvent-cast DIW	~100–300 μm	Polymers, composite materials, and lightweight structures (*e.g.*, lightweight bio-based packaging structures, polymer membranes)	Simple, low-cost process/long drying times, and possible deformation	314

ambient temperature, thereby avoiding the issues related to thermal and residual stress typical of FFF. After robocasting, conventional sintering can be used to compact the material. The LM-DIW technique is used for low-viscosity, low-melting-temperature metals and other conductive materials that are extruded through the nozzle and deposited onto a substrate. It is widely used to manufacture electronic and stretchable conductive materials. Polymers are mainly used in SC-DIW. In this process, thermoplastics are dissolved in a rapid evaporation solvent, and the resulting solution is extruded through the nozzle. In this case, the choice of solvent and its concentration are key factors in ensuring both rapid evaporation and the appropriate flowability,[319,320] together with a high colloid volume fraction in the ink composition, to minimize drying-induced shrinkage after printing.[319] All the DIW-illustrated technologies may require a post-processing step to harden the printed object, such as drying, heating, or sintering.[5,321] A comparison between these different DIW technologies in terms of resolution, applications, advantages, disadvantages, and practical applications is provided in Table 8.

3.2.1. DIW process parameters and material properties. The key point of all DIW processes is the rheological behavior of the ink that is inevitably influenced by the process parameters. In the case of a polymeric solution involved in energy-assisted DIW and extrusion-based DIW, to ensure consistent and controlled ink flow, shear thinning behavior is necessary when inks are extruded from the nozzle, where they are subjected to significant shear stress. According to the Herschel–Bulkley equation:[333]

$$\tau = \tau_y + K\dot{\gamma}^n \quad (1)$$

where τ is the shear stress, K is the consistency, τ_y is shear yield stress, $\dot{\gamma}$ is the shear rate, and n is the flow index, which assumes values lower than 1 for shear-thinning fluids. To be extruded, the material in the print head must undergo an applied stress greater than its yield stress, τ_y. At the outlet of the nozzle, the material recovers its τ_y and shear elastic modulus G', thus maintaining its shape and dimension.[321,334] This implies that the ink must possess sufficient mechanical strength to support the load of subsequent layers without deforming or losing its intended structure.[13] In continuous droplet-based direct ink writing (DIW), the generation of droplets is influenced not only by the intrinsic properties of the ink—such as density (ρ), viscosity (μ), surface tension (γ), and characteristic droplet size (L, typically the droplet diameter)—but also by printing parameters like droplet velocity (v) and the diameter of the nozzle (d). It is common in engineering to use dimensionless numbers to combine material properties and process parameters, thus all the aforementioned parameters can be collected in the Z number, the inverse of the Ohnesorge number (Oh), that relates inertial and surface-tension forces to viscous forces to achieve the right balance between viscosity, surface tension, and inertial forces in continuous droplet-based DIW. Z number is defined as follows in eqn (2):

$$Z = \frac{\mathrm{Re}}{\sqrt{\mathrm{We}}} = \frac{\sqrt{\rho\gamma L}}{\mu} \quad (2)$$

where Re and We are the Reynolds and Weber numbers, respectively.[335] Printing will not result in the formation of ink droplets if viscous forces are dominant (low Z). Print fidelity will decrease if inertial or surface-tension forces predominate (high Z), as ejected droplets are more likely to splash or split into many satellite droplets during printing. Generally, ideal droplet formation occurs when Z is between 1 and 10, and the droplet velocity is at least equal to $\sqrt{(4\gamma/\rho d)}$.[321] Typical values for μ, L, and v are 2–20 mPa s, 10–30 μm, and 1–10 ms^{-1}, respectively. Sometimes carbon nanotubes can be used as

rheological modifiers, enabling DIW of polymers with low viscosity, simultaneously getting multifunctionality.[336] However, printing concentrated polymer solutions or solutions containing filler particles with diameters exceeding 100 nm is quite complicated.[321] Rheological properties of DIW ink have been extensively studied.[337] It emerged that the most important parameters to evaluate the suitability of a material to the DIW process are mainly flow transition index (FTI) indicating how brittle or gradual the yielding process is (FTI $\approx$ 1 suggests brittle behavior); thixotropy and recovery time measuring how quickly the ink regains its viscosity after extrusion; Deborah number (ratio of material relaxation time to observation time; high De indicates solid-like behaviour) and Weissenberg number: (product of relaxation time and shear rate, high value indicates nonlinear flow behavior). Emerging approaches such as computational modeling, high-throughput rheology, machine learning, and materiomics, represent the emerging strategies for advanced study of DIW ink rheology.[337] Not only is the rheological behavior of the material fundamental for DIW technologies, but also two other aspects must be taken into account: paste open time and paste setting time. The paste open time is the time before the paste starts to compact in the extruder channel. For an appropriate printable paste, the open time needs to be extended to accommodate the time necessary to add the paste to the printer's reservoir barrel and wait for material deposition. A short open time facilitates the paste's quick setting in the extruder and reservoir. Thus, to extend the ink's open period, the rheological characteristics must be improved. The time the paste starts to harden is called the initial setting time, while the final setting time is when the flowability of the ink tends to zero, thus the paste is completely solidified.[314] In the case of Laser-DIW and UV-DIW, the open time is a more relevant parameter than the initial and final setting time, since the evaporation of the solvent does not determine the setting time, as it may happen in continuous-based DIW and extrusion-based DIW. Still, the setting time directly depends on the curing kinetics of the material under the input energy source. For this reason, one of the advantages of Laser-DIW and UV-DIW is the speed of the processes; in fact, solidification occurs quickly after deposition. At the same time, a low setting time avoids the spread of wet ink due to the substance's flowability, guaranteeing higher dimensional stability. However, although the setting time could be reduced in energy-assisted DIW technologies, it is worth noting that the duration of the whole process also depends on the characteristics of the light source, such as light absorbance and light penetration.[338,339] In cases where light penetration is low into the materials, it is necessary to reduce the layer thickness, necessarily increasing the process period.[338] In addition, the intensity of the UV light is a key parameter for achieving consistency in the production.[314] Substrate surface preparation is another critical factor in ensuring reliable and high-fidelity outcomes in the DIW process. The substrate's surface energy directly influences ink spreading and adhesion. The contact angle is a simple and valid method to estimate the surface energy and ink-substrate interactions. It has to be low enough to promote moderate wetting, ensuring sufficient contact without excessive spreading.[340] For example, studies using polymeric composite inks have shown that contact angles below 90° are generally favorable, and that calculating the adhesion force can help predict interfacial behavior more accurately.[340] Surface roughness is another important variable: roughening the substrate *via* sandblasting or etching can improve adhesion by increasing the actual contact area and enabling mechanical interlocking, though excessive roughness may cause irregular ink flow and edge defects.[341] Functional coatings and surface treatments, such as polymer layers or plasma treatment, have been used to adjust wettability and reduce instability in low-viscosity ink deposition.[342] In such cases, both the contact angle and the motion of the contact line (the visible edge of the droplet or filament where it touches the substrate) are indicators of stability, with unsteady contact lines often linked to filament breakup or spreading errors.[342] More advanced approaches, such as electrowetting, have also been proposed to modulate substrate wettability during printing dynamically. In the specific case of electrowetting, the application of an electric field to the substrate allows for temporarily improving its wettability. However, J. M. Löwe *et al.*[341] in their study underlined that the variability of this method was still high, so that reproducibility and control are current challenges. A consistent control over surface properties is necessary.[341] Parameters like stand-off distance between nozzle and substrate further interact with surface preparation, especially for low-viscosity inks, where smaller gaps increase the sensitivity to substrate wetting behavior.[342] Overall, effective surface preparation for DIW involves not only matching surface chemistry to ink properties but also carefully managing roughness, surface treatment uniformity, and interfacial dynamics. The layer-by-layer deposition process characteristic of DIW poses challenges in preserving structural stability, especially when printing intricate shapes. To ensure the printed structures remain secure, the use of well-designed support systems is essential. Continued research can help optimize these support techniques and minimize deformation, leading to greater printing precision, enhanced structural integrity, and reduced need for post-processing.[343] As for the other material extrusion process, *e.g.*, FFF, the most common post-processing methods are sanding or surface polishing to smooth the surface imperfections, gap filling (for example, with epoxy/filler mixture), and coating to improve the aesthetic appearance or for functionalization and protection.[344] In the case of energy-assisted DIW, a secondary curing process is employed because the initial polymerization—typically triggered by UV light or heat—forms polymer chains but does not fully react all monomers. Residual monomers are then eliminated through additional heat treatment or further UV exposure. These secondary curing steps can also be used to modify the material's properties or alter the shape of the 3D printed object to reach its final configuration.[5]

Apart from material properties, since DIW technologies are very similar to the FFF process, the majority of printing parameters related to the asset of the machine are the same, such as

Table 9 Effect of DIW process parameters on the final objects

Parameter	Effect	Ref.
Printing pressure	• Volumetric flow rate • Resolution of miniaturized electronics • Residence time of material in the flow channel • Printing speed	345
Nozzle diameter	• Die-swell phenomenon	346
Printing speed	• Consistency of deposited trace	346
Energy source (400–800 nm)	• Strength of the final object • Resolution • Need for post-process • Time to start the photoreaction	328, 347 and 348

nozzle diameter, ink flow rate, height of the layer, filling pattern, printing speed, filling density, chamber temperature and humidity, and building orientation. To these parameters, printing pressure and energy source characteristics have to be added.[314] Their effects are summarized in Table 9, while a case study on the parameter optimization for dimensional accuracy is provided by Y. Tu *et al.*[349]

Although polymer and polymer composites for DIW processes have been extensively discussed in the literature,[350] and researchers are working on advanced polymer formulations,[351] the application of smart materials printed *via* DIW in the aerospace and aeronautical sectors is still a poorly explored field. A. White *et al.*[352] used a 2-axis nScrypt material extrusion system, similar to that recently employed by NASA in parabolic flight tests, for printing polyvinylidene fluoride–trifluoroethylene (PVDF–trFE) ink. It is a flexible, biocompatible, and chemical-resistant material capable of detecting impact forces due to its piezoelectric properties. In this study, PVDF–TrFE films were reliably fabricated with a thickness of approximately 40 μm, demonstrating a notable piezoelectric coefficient reaching up to 25 pC N^{-1}. Furthermore, a fully printed dynamic force sensor was developed, achieving a sensitivity of 1.18 V N^{-1} through the combined printing of commercial conductive silver inks and customized PVDF–TrFE inks. K. Gao *et al.*[353] studied a new polyaryletherketone (PAEK)-based DIW ink, enhanced with *N*-vinyl-2-pyrrolidone (NVP) and polyethylene glycol diacrylate (PEGDA). These additives enable photocuring and cross-linking, giving the printed parts high tensile strength (42.6 MPa), thermal stability (T_d = 246 °C), and exceptional shape memory performance (fixation >93%, recovery >100%). Since PAEK is a high-performance engineering plastic known for its excellent mechanical properties and thermal resistance, the new modified ink functioned effectively as a high-temperature actuator, demonstrating its potential for aerospace and other demanding applications.

Other peculiar examples of composites and nanocomposites printed *via* DIW, which have the potential to be applied in the aerospace and aeronautical sectors, are reported in Table 10.

3.2.2. Application of DIW printed parts in the aeronautical and aerospace sectors. Currently, some DIW technologies (drop-on-demand and continuous inkjet) are already industrialized for the decoration of surfaces, and exterior printing/patterning on large parts with automated systems. In addition, the research community is moving in the direction of applying DIW processes to fabricate passive electrical components, electronic circuits, sensors for structural health monitoring

Table 10 Effect of filler in DIW-printed polymer composites

Composition	Properties	Ref.
TPU-multi-walled carbon nanotubes and graphene nanoplates	Thermal conductivity of the polymer composites increased nearly sevenfold (from 0.36 W m^{-1} k^{-1} to 2.87 W m^{-1} k^{-1}), and the electrical conductivity increased up to 5.49×10^{-2} S m^{-1}.	354
PDMS-carbon nanotubes-silica nanoparticles	Durable, extremely deformable, and sensitive piezoresistive response (gauge factor of about 16 at 1% max strain, and a gauge factor of about 5 at 15% max strain). Increasing the microscale porosity enhanced the piezoresistive sensitivity of the conductive polymer nanocomposite structure more than the macroscale porosity (dual scale porosity) of about 67%.	355 and 356
PVDF-boron nitride (BN)	400% increase in in-plane thermal conductivity. The lithium-ion half-cells made with the PVDF-BN show stable cycling performance at a 1C charge–discharge rate for 250 cycles with 90% capacity retention.	357
Silicon elastomers reinforced with TiO_2, Al_2O_3, and graphite	Reduced vibrational damping and shockwave mitigation.	358
Aliphatic urethane diacrylate and isobornyl acrylate – carbon nanotubes	Sample with 2 wt% MWCNT had the highest sensitivity of 8.939 with linearity up to strain of 45%, a strain detection range of ~60%, a low detectable limitation of 0.01%, and a high mechanical durability for 10 000 stretching–releasing cycles	359
PEDOT/PSS-MXene	High electrical conductivity (1525.8 S m^{-1}), flexibility, stretchability, and fatigue resistance.	360
Elastomeric and rigid thermosetting polymer inks – ZnO functionalized carbon fibers	ZnO functionalized epoxy composites achieve a Young's modulus of 3.69 GPa, which is 15.3% higher than pristine fiber-reinforced composites; enhanced the fiber/matrix interface strength, with improvements of 57%, ZnO nanowires enhance the heat transfer rate of carbon fibers by 17% considering the same heating time	361
Polycarbosilane (PCS)–Chopped carbon fibers (C_f)	Annealed DIW printed PCS-C_f produced. C_f/SiC fibers. C_f/SiC composite with 30 wt% C_f content has high bending strength (~7.09 MPa) and negligible linear shrinkage (~0.48%)	362
Epoxy – nanoclay-Kevlar fibers	Static flexural strength and modulus of 108 ± 13.37 MPa and 4.23 ± 0.29 GPa were attained for 6.3% Kevlar fiber reinforced composites, respectively.	363

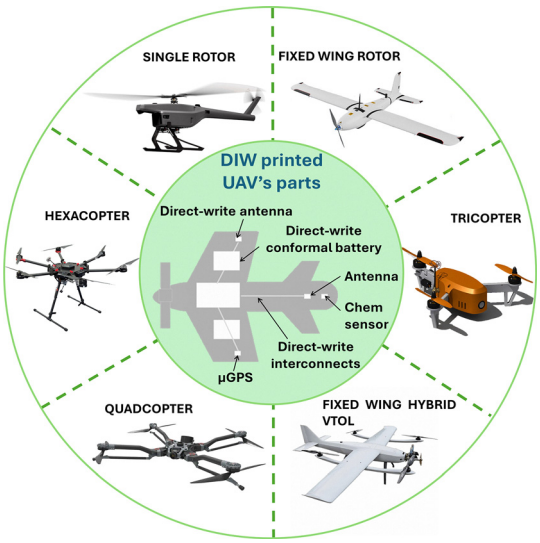

Fig. 14 DIW printed devices for a micro-air vehicle.[365]

(SHM), gases, batteries, and wireless antennae for communications, and polymer solar cells for UAV applications.[364] In this regard, Fig. 14 shows DIW printed devices for a micro-air vehicle,[365] applicable to different types of UAVs.

Moreover, NASA's Glenn Research Center has developed a variety of polymer aerogel formulations that are printable *via* DIW technology, promoting the applicability of aerogels with controlled complex shapes for thermal and acoustic insulation, vibration mitigation, sensors, antennas, *etc.* Among the main advantages, NASA highlighted the possibility of chemically bonding different polymer aerogel formulations layered in a gel state, thereby immediately eliminating the need for adhesives and the solvent removal phase (*e.g.*, supercritical fluid extraction).[366] Low-cost, short-range optical connection technology is crucial for high-speed data transmission at the board level. Lin *et al.*[367] produced an optical waveguide for optical interconnects by DIW printing polymethylmethacrylate (PMMA) polymer. The researchers effectively fabricated high-density, multilayer waveguide arrays—specifically, a four-layer structure comprising 144 individual channels. Each channel demonstrated error-free data transfer at a rate of 30 Gb s^{-1}, showcasing the printing technique's capability to produce optical waveguides with outstanding transmission quality. Ho *et al.*[368] exploited the extrusion DIW to fabricate carbon electrochemical capacitors and zinc-manganese dioxide micro batteries. The authors used poly(vinylidene fluoride hexafluoropropylene) (PVDF) as a polymeric binder and *n*-methyl-2-pyrrolidone (NMP) as a solvent. They confirmed that DIW technology is a valid method to produce multilayer structures with a limited area. The electrochemical capacitors had the capability to cycle more than 120 000 times without significant performance loss (average areal capacitances of 100 mF cm^{-2}), while printed micro-batteries cycled over 70 times with an average capacity of 1 mAh cm^{-2} and 1.2 mAh cm^{-2} areal energy density. The advantage of using the DIW process for electronic circuits is the possibility of locally processing the material using, for example, a laser source, even on large structures, where conventional oven curing is not practical, especially in the aeronautical sector. NASA's Goddard Space Flight Center (GSFC) invested in printing traces for CubeSat flex circuitry and also used DIW technologies on three-dimensional geometries for miniaturized detectors and electronic assemblies.

Polymer-based ink filled with micron-sized particles of copper, gold, and silver, or nanometric carbon-based particles, has been printed to form conductive tracks on a variety of substrates.[369] Although silver-based inks represent the best tradeoffs between conductivity and cost, graphene is also an inexpensive conductive material that can be integrated with difficult substrate materials such as soft and flexible textiles. Due to these factors, as well as the exceptional electrical and mechanical properties of graphene, graphene-based conductive inks have the potential to completely transform the printed electronics industry by substituting metallic components for conventional inks.[370] Moreover, soft robotics is being studied for various space applications, including planetary stations, spacecraft, and assets, in low-gravity and confined spaces. These applications include navigation, observation, and even component maintenance. For instance, in an emergency, like a spacecraft experiencing a pipe system failure, a soft robot might be able to help navigate the structure and identify the position and source of the failure.

Furthermore, in space, the ability to fabricate soft robotic tooling in a single step is essential, and currently, it is only possible with 3D printing technology.[371] In this scenario, Demirkal and colleagues[371] introduced a new UV-resistant elastomer designed for fabricating structures that integrate electrical interconnects and sensors capable of monitoring temperature and strain directly, tailored for space-related uses. They employed a highly flexible, silicone-based elastomer characterized by low or minimal toxicity, using a thiol-ene click chemistry approach to enable fast polymerization and maintain structural integrity throughout the printing process. Tethers Unlimited, Inc. (TUI) and Western Washington University (WWU) proposed the ''Resin Additive Manufacturing Processed Thermal Protection System'' (RAMP TPS) project,[372] whose goal is the development of an *in situ* cured spacecraft heat shield material processed *via* DIW. As part of the RAMP TPS project, a specially formulated benzoxazine resin composite—enhanced with carbon fibers, silica microballoons, curing agents, and viscosity control additives—was employed to maximize mass efficiency by combining a refined material blend with strategically graded, low-density printed core structures. Soon, this innovative heat shield technology will be utilized in the manufacture of automated re-entry vehicles (such as those for lunar exploration missions, Mars sample missions, and asteroid sampling missions) and in-space servicing procedures.[372]

On the other hand, Marnot *et al.*[373] tried to formulate a high-solid suspension for rapid manufacturing in future space missions covering the gap of materials compatible with the unique environments, such as that of the Lunar surface. The main difficulty was achieving success in DIW printing a photopolymerizable binder composed of hexyl acrylate (HA) and

PEGDA monomers, at −30 °C. The authors demonstrated that despite lower cure kinetics, it could be possible to obtain similar mechanical properties of the DIW ambient temperature printed object by adjusting the composition of the ink (in that case, by increasing a small copolymer quantity of poly(ethylene glycol)diacrylate (PEGDA) and decreasing the linear HA chains). Although it represents a pioneering experiment in the space field, it surely opens up the translation of DIW technology from ambient conditions to new and challenging environments.

From these examples, it is evident that DIW technologies are mainly investigated for aerospace applications rather than for aeronautical ones. By enabling precise, on-demand fabrication of functional materials, from aerogels and waveguides to soft robots, batteries, and heat shields, DIW supports the integration of complex, multi-material systems with minimal post-processing. Its compatibility with various formulations, including UV-curable and cold-environment printable inks, further highlights its potential to revolutionize *in situ* manufacturing for space missions and next-generation printed electronics. However, despite its versatility, DIW still faces notable limitations, including material formulation challenges, slower printing speeds, limited resolution compared to other additive methods, and sensitivity to environmental conditions such as temperature and humidity. Overcoming these hurdles, especially in off-Earth or *in situ* applications, will require continued innovation in rheology control, curing strategies, and ink chemistry, particularly for harsh or non-standard environments like deep space or the lunar surface.

3.3. Stereolithography (SLA)

Stereolithography (SLA), whose working principle was published in 1981 by Dr. Hideo Kodama, was the first 3D printing technology to be patented by Charles (Chuck) Hull in 1986. This technique uses an irradiation light source whose energy is required to cure or solidify a liquid-photosensitive polymeric mixture. The apparatus consists of a UV lamp with a wavelength that varies between 300 and 400 nm, depending on the SLA machine, and a reservoir that holds the liquid photosensitive monomers. However, few prepolymers or monomers can absorb UV light; for this reason, it is necessary to add organic molecules with a low molecular weight, known as initiators. A photochemical reaction happens as the excited species forms. The exothermic polymerization process involving a chemical cross-linking reaction is correlated with the curing mechanism. The system's physical characteristics alter throughout this phase. It passes from a liquid to an insoluble, solid form by gradually increasing its viscosity, which is followed by a gelation and hardening phase. Thus far, there have been significant advancements in stereolithography, and several strategies have been developed for these systems. Huang *et al.*[374] classified the SLA techniques into four generations in chronological order: scanning laser beam, projection stereolithography, liquid interface production, and volumetric stereolithography. In laser scanning stereolithography (LS-SLA), a system of mirrors was developed to focus the laser beam onto the resin surface, curing it according to the CAD model (Fig. 15a). In some cases, mirrors

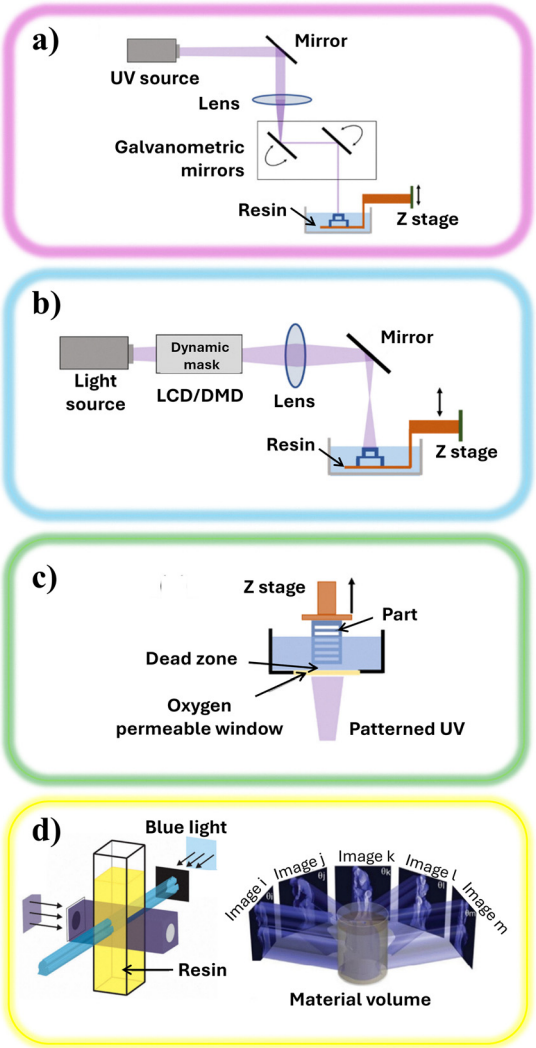

Fig. 15 Scheme of: (a) scanning laser beam; (b) projection stereolithography; (c) liquid interface production; (d) volumetric stereolithography. Reproduced with permission from ref. 374. Copyright 2020 MDPI.

were moved to change the laser beam trajectory in the *X*–*Y* directions, while the building bed was motorized to move along the *Z* axis from one layer to the next.[375] In other cases, mirrors and the laser beam were fixed in unique optical systems that moved in the *X*–*Y* directions, or again, the beam was fixed on the resin, and the platform moved in all three directions. Due to the long processing time and low efficiency, the second generation of SLA was introduced. Projection stereolithography is a well-known term for digital light processing (DLP). The main difference between the previously described SLA printing and the DLP process is that the 3D printing machine is able to build 3D objects by curing each layer simultaneously through a single exposure by projecting mask patterns onto the resin surface (see Fig. 15b).

The mask is obtained by using a liquid crystal display (LCD) or a digital micromirror device (DMD) to direct UV light and polymerize the resin. The LCD generates dynamic masks by changing the pixel state from transparent to opaque[376]

while the DMD is a matrix of micro mirrors whose orientation can vary to divert the light in a controlled way in different directions and generate the image to be projected.[377] Although DLP machines are faster and cheaper than SLA printers, they cannot match the smooth surface finish of SLA parts. To speed up the process, continuous liquid interface production stereolithography (CLIP-SLA) was developed, allowing for continuous exposure of the material to the UV source without interruptions from layer to layer. As shown in Fig. 15c, a persistent liquid interface (dead zone) with an oxygen-permeable window, located below the UV image projection, prevents photopolymerization between the window and the polymerizing part during platform elevation.[378] CLIP has demonstrated impressive performance, achieving build rates up to 100 liters per hour and resolutions as fine as 4.5 μm. Despite these capabilities, it faces several limitations. The process is restricted to low-viscosity resins, which narrows the range of usable materials and poses challenges for incorporating biodegradable options. Moreover, support structures are necessary when printing complex geometries. Additionally, at higher resolutions, the process can no longer maintain a consistent upward motion of the printed object, which affects production continuity.[379]

The most recent SLA technology, volumetric stereolithography (V-SLA), enables the production of 3D objects not layer by layer, but by building 3D volumes as a single unit operation (Fig. 15d). UV beams are focused on the resin in the building area from the three orthogonal directions while the resin is stored in a rotating cuvette. By adjusting the compensation between each beam, a single exposure is enough to obtain a V-SLA printed object according to the CAD model.[380] This method achieves volumetric build rates of up to 55 mm^3 s^{-1} and resolutions of approximately 25 μm in the x–y plane and 50 μm in the z-direction, positioning V-SLA as a promising solution for high-speed, high-resolution 3D printing at the micron scale.[379] A further improvement in SLA printing comes from the light source. Although the aforementioned technologies can resolve 20 μm, to guarantee a good quality of restricted controlled porous structures, a new technique called two-photon polymerization (2PP) was developed, whose resolution goes down to 100 nm.[381] Also in this case, the material must be photosensitive; however, instead of a UV source (350–400 nm), 2PP uses a femtosecond near-infrared laser (700–800 nm) in a pulse mode. The light can pass through the resin without initiating the reaction. Only when two photons are combined at the same point does the material undergo local polymerization. Although 2PP-based techniques offer significant advantages, they encounter challenges such as slow printing speeds caused by the narrow fields of view in high-resolution systems, limited working volume, and limited selection of compatible materials.[382] For this reason, 2-PP use for printing polymeric structures/devices applicable in the aerospace and aeronautical sectors is still limited. However, recent developments in scanning technologies, parallelization methods, photoreactive materials, and accelerated photopolymerization processes are actively working to overcome these obstacles.[383] A schematic representation of this more accurate SLA process is shown in

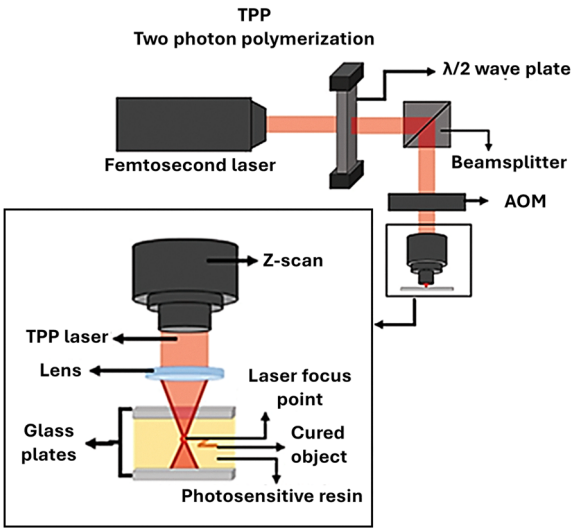

Fig. 16 A two-photon polymerization (2PP)-SLA process. Reproduced with permission from ref. 102. Copyright 2021 Wiley.

Fig. 16. For LS-SLA, P-SLA, and CLIP-SLA, a further distinction can be made between top-down and bottom-up sequences of layer deposition based on the direction of growth (Fig. 17). In the first case, the building bed is positioned on top of the resin reservoir, and the UV source is placed above it. Once a layer is cured, the movable platform lowers, allowing the required quantity of liquid resin, constituting the new layer, to be cured and cover the item (Fig. 17a).

In the bottom-up approach, the movable platform is located close to the reservoir's bottom (see Fig. 17b), and the liquid resin fills the space between the platform and the container bottom. Thus, the UV source is located below the reservoir. As the layer is fully cured, the platform moves up to a height necessary to allow the uncured resin to reach the bottom again, forming the next layer.[384]

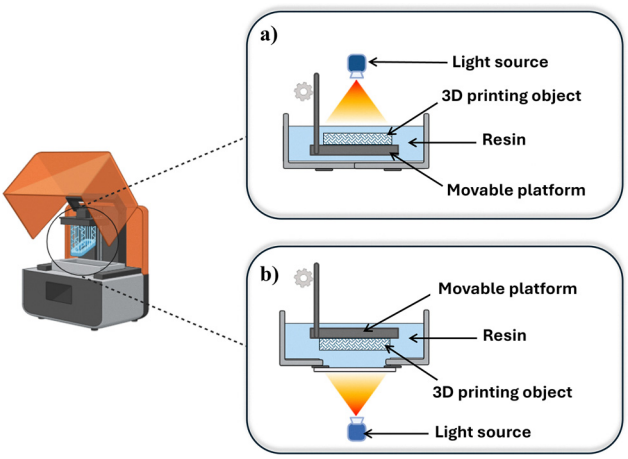

Fig. 17 Schemes of two types of stereolithography setups: (a) bottom-up system and (b) top-down setup. Adapted with the permission from ref. 384. Copyright 2018 MDPI.

3.3.1. SLA process parameters and material properties. The main process parameters of SLA that significantly impact the quality, accuracy, and strength of the final printed object are laser power, scan speed, layer thickness, scan pattern, hatch spacing, overcure, and exposure time. While the concepts of layer thickness and scan pattern are already known from other 3D printing technologies, such as FFF, the remaining parameters are presented in this paragraph. It is worth noting that mathematical relations strongly interconnect all these parameters. More in detail, the resolution of the SLA printed object depends on the curing depth (C_d) and curing width (C_w). According to the Beer-Lambert law:

$$C_d = D_p \ln \frac{E}{E_c}$$

$$C_w = w_0 \sqrt{\frac{2C_d}{D_p}}$$

The parameter C_d is related to the penetration depth D_p, the maximum exposure energy E, and the critical exposure energy E_c, which is the minimum energy required to trigger polymerization and convert the resin from a liquid to a solid state.[96,385] The penetration depth D_p refers to the depth at which the light intensity falls to $1/e^2$ (approximately 37%) of its initial value at the resin's surface.[386] This depth is determined by the inherent characteristics of the resin composite, including the concentration and size of the nanoparticles, as well as the refractive indices of both the particles and the liquid resin. Incorporating an optical absorber into the photosensitive resin allows precise tuning of the light penetration depth.[101] Photoinitiator and liquid monomers determine the value of E_c. Laser power influences the value of the maximum exposure energy E, which can be calculated as follows:

$$E_{max} = \sqrt{\frac{2}{\pi}} \frac{P}{w_0 v_s}$$

where P is the power of the laser at the surface of the resin, w_0 is the beam radius, and v_s is the scanning speed.[386] From these equations, it can be deduced that when D_p assumes low values due to a significant difference between the refractive index of the nanoparticle and the liquid resin, the curing depth will be lower, and laser light will be scattered. It follows that the penetration depth constrains the layer thickness, and if it is very low, the process duration increases. At the same time, it is not possible to increase the scan speed significantly, as this would again result in a decrease in C_d and C_w. For the same reason, micro-stereolithography based on a small beam radius, on the one hand, guarantees a high resolution of the final piece, but on the other hand, it requires a long time.[96] The concept of hatch spacing and overcure is illustrated in Fig. 18. Hatch over-curing refers to the portion of the hatch stand of the new layer overlapping the previous one due to the extension of the penetration depth. Hatch spacing, on the other hand, is the distance between two adjacent hatch overcures. The hatch over-curing also depends on the layer height and penetration depth,

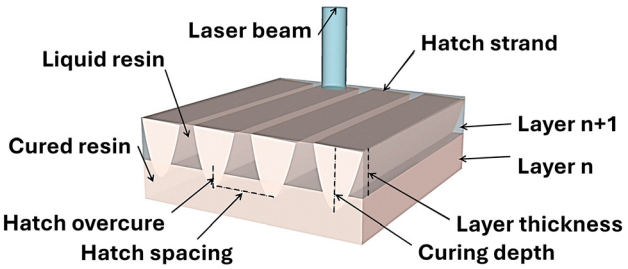

Fig. 18 Scheme of some of the SLA parameters. Reproduced with permission from ref. 386. Copyright 2020 Elsevier.

as can be noted in Fig. 18. Exposure time is the interval of time during which UV light is focused on the same portion (*e.g.*, the same layer) of the under-construction structure to allow the resin to cure. The effect of these parameters on the final SLA printed object is summarized in Table 11, and a strategy for their control and optimization is the Taguchi method, a statistical model, successfully applied by N. D. Borra *et al.*[387]

The primary SLA restriction is the selection of materials, as only photosensitive liquids are permitted. In addition to chemical and optical properties (*e.g.*, transmission, absorption, reflection, and scattering), which strongly affect the kinetic and cure degree, SLA materials must respect rheological constraints. The viscosity of materials ranges from 0.1 Pa s for low-molecular-weight molecules to 10 Pa s for high-molecular-weight.[388] A high viscosity of the polymer causes a high surface tension on the freshly applied thin film, which assumes a convex shape.[386] In the case of highly viscous monomers, heated reservoirs could be used; however, it is a very uncommon choice, especially for industrial applications.[388] A comprehensive list of fuel-based materials for SLA printing is provided by Bagheri *et al.*[98] in their review. In the last few years, researchers have made efforts to develop new bio-based resins suitable for SLA processes. Works by V. S. D. Voet *et al.*[101,389] and by G. Zhu *et al.*[390] represent some efforts in developing bio-based resins for SLA printing. Although many papers deal with the photopolymerization of biodegradable resins, only a few have succeeded in completely degrading the building material. For this reason, CANs have gained more

Table 11 Effect of SLA parameters on the final properties of the printed object

Parameters	Effect	Ref.
Hatch spacing	• Cure degree of layer (presence of overlapping between cured regions, or of uncured resin region)	96 and 386
Hatch overcure (10%–35% of the layer thickness)	• Shrinkage	
Hatch strand		
Layer height	• Hatch overcure • Adhesion properties	96 and 386
Exposure time	• Mechanical properties • Over-curing	397

attention in the SLA process.[389–392] CANs, interpenetrating polymer architectures, or elastomeric modifiers can significantly enhance the flexibility and fatigue resistance to mitigate brittle fracture and microcrack formation in SLA printed sensors.[393]

Alejandra Durand-Silva *et al.*[89] studied the effect of a thermally reversible Diels–Alder cross-linker on the shape stability of photoprintable resins and their self-healing properties. The authors demonstrated that a dynamic covalent cross-link concentration of 1.8 mol% was enough to provide 99% self-healing efficiency without disrupting the shape stability of the printed objects. Z. Zhiheng *et al.*[394] added fragmentation chain transfer (RAFT) agents into resin formulations to allow visible light (405 nm) mediated 3D printing of materials with self-healing capabilities. The authors demonstrated the reactivation of the RAFT agent embedded in the thermosets under UV light (365 nm), which enables reformation of the polymeric network. H. Kim *et al.*[395] optimized the solvent (*N*,*N*-dimethylformamide, DMF) to PVDF ratio and PVDF solution to photopolymer resin (PR) ratio to enhance the dispersion of the PVDF into the PR to achieve high piezoelectric performance. The results demonstrate that a ratio of 1 : 10 (PVDF : DMF) and 2 wt%-PVDF/PR was optimal for the best dissolution of the PVDF, 3D printability, and piezoelectric properties. Under these conditions, the blend generated ±0.121 nA under 80 N dynamic loading excitation. Recent studies on SLA for producing piezoelectric devices primarily concentrate on printing photosensitive composite slurries with piezoelectric properties. However, these composites often exhibit limited piezoelectric performance, mainly due to the low solid content in the slurry and challenges associated with maintaining its stability over extended periods.[396] Wang *et al.* grafted the surface of the piezoelectric ceramic powder with oleic acid to enhance the matching between the piezoelectric ceramic and the polymer matrix (photocurable thermosetting resins) in the formed piezoelectric composite material. The results revealed that 72 wt% paste prepared with oleic acid-grafted and modified piezoelectric ceramic particles had good stability, and the piezoelectric voltage constant of the piezoelectric composites fabricated with the paste was 220.2×10^{-3} Vm N^{-1}, and the piezoelectric sensitivity after topology optimization could reach 30 mV kPa^{-1}.[396]

More challenging materials include nanocomposites and composites, as the filler dimensions must be smaller than the wavelength; otherwise, the UV rays would be dispersed or even blocked. Moreover, the addition of finer particles increases viscosity, causing issues during the passage from one layer to another and in hollow structures. Different dispersion methods[385,398] or surface chemical modification of the filler[385] were experimented with to limit the phenomenon of self-association of nanoparticles, which could worsen the mechanical properties of the final item and increase process complexity.

O. W. Saadi *et al.*[393] in their review on SLA-printed piezoresistive sensors found limited exploration of smart materials (including shape-memory polymers and self-healing polymers) together with piezoresistivity. Future investigations could focus on incorporating multifunctional smart materials to broaden the range of applications for SLA-printed sensors beyond just strain detection. Additionally, adopting bio-inspired designs and lattice-based structures may improve mechanical strength by promoting better stress distribution and enhancing resistance to repeated loading. In the specific case of aerospace and aeronautical sectors, embedding piezoresistive strain sensors within interpenetrating phase composites (IPCs) and aperiodic lattice frameworks represents a promising avenue for future research. IPCs are composed of robust, load-bearing hard phase—such as lattice or truss structures—interwoven with a softer, compliant phase. These composites achieve enhanced damage resistance and energy absorption through the interaction between the hard and soft phases. Incorporating strain sensors produced *via* SLA could allow for real-time tracking of strain development, monitoring of cyclic loading behavior, and early detection of failure processes.

Additionally, researchers attempted to modify the machine asset to enhance filler dispersion in the resin. Magnetic,[399–401] electrical,[402] and acoustic field[403] were exploited to induce the orientation of filler nanoparticles, contributing to the improvement of the final properties of smart components with complex shapes.[404,405] Not only nanoparticles but also chopped and mat materials have been demonstrated to be possible to include in an SLA-printed sample. Sano *et al.*[406] were the only ones to try to UV-cure epoxy resin and glass fibers in three different forms: powder, chopped glass fibers, and in the form of a fabric. These examples open up the opportunity to obtain smart materials *via* the SLA process, which is applicable in the aerospace industry.

3.3.2. SLA printed parts in the aerospace and aeronautical sectors. The aerospace and aeronautical sectors utilize SLA technologies for parts that are not typically intended for structural applications, where load-bearing is the primary function. Instead, they are being considered for pseudo-structural roles, such as positioning sensors, wires, or other lightweight components; providing isolation between elements (*e.g.*, electrical, magnetic, or EMI); offering shielding against light, low-energy radiation, or electric fields.[407] The Goddard Space Flight Center (GSFC) of NASA completed a project on micro-additive manufacturing between 2016 and 2017, aiming to fabricate new sensors at the micro-scale with features impossible to replicate *via* traditional methods. For this reason, they combined micro-SLA technology with chemical vapor deposition (CVD). An intricate structure was first manufactured *via* micro-stereolithography and Nanoscribe's 2-photon process, employing a polymeric material. Then, a thin shell of refractory materials, such as fused quartz and boron, was deposited on the polymeric support using low-temperature CVD. Ultimately, the polymeric structure acting as a mold was dissolved in a solvent, and a second CVD step was performed at a higher temperature. The innovation of this project lies in the use of an SLA high-resolution printed support, which enables the CVD process at atmospheric pressure to reach microscopic interior features and deep voids.[408] In another research activity, NASA combined the SLA process with copper–nickel electroplating to

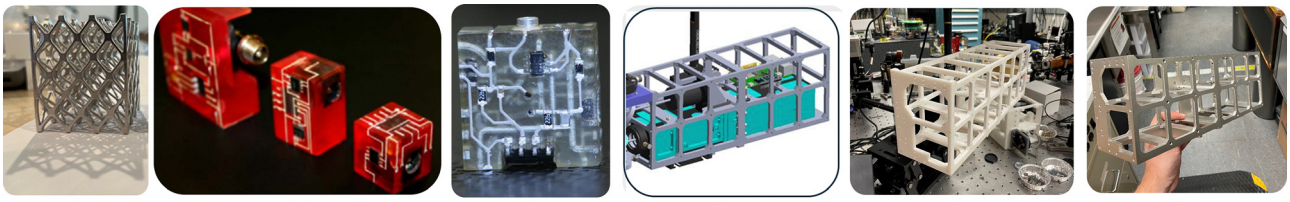

Fig. 19 Examples of SLA printed parts for aerospace applications: (a) electroplated SLA printed lattice structure;[409] (b) four generations of 3D magnetometer systems. Reproduced with permission from ref. 410. Copyright 2014 Springer Nature; (c) SLA printed circuit based on the NASA benchmark circuit. Reproduced with permission from ref. 411. Copyright 2014 IEE; (d) scheme of the KArLE system;[409] (e) SLA printed structure of the KArLE system before electroplating;[409] (f) SLA printed structure of the KArLE system after electroplating.[409]

increase the structural strength of resin-based components, and, at the same time, to study the feasibility of substituting metal components with less expensive, less massive, faster-produced ones compared to those obtained *via* conventional computerized numerical control (CNC) machining of metals.[409] After a preliminary characterization of the mechanical properties of an electroplated SLA-printed lattice structure (see Fig. 19a), a real object was produced. The KArLE (Potassium Argon Laser Experiment) Optical system is an instrument used to accurately determine the age of lunar samples (geochronology) on the Moon's surface. Thanks to the use of SLA technology, the KArLE system was built by assembling only two parts rather than 12, reducing both time (three times faster to produce) and mass. Then, a copper–nickel coating of ~150–400 μm was electroplated to improve the mechanical properties. A schematic of the KArLE system and the real images before and after electroplating are shown in Fig. 19d–f.

A four-generation 3D magnetometer system with off-axis component placement and conducting routine, which includes a microprocessor, LEDs, a DC connector, and three orthogonally placed magnetic Hall effect sensors, is illustrated in Fig. 19b.[410] This is an example of the progressive improvement in volume savings by exploiting all the advantages of the SLA process (*e.g.*, resolution and accuracy). Fig. 19c reports a circuit design that accomplishes component layout by making use of all of the surfaces present in a pre-defined volume. Additionally, the routing has utilized the device's interior volume, in addition to all accessible surfaces.

The original gadget was a signal conditioning circuit, whose schematic was made available by NASA's Johnson Space Center engineers as a benchmark circuit to demonstrate the volumetric efficiency of 3D-printed electronics. As can be seen, the circuit volume was significantly decreased from the original design to a volume of $0.5'' \times 0.5'' \times 0.125''$, with a component and trace density of 27%.[411] Getachew *et al.*[412] in a recent review reported some examples of real components that can be manufactured *via* SLA, such as ducting components with intricate geometry for air conditioning, ventilation, and fluid systems; intake and exhaust components for lightweight engines; high-precision actuators; customized aerospace brackets; electrical connectors for communication, power transmission, and control; fuel system lightweight elements suitable for harsh environments; and aerospace housings.

V-SLA shows strong potential for IN-space manufacturing because, unlike traditional layer-by-layer methods, it does not depend on maintaining a flat liquid–gas interface during the printing process. With further development, V-SLA could enable the production of various components for space missions, including organic tissues, flexible seals, rigid structural elements, and fine microstructures, as well as support on-site repairs of tools and equipment.[413] In May 2022, a system called "SpaceCAL" was tested during a microgravity parabolic flight, aiming to assess the feasibility and performance of V-SLA in a weightless environment. Early results indicate that a low-viscosity precursor (0.12 Pa s) can be successfully printed in microgravity, with reduced geometric distortion compared to printing under Earth's gravity. SpaceCAL integrates five CAL printing systems into a single payload and was specifically designed to fabricate complete parts within 20–28 second windows of simulated Martian, Lunar, and microgravity conditions during a parabolic flight. As a successful demonstration of CAL's capabilities in reduced gravity, the system was operated during flight and produced 154 individual parts using five different materials. To showcase the printing precision in microgravity, several complex geometries—including miniature rocket models—were fabricated. Additional examples, such as polymer structures printed over metal components, flexible O-rings, and soft biomaterial tubes, highlight CAL's versatility for both repair tasks and bioprinting applications. This experiment demonstrated that CAL can handle a diverse range of materials within a single system. It is important to note that only the light-based exposure stage of the CAL process was carried out during flight; post-processing was completed afterward. To assess the whole process, including power consumption and volume requirements relative to other IN-space manufacturing methods, a dedicated flight-ready version of SpaceCAL is currently under development.[413]

Different from the FFF process, SLA technology is mainly employed in aerospace applications. In this context, SLA technology ranges from sensor integration and radiation shielding to miniaturized, high-density 3D electronic circuits. The primary limitation of SLA-based technologies remains their inadequate mechanical strength and thermal resistance for primary load-bearing or structurally critical aerospace components. SLA parts still fall short of replacing metals or composite materials used in conventional aerospace-grade components. Post-

processing requirements—such as the need to remove sacrificial polymers or perform high-temperature treatments---introduce additional complexity, reducing SLA production speed. Full in-space operability has not yet been achieved, remaining a challenging goal to work on in future research activities.

3.4. Materials jetting (MJ)

SLA, Laser-DIW, and UV-DIW are 3D printing technologies based on the photocuring of the deposited resin; however, their main limitation is the presence of a single resin container that allows for the printing of a single material or in a more sophisticated way, it is necessary to empty, clean and refill the reservoir to change the material resulting in a long-time consuming and discontinuous process. Materials jetting (MJ), also known as PolyJet, is a 3D printing method capable of simultaneously depositing multiple materials. To achieve this, the MJ machine is composed of a jetting head containing 4 or more printing heads (depending on the machine model[414]), each loaded with a different material. Each material is selectively jetted in the form of hundreds of droplets from many nozzles that constitute one of the printing heads. For example, the Stratasys J750 printer is composed of four printing heads in total, each with 96 nozzles of 10 μm diameter.[415] On both sides of the jetting head, two UV lamps are allocated in such a way that they move simultaneously with the jetting head. Once the materials are ejected to form the entire layer, the jetting head continues in the same direction as material deposition, allowing the UV light to cure the layer and solidify it.[416] The asset of the jetting head of the MJ printer is shown in Fig. 20. After the layer is completed, the building platform moves down a height equal to the layer thickness, and the process is repeated until all the object is obtained.

Additionally, during this 3D printing process, a sacrificial, hydrophobic support material can be used to prevent the collapse of parts when necessary. Typically, the supporting material is a gel-like photopolymer that is easily removed manually or by using a water jet cleaning station.[417] MJ technology enables the attainment of high finishing quality, thanks to a layer thickness in the range of 16 μm to 30 μm and an in-plane resolution of 42 μm.[416–418]

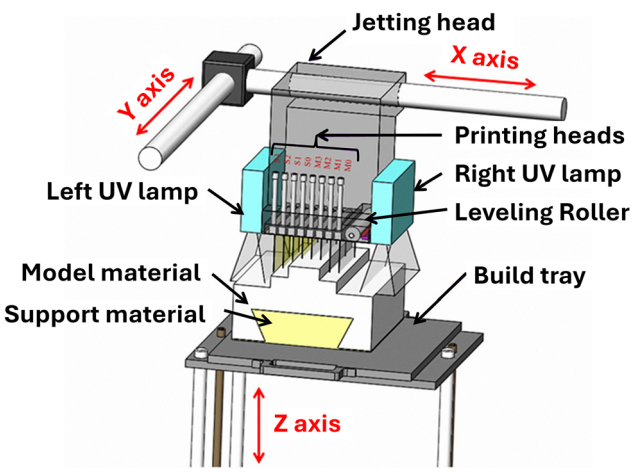

Fig. 20 A schematic representation of a Material Jetting 3D printer. Reproduced with permission from ref. 416. Copyright 2019 Springer Nature.

The advantage of using different materials implies that the CAD model has to be adequately prepared. To associate material or color to a determinate portion of the object to be printed, it is necessary to model the item as an assembly of distinguished bodies (CAD sub-models). As usual, the assembled CAD has to be saved in a unique STL file. During the CAM phase, a specific color or material will be assigned to each body of the as-prepared CAD model.[419] Tessellation approximations and constructed CAD sub-models representing multi-material regions can be the primary causes of loss of geometric description. Consequently, the mechanical properties of multi-material composite parts can be adversely affected, resulting in unsatisfactory print quality.[420] However, some commercially available printers employ an alternative approach known as voxel printing technology. The concept of a voxel is similar to that of a pixel, but intended for use in three dimensions. Using voxel printing, one may construct engineered multi-material composite parts by modifying a CAD geometry voxel by voxel, defining related materials, and creating variations for each voxel.[419,421] Since voxel printing is based on a bitmap picture for each printing layer, it is first necessary to digitally slice the object. In this way, it is possible to create multi-material, intricate structures with high resolution without modifying the CAD model or the STL information. Not only can multi-material items be produced, but also illusory-effect, multi-colored parts can be created thanks to the voxel strategy.[422] For basic printers, basic colors are combined according to the RGB system to create a wide gamut of colors. According to the RGB (red, green, and blue) system, color is obtained by assigning an integer value from 0 to 255 to the R, G, and B parameters. For example, black is obtained by the sequence (0,0,0) while white is defined by the sequence (255, 255, 255).[423] In the case of multi-material systems, utilizing materials with different properties can enhance the final functionalities of the printed parts.

3.4.1. MJ materials and process parameters. In the MJ process, as in the previous UV-assisted 3D printing process, the UV light intensity and exposure time are the primary parameters that determine the final mechanical performance of the printed part. Typically, a UV lamp requires calibration to prevent problems related to its intensity. To improve the mechanical properties, a common practice is to combine MJ with post-treatment processes. Dynamic mechanical analysis (DMA), Nanoindentation, and Fourier-transform near-infrared spectroscopy (FTIR) are useful investigation techniques for examining changes in viscoelastic properties, such as storage modulus and relaxation modulus, glass transition temperature, and changes in hardness, all of which are attributed to the increasing level of photopolymerization.[424–426] Contrary to the SLA or UV-DIW process, in which the UV light is selectively pointed on the zone to be cured, in the MJ process, since the UV lamp is laterally attached to the jetting head and is always on, it

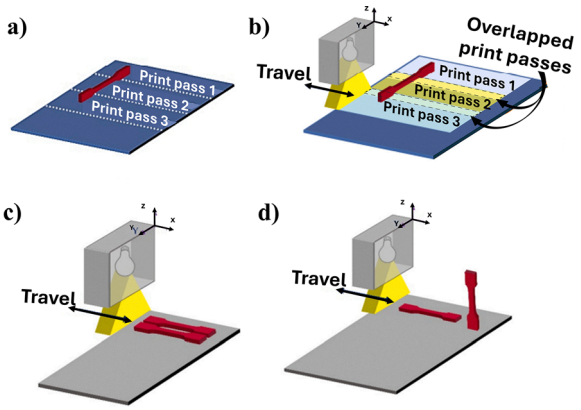

Fig. 21 The importance of building orientation and part spacing to avoid over-curing in the MJ process: (a) scheme of print bands according to the length of the jetting head; (b) representation of overlapping scan regions; (c) over-curing due to strict part spacing; (d) over-curing due to different heights of samples positioned in the same print band. Adapted with permission from ref. 425. Copyright 2023 Elsevier.

moves simultaneously and indiscriminately irradiates across the build plate to induce polymerization of deposited resins. This allows the parts to be exposed to variable UV levels, inconsistent curing, or localized over-cured zones.[427] The relevance of properly combining building orientation with part spacing, considering the width of UV exposure, is schematized in Fig. 21a–c.[425]

Another parameter peculiar to the MJ process and not common to other UV-assisted 3D printing technologies is the type of finishing. Surface finish is important because it can reduce post-processing costs, enhance component functionality, and affect part accuracy. It may be of two different types: glossy surface finish setting or matte finishing. In the case of a glossy finish, the support material is deposited only at the base of the component as an interface layer between the platform and the piece to be printed, and in all those areas where the collapse of the product has to be avoided, such as protrusions or voids. On the other hand, in the case of a matte finish, the support material is deposited on the entire surface of the piece, even on lateral or flat faces. It follows that a complicated structure could not be printed entirely with glossy finishing because features with a negative angle (smaller than 90°) or overhangs always require a support material, which results in matte finishing zones.

When a glossy aspect is desired for a complex geometry, a post-processing process can be used to remove the matte layer. Otherwise, it is suggested to divide the CAD model into different pieces that do not require support materials and assemble them at the end of the process.

Finishing mode has multiple effects, not only from an aesthetic point of view, but also regarding functional and mechanical properties. An overview of the effect of these process parameters on the final properties of the MJ-printed material was reported by N. Muthuram *et al.*,[418] while O. Gülcan *et al.*[428] and H. Kim *et al.*[429] critically reviewed how to control the dimension accuracy and printing errors in MJ. The main aspects emerging from these studies are listed in Table 12.

Employing different materials can lead to enhanced thermal and mechanical properties, provide additional properties (*e.g.*, electrical conductivity, barrier properties), or simply separate two attached materials, such as insulators and conductors, when fabricated in a continuous process.[416,430] However, when it comes to the overall functionality of multifunctional structures and composites made using multi-material additive manufacturing, the interface qualities are crucial.

Liu *et al.*[436] developed a material mixing model based on the distribution of material properties, which was able to successfully predict the effective stiffness and effective strength calculated from experiments. The authors found that interfaces between rigid and compliant materials printed *via* MJ were strong enough due to the material mixing during the process. Combining two or more photopolymers in determinate concentrations and microstructures results in digital materials, a composite material with hybrid properties.[437]

In addition to digital materials, other materials already present in the market and usually applied in the MJ process are summarized in Table 13, together with their respective properties. N. Muthuram *et al.*[418] in their study reviewed

Table 12 MJ process parameters and their effect on the final printed object

Parameters	Effect	Ref.
UV light intensity	• Over-curing • Over-aging • Mechanical performance (brittleness)	431
Jetting head length Building orientation Part spacing	• Inhomogeneity in curing degree • Over-exposed regions • Dimension stability (part distortion)	417, 425 and 432
Glossy finishing type	• Accumulation of exceeding resin between neighboring components • Surface roughness	106, 416 and 433–435
Matte finishing type	• Process duration (time-consuming) • Surface roughness	434 and 435
Printing mode (high quality or high speed)	• Mechanical properties (tensile strength, flexural modulus, and shore hardness) • Costs • Process duration • Material consumption	416

different case studies in which these materials have been used for different applications, such as a microfluidic capacitor and a turbine blade.

To maximize MJ printed part stiffness, Sugavaneswaran *et al.*[442] used a high-strength "ABS-like" material as reinforcement of a flexible "polypropylene-like" matrix. The results showed that the use of a rigid material as reinforcement in a flexible matrix enhanced the elastic modulus by 6.79% to 21.03% with respect to the reinforcement orientation. There are a few examples of fiber-reinforced MJ printed objects in the literature. The benchmarked carbon fiber composite made by conventional mold casting has a substantially higher total strength than the MJ-constructed structure. This drawback occurs because, due to the presence of significant voids, the interfacial strength between the reinforcement and matrix of an MJ-intended composite structure is compromised.[439] Among the smart properties interesting for the aerospace and aeronautical sectors, few examples have been found in the literature. Gang Chen *et al.*[443] developed a flexible strain sensor with dual conductive networks, consisting of a polyvinyl alcohol/multi-walled carbon nanotube (PVA/MWCNT) substrate layer and an overlying poly(3,4-ethylenedioxythiophene) polystyrene sulfonate/MWCNT (PEDOT:PSS/MWCNT) layer patterned and deposited layer by layer. A wide strain response range of 0.6–80% and high sensitivity with a gauge factor (GF) of 31.2 was obtained. Additionally, the strain sensor stabilized its current signal under 2000 cyclic loading conditions, demonstrating good stability and versatility for UAV flight monitoring, including real-time strain detection during take-off and landing processes. No peculiar examples have been found for piezoelectric and self-healing functions, while a review paper on shape memory MJ printed materials emerges.[444] According to this study, commercially available polymer inks offer limited opportunities for tailoring their thermomechanical properties. Similarly, most inkjet printers are not designed to accommodate customized or modified inks. These limitations highlight the need for comprehensive theoretical and experimental research to assess the viability of newly formulated SMP inks for inkjet applications. Although dedicated research systems exist for testing novel inks, they currently lack the capability to produce complete, functional 3D structures.

3.4.2. MJ printed parts in the aerospace and aeronautical sectors. The MJ process is a versatile technique that has captured the attention of the aerospace industry due to its capability to fabricate multi-material, functional composites and structures. High-performance thermoplastics, along with rigid and thermally resistant resins, are utilized to produce jigs, clamps, check gauges, and finished aircraft components in a cost-effective, time-efficient, and flexible manner.[439] The UAV sector is undoubtedly the main field of MJ printed structures. Moon *et al.*[445] exploited the capability of MJ technology to print complex structures, thereby lowering the weight of a UAV wing while simultaneously guaranteeing optimal elastic performance. Three lattice designs – the 3D Kagome structure, the 3D pyramidal structure, and the hexagonal diamond structure were selected as the interior design of the wings, as reported in Fig. 22a. The results obtained by the authors demonstrated that the 3D Kagome has the highest load capacity. However, the

Table 13 Properties of common commercial MJ materials

MJ materials	Properties	Ref.
Digital ABS	Heat resistant High impact resistance Good finishing quality	418
Tango Tango+ Tango black+ Tango grey	Rubber-link material with large elongation	438
Vero white+	Rigid material able to simulate the properties of ABS	439
Vero clear	Transparent materials to simulate PMMA mechanical and optical characteristics	439
Vero transparent Vero pure white Vero magenta Vero cyan	Rigid and opaque material. Stiffness and high-quality, accurate details.	440
DM40 DM50 DM60 DM70 DM85 DM95	Mixture of Tango Black + and Vero White + two base materials. The naming convention is based on the equivalent Shore A hardness of each material. For example, DM60 stands for a Digital Material with Shore A hardness of 60.	441
Agilus 30	Combination of elastomers and thermoplastic substances. Soft and flexible (shore A hardness is 30). Excellent dimension stability Resistance to wear and tear.	418
Stratasys RGD series	RGD 720: Rigid translucent material used for simulating standard clear plastics in prototypes and concept models RGD 525: High-temperature (75–80 °C) opaque material RGD 450: PP-grade material known for its strength and chemical resistance	439

hexagonal diamond exhibited the ideal properties of an energy absorber. Complex 3D printing structures can be utilized as cores in sandwich structures, and also for mitigating noise and vibration problems, and protecting electronic equipment carried by satellites from any deformation, as shown in Fig. 22b.[446,447] Rajendra Boopathy *et al.*[430] not only exploited the free-form advantage of 3D printing but also took advantage of the MJ process to simultaneously print different materials in the same object in a continuous process. The authors studied the impact and compression response of multi-material honeycomb structures particularly important in in-flight scenarios. Three-layered honeycomb structures were printed *via* MJ using two completely different commercial materials: Vero White (rigid material) as reinforcement and Tengo Plus (soft material) as the matrix. The two-layer (2L) structure contains one layer for each material, and three-layer (3L) structures consist of a central structure of Tengo Plus and two external layers of Vero White. Finally, a five-layer (5L) structure is composed of three layers of Tengo Plus alternated with two layers of Vero White. While the rigid material alone proved to be completely unable to absorb impact loads, this capability gradually improved with an increase in the number of material layers. Moreover, MJ printing can be used to produce a reliable mold for complex structures, thereby reducing the cost of tools required in conventional processes, such as injection molding and thermoforming. This is because, apart from the price of the machine, MJ required lower labor costs and reduced time. In addition, 3D printing flexible design allows for the integration of cooling channels into the molding tool, taking into consideration the complexity of the geometry and the number of cavities. Fig. 22c illustrates an example of an MJ-printed molding tool and the corresponding thermoformed interior part developed by the American Institute of Aeronautics and Astronautics for use in electronic vehicles.[448]

Despite the unique advantage of using different materials in a single-step process, MJ has not yet gone beyond the use of commercial materials. This limitation reduces the possibility of extending this technology to the production of functional components, such as sensors, or to localize smart functions with proper control. Improvements in materials compatibility and further studies on smart polymers are topics still to be addressed.

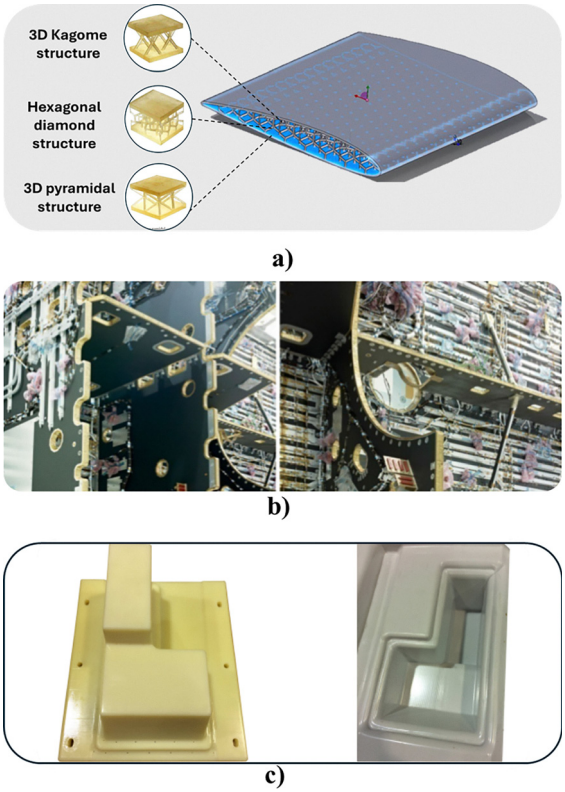

Fig. 22 Examples of MJ applications in the aerospace and aeronautical sectors: (a) MJ printed complex structures for light-weight high-strength reinforcement. Adapted with permission from ref. 445. Copyright 2015 Springer Nature; (b) coupling structure–structure in the design of the satellite;[446] (c) MJ printed mold and thermoformed interior parts for electric vehicles. Reproduced with permission from ref. 448. Copyright 2015 IAA (American Institute of Aeronautics and Astronautics).

3.5. Selective laser sintering (SLS)

The SLS process follows the main principle of AM technology by fabricating complex structures layer by layer. However, the principal difference with respect to the other described 3D printing technologies lies in the fact that SLS works on polymers in the form of a powder. The SLS machine uses a CO_2 laser beam to selectively solidify the powder according to the CAD model. Commonly, the SLS machine is composed of three chambers, two for the unsolidified power and the building chamber (where the sample is produced) between them, as schematized in Fig. 23. Even the process can be divided into three phases. In the first step (powder recoating) a recoating roller delivers a thin layer of powder on the building plate of the central chamber.

Then, in the second phase (laser energy input or "powder melting"), the laser beam scans and solidifies material particles (the consolidation could take 35 s or 40 s depending on the machine), and finally, once the layer is completed, the piston of the building chamber moves down by a height equal to the layer thickness (from 20 to 150 μm), while the piston in the

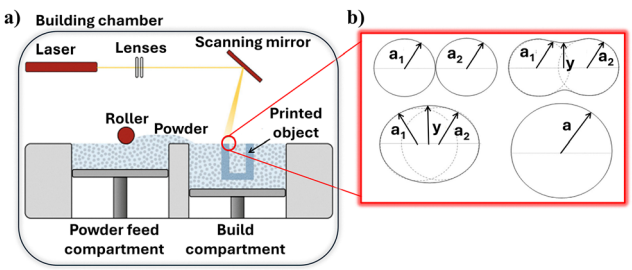

Fig. 23 (a) Schematic representation of the SLS machine. Reproduced with permission from ref. 451. Copyright 2021 Springer Nature, (b) scheme of sintering of polymeric particles according to Frenkel–Eshelby viscous. Reproduced with permission from ref. 199. Copyright 2014 Elsevier.

powder chambers moves up to make a new quantity of powder available for the deposition.[449,450]

Throughout the entire process, the temperature of all the chambers is set and controlled to specified values. The building chamber is warmed to a temperature value, known as the powder bed temperature (T_b), which is lower than the softening temperature points of the polymeric material to prevent particle sticking;[449] thus, it mainly depends on the material type (amorphous or crystalline). T_b is maintained at a constant level until the end of the process, when the room conditions are restabilized, cooling down the final object and allowing its consolidation without applying pressure. Usually, the isothermal condition in the building chamber is reached thanks to the energy provided by continuous IR lamp irradiation and/or resistance heaters.[450]

Unlike many other AM techniques, SLS does not require support structures to prevent the created part from collapsing, which is one of its main advantages, as the unmelted powder serves as a natural supporter.

As can be easily understood, a large quantity (approximately 70%) of the powder remained unsolidified, and due to its high cost, it is usually recycled. In cases where the powder needs to be reused for the same process, to ensure reproducibility and the success of the process, it is necessary to restore the particle characteristics, such as shape and dimensions, which strongly affect their flowability.[449] Moreover, particle aging prevalently depends on the building temperature and the duration of the process. Typically, exposure to light radiation and humidity, combined with the temperature effect, contributes to the degradation of the powder in terms of thermal stress, unstable crystallization state, residual stress, and chain scission.[452] The most commonly used practice to reuse unsolidified powder, while saving costs, is to partially substitute the total quantity of unsolidified powder with approximately 50% virgin powder.[453] Moreover, Gomes *et al.*[454] proposed a post-processing method to reuse polymeric powder without requiring additional amounts of virgin material. The author noticed that at the end of each printing cycle, the degradation of the unsolidified powder was apparent, both from thermal and morphological points of view, resulting in high porosity and roughness of the printed part. To limit the degradation, the proposed post-processing method consisted of milling, filtering, and homogenizing the powder at each cycle. Finally, a less expensive strategy is to reuse the unsolidified material for other 3D printing processes (*e.g.*, FFF), where thermoplastic particles are completely reshaped into filament form.[455] For example, Mohammad Uddin *et al.* recycled the waste SLS nylon powders into a new FFF filament. The waste filament exhibited reduced moisture absorption and comparable mechanical properties to commercially available nylon filament. Moreover, the waste SLS powder was also reinforced with Mg powders to improve the mechanical properties of the filaments further. Incorporating 8% Mg into the waste composite boosted the flexural strength by as much as five times with respect to the waste nylon alone.[456] In another study, PA12 waste was recycled by mixing it with PVA and adding 1 wt% and 3 wt% of nanosilica.[457] Wang *et al.*[455] demonstrated the feasibility of using a milled carbon fiber (mCF)/recycled polyamide12 (rPA12) composite filament for FFF. Tensile strength, tensile modulus, flexural strength, flexural modulus, and impact strength of rPA12 filled with 30 wt% mCF were improved by 35%, 163%, 61%, 138% and 23%, respectively. As a comparison, a fuel-line quick connector was also printed using a commercial ABS filament. The quality of the parts produced using the recycled composite filament was comparable to that of a commercial filament after switching from a 0.5-mm nozzle to 0.8 mm to avoid clogging.[455] As can be noticed, nanofillers are mainly used to adjust the properties or performance of waste pristine polymers after their use in the SLS process. However, the recyclability of SLS-waste nanocomposite powders is a relevant topic for the aerospace and aeronautical sectors, and even in general, which has not been addressed yet and is worth investigating in future research.

To fully understand how the sintering phenomenon occurs and enables the solidification of the powder, it is necessary to consider four categories of SLS technologies based on the binding mechanism.[449,458] Solid State Sintering (SSS) is a binder mechanism dominated by diffusion phenomena. It happens at a temperature lower than the melting point (between $T_{Melt}/2$ and T_{Melt}) when a flux of atoms between two adjacent particles moves towards the neck regions due to a gradient of vacancy concentrations in those regions. Although this phenomenon occurs not only for polymeric particles but also for any material, it is quite slow and requires a pre-heating of the powder. Chemical-induced binding (CIB) is a sintering process aided by a chemical reaction. The presence of a gas capable of reacting with the powder in the building chamber favors the formation of chemical species that act as binders between the particles. CIB is mainly used for metals. Liquid phase sintering (LPS) is referred to in this manner because part of the powder melts, allowing the unmelted particles to adhere to one another. In the LPS process, two different materials can be used, such as a low-temperature binder and a structural material, or a single material with two main sizes, where the smallest particles melt faster to bind the larger ones. Finally, the last category is represented by fully molting sintering, better known by the name of selective laser melting (SLM). In this case, the high energy of the laser source completely melts the particles, resulting in almost fully dense products with mechanical properties comparable to those of bulk objects. However, this technology is mainly used for metals.[458] Although this theoretical distinction exists, when polymeric particles solidify together, a series of practical phenomena make it very difficult to categorize the process perfectly.

3.5.1. SLS process parameters and material properties. The binding phenomenon is governed by the Frenkel-Eshelby model:[199]

$$\frac{y}{a} = \left(\frac{\Gamma t}{\mu a}\right)^{0.5}$$

where y is the half-neck radius, a is the initial particle radius, Γ is surface energy, μ is viscosity, and t is sintering time. This

model illustrates the time dependency of the neck radius (as depicted in Fig. 23b), where the radius of particle a is assumed to be constant throughout sintering. This means that the model is only valid in the early stage. However, this model is a good indication of how the properties of the polymeric materials affect this phenomenon. More specifically, viscosity plays a crucial role, as it can vary by several orders of magnitude when nanoparticles are added or the molecular weight of the polymer is altered. This is the reason why a rheological characterization of polymeric powder at a low deformation rate and in the same temperature conditions is needed.[199]

The type of polymeric material, whether amorphous or semi-crystalline, affects both the sintering phenomenon and the solidification efficiency. Regarding the sintering phase, the viscous properties can be significantly different between amorphous and semi-crystalline materials. Once the amount of heat necessary to destroy the ordered crystalline region has been absorbed, the melted liquid flows in the neck regions with a lower viscosity than amorphous polymers, since the semi-crystalline ones have a high constitutional and conformational order along their polymeric chains. This aspect makes the SLS process of semicrystalline materials faster. On the other hand, the disordered structure of the amorphous polymer implies a higher viscosity than semi-crystalline, even when the same temperature (above T_g) is considered. It follows that the SLS of amorphous polymers faces issues such as low flowability, higher porosity, consequently lower compactness degree, and less strength in the final product. On the other hand, semi-crystalline polymers suffer the problem of shrinkage and residual stress after cooling down.[449]

However, rheological properties represent just one of the key intrinsic characteristics of the material required for the SLS process. The selection of materials for the SLS process is based on both intrinsic and extrinsic properties,[459] as schematized in Fig. 22. Since extrinsic properties do not depend on the material itself, but rather on how it was manufactured into particles, these aspects will be discussed later as process parameters. Optical and thermal properties are the other intrinsic characteristics that need to be addressed. Optical properties affect the material's ability to absorb energy at the wavelength of the laser source (usually a CO_2 Laser, with a wavelength of 0.6 μm).[460] The majority of polymers containing aliphatic segments (C–H) easily absorb energy, while other polymers have some groups of vibration in the 'fingerprint' infrared (IR) region sufficient to absorb relevant portions of 10.6 μm radiation.[459,460] In any case, the absorption capability could be compensated by increasing the laser power, making the optical aspect of the material less critical. Regarding thermal properties, DSC analysis is fundamental to determine the nature of the material, whether it is amorphous or semi-crystalline, before setting the process parameters.

The operative temperature in the building chamber strongly depends on the melting and crystallization temperatures for semi-crystalline polymers and the glass transition temperature for amorphous polymers. The 'sintering window' is a metastable thermodynamic region of undercooled polymer melt[459] positioned between the melting and the crystallization temperature. In this temperature interval, the sintering of semi-crystalline polymers occurs in quasi-isothermal conditions.[373,460] For semi-crystalline polymers, it is essential to have a ''sintering window'' wide enough not to cause defects in the final sample. In fact, in the case where the temperature during the sintering process is too close to the crystallization point, crystals start to form prematurely, and the final object will show warpage defects. On the other hand, a sintering temperature near the melting point results in a loss of finishing quality, as neighboring particles tend to adhere to the surface of the sintered part. For amorphous polymers, to ensure the correct flowability in the neck region between particles, a temperature just above T_g (with a maximum of 50 °C higher) is recommended, although their change in viscosity is lower than that of semi-crystalline polymers.[460] In the case of a blend of semi-crystalline polymers, the sintering window is delimited between the melting temperature of the low-melting polymer and the crystallization onset temperature of the high-melting polymer.[461]

The sintering temperature is not constant along the process and the DSC conditions (*e.g.* scan rate of 10 °C min^{-1}) are not the same as a real process, for these reasons many papers in the literature tried to model the SLS process by considering sintering, heat transfer phenomena and material properties.[462–465] All three main classes of polymeric materials (thermoplastics, thermosets, and elastomers) can be applied in the SLS process. Regarding thermoplastics, PA11 and PA12 are widely employed and already commercially available in the form of a powder for SLS printing, as they are stable during the process, exhibit minimal shrinkage due to their large sintering temperature window, and possess good mechanical properties.[459,466–468] Together with PA, PC,[469,470] PET,[471–473] and PEEK[474–478] are the engineered materials and high-temperature materials suitable for the SLS process. Even standard polymers, such as PE,[479–482] PP,[483–485] PS,[486–488] PMMA,[472,489] and ABS,[490,491] are used. Regarding elastomeric materials, the SLS process is primarily used to print thermoplastic polyurethane (TPU), a semi-crystalline polymer characterized by good tensile strength, abrasion resistance, hydrolytic stability, flexibility, durability, and corrosion resistance.[492–496] Moreover, the good flowability of its powder, low melt viscosities, and minimal shrinkage during the consolidation phase are the key aspects that make TPU a suitable material for the SLS process.[493] Lv *et al.*[497] tried for the first time to print *via* SLS polyetherimide (PEI) material to alleviate the supply-chain issues in the aircraft maintenance industry. At the same time, blends and nanocomposite materials have been investigated. For the SLS process, blends of polymers are generally multiphase systems; thus, the microstructure of the final object strongly affects its mechanical properties.[459,498,499] In brief, when two different polymers are mixed in powder form, the material with better optical properties and a lower melting temperature acts as a binder between the particles of the other material.[500,501] For other energy-assisted AM technologies, such as SLA or UV-DIW and Laser-DIW, it is complicated to add nanoparticles without

Table 14 Examples of nanocomposite materials printed *via* SLS

Composition	Properties	Ref.
PA12-carbon nanotubes	Enhanced thermal conductivity (from 0.21 W K^{-1} m^{-1} to 0.40 W K^{-1} m^{-1} as the s-CNTs addition increases from 0 to 0.5 wt%) and electrical properties (over 10^{-5} S cm^{-1})	499
PEEK-graphite	The addition of graphite improved laser absorption, lowered the flowability of powder and increased porosity and maximum pore size	509
Siloxane-containing phenylethynyl-terminated polyimide oligomer powders with milled carbon fibers	High tensile and compression performance; high heat resistance and reliable tribological property. Printed composite with 30% of CF showed tensile strength of 82 MPa, tensile modulus of 4.4 GPa, elongation at break of 2.3%, and T_g of 419 °C, comparable performance to those of thermal compression molded composites	510
Commercial RTM370 imide resin modified with reactive phenyl ethynyl (PEPA) groups- carbon fibers	Attempts to print high-temperature thermoset polyimides. Postcure on the LS-printed resin chips was unsuccessful because of the melting of the oligomer resin instead of crosslinking. Improved high-temperature resistance (T_g above 300 °C). The development of laser-curable reactive endcaps would be a viable solution to advance the laser sintering of thermoset resins	511 and 512
Bismaleimide (BMI I-841) – carbon micro-balloons (CMB)	Enhanced mechanical properties: damping factor (tanδ) peak is observed at 297.7 °C, 114.9 MPa stress is reached before fracture in compression mode.	513
TPU – carbon nanotubes	Self-sensing properties in compression mode: TPU/CNT composites with 0.25 wt% CNT exhibited a high sensitivity (0.12–0.549 kPa^{-1}) in a wide range of pressure values (17–240 kPa).	496
Thermoplastic polyether-*block*-amide (TPAE) - carbon nanotubes	Self-sensing properties and electro-induced shape memory from Joule heat generated by electrothermal conversion effect.	514
PA11 - glass beads	The tensile and compressive modulus increases while strain at break and strain at yield decrease as a function of glass bead volume fraction.	515
PA-12 - single-walled carbon nanotubes	For a sample with 2 wt% SWCNTs, electrical conductivity reached a plateau value of 3.2×10^{-2} S cm^{-1}. The electrical conductivity of the printed sample is within the same order of magnitude as that of the pressed sample. For the pressed composite, a higher anisotropy coefficient of 4.8 is observed than for the printed one	516
PA11-$BaTiO_3$	For the composites containing 40 wt% $BaTiO_3$ particles, the sintering window increased from 10.1 °C to 14.6 °C. Sintered PA11–80%$BaTiO_3$ nanocomposites show enhanced d_{33} (4.7 pC N^{-1}) and g_{33} (27.6×10^{-3} Vm N^{-1}) values, about 47 and 8 times, respectively, higher than pure PA11.	517
PA1212-glass fiber (GF) and glass beads (GB)	10 wt% GFs and 40 wt% GBs significantly strengthened the PA1212 matrix. The 40GB-10GF specimens exhibited a good combination of shore hardness and tensile strength of 83.8 HD and 52 MPa, respectively, at a laser power of 30 W.	518
PVDF–graphene	Comparison of the piezoelectric performance of hollow arrays (BCP), spherical hollow arrays (BSP), and ellipsoid hollow arrays (BEP) structures. BSP was optimal (at the acceleration of the linear motor of 7 m s^{-2}, the open circuit voltage and short circuit current were 16.97 V and 274.0 nA, respectively, followed by BCP and finally by BEP).	519
TPU aluminum (AlN) and boron nitride(h-BN)	At 20 wt% of AlN and 15 wt% of h-BN, the thermal conductivity of the TPU composite is 0.90 W mK^{-1}, 391% higher than that of pure TPU sintered parts	520
TPU-carbon nanotubes and graphene	1% wt of MWCNTs and graphene (70/30 wt/wt) filled TPU printed in diamond and gyroid unit cells showed negative piezoresistive behavior with a gauge factor of about −13 at 8% strain. Porous structures (20% of porosity) exhibited microwave absorption coefficients ranging from 0.70 to 0.91 in the 12–18 GHz region and close to 1 at THz frequencies (300 GHz–1 THz)	521

reducing the penetration depth. In contrast, numerous manuscripts are present in the literature for nanocomposites processed *via* SLS.[498,502,503] However, nanoparticles can also be used to modify the optical properties of the powder. It was demonstrated that the addition of graphite improves the energy absorption, allowing the temperature of the powder bed to be lower.[504] On the other hand, because radiation is mainly absorbed by fillers (*e.g.*, graphite, carbon black, or carbon fibers) at the surface of the polymeric particles, the laser energy does not propagate throughout the powder bed, thereby reducing the melting efficiency.[505] Some examples of SLS-printed nanocomposites are reported in Table 14. Azam M. U. *et al.*[506] reviewed several case studies of self-sensing and strain-sensing composite polymers printed *via* the SLS process. From their study, it emerges that SLS has proven highly effective in producing electrically conductive polymer composites with advanced functional capabilities. This effectiveness is largely attributed to the development of segregated filler networks within the sintered structures, where conductive fillers tend to concentrate along the boundaries of the polymer powder particles. These segregated configurations create efficient conductive pathways, significantly enhancing electrical performance. The overall conductivity of the composite is influenced by several parameters, including filler content, spatial distribution, orientation, and the degree of interconnection.[506] In a more recent study, the same authors (M. U. Azam *et al.*) investigated the effect of different values of relative density (20%, 30%, and 40%) on the self-sensing hexagonal

honeycomb structures (HHSs) fabricated using SLS of a ball-milled nanocomposite powder containing 0.3 wt% multi-walled carbon nanotubes (MWCNTs) blended with polyamide 12 (PA12).[507] The unfilled PA12 HHSs displayed lower porosity and superior mechanical characteristics—such as higher collapse strength, elastic modulus, and energy absorption—particularly at higher densities (30% and 40%). Under out-of-plane compression at 40% relative density, the specific energy absorption of neat PA12 reached 24 J g^{-1}. In contrast, the addition of MWCNTs led to a decrease in mechanical strength and stiffness, but significantly improved energy absorption efficiency, reaching up to 53%. Furthermore, the MWCNT-reinforced structures demonstrated high sensitivity to strain within the elastic range, with gauge factors as high as 25. Achieving optimal performance involves balancing electrical conductivity with mechanical integrity, as higher filler concentrations often compromise mechanical strength. To address this, post-processing methods—such as annealing, isostatic pressing, or surface modification—are commonly used to reinforce filler connectivity and improve the composite's structural cohesion.[506] Nonetheless, several challenges remain, such as enhancing the stability and structural design of polymer composites, differentiating multiple stimuli (*e.g.*, temperature *versus* strain) from a single signal output, and innovating multifunctional, self-responsive materials, including those with magnetic, optical, or self-healing properties.[506] A peculiar case is that published by Li X. and coworkers,[508] in which conductive nanofiller has been added to the CAN matrix to obtain a multifunctional material. They developed self-healing and conductive elastomer composites by wrapping single-walled carbon nanotubes (SWCNTs) onto poly(dimethylsiloxane) covalent adaptable networks (PDMS-CANs) using a liquid-phase deposition and adsorption process. These SWCNTs@PDMS-CANs composite powders were then employed in SLS printing to fabricate lattice-structured parts. During printing, conductive segregated SWCNT networks formed in situ, yielding an ultra-low electrical percolation threshold of 0.007 wt%. The resulting structures exhibited multifunctionality, including crack diagnosis and self-healing capabilities triggered by heat, light, or electricity—enabled by the photothermal and electrothermal properties of SWCNTs. Shape memory function has not been studied yet in SLS, since no documented research has been found. This suggests that the integration of shape memory polymers into the full spectrum of 3D printing technologies is still in its early stage.

SLS process parameters can be divided mainly into three categories: laser parameters, building parameters, and material parameters. The effects of the parameters belonging to these three categories are summarized in Table 14. Laser power, scan speed, scan spacing, and laser beam diameter belong to the first group. Laser power can be set as a percentage value of the maximum power allowed by the machine. Scan speed represents the velocity at which the laser scans the powder surface, thereby determining the exposure time of the powder to the energy source. The concept of scan spacing is similar to hatching spacing, introduced for the SLA process, which refers to the distance between two neighboring parallel scans. Laser power, combined with scan speed and scan spacing, determines the amount of energy sent to the powder surface. This energy can be estimated as surface energy density (J mm^{-2}):[449]

$$\text{Surface energy density} = \frac{\text{laser power}}{\text{scan speed} \times \text{scan spacing}}$$

or taking into consideration the layer thickness as volume energy density (J mm^{-3}):

$$\text{Volume energy density} = \frac{\text{laser power}}{\text{scan speed} \times \text{scan spacing} \times \text{layer thickness}}$$

Scan spacing (s) and laser beam diameter (D_b) are correlated by the following equation:[451]

$$\text{OL} = \frac{D_b}{s}$$

where OL is defined as the overlay ratio, and the laser beam diameter is always larger than the scan spacing, resulting in overlay regions between two adjacent scans.[451] The most relevant building parameters are layer thickness, the temperature of the powder compartment, and the temperature of the building compartment (see Fig. 24 and Table 15).

Yehia H. M. *et al.*[522] studied the exploitation of machine learning (ML) techniques—supervised, unsupervised, and reinforcement learning—in optimizing processes, detecting defects, and ensuring quality control within SLS. However, the authors underlined that challenges associated with integrating ML in SLS, including data availability, model interpretability, and leveraging domain knowledge still remain; they could be studied in future research. The intrinsic material properties introduced above play a key role in determining building and laser parameters. Moreover, the extrinsic properties of the polymer powder must not be underestimated. The final density of the product is strongly affected by the spreadability of the powder when the roller deposits a new layer. It follows that the shape, morphology, and size of the powder are crucial aspects. Even the geometry of the roller can affect the distribution of the powder, which must be uniform, since no additional pressure is applied during the process to compact the powder.

Typically, the powder dispenser can be a roller or a blade; however, it appears that the roller provides a more uniform distribution of the powder layer due to its larger contact area between the dispenser and the particles.[450] In the end, it is necessary to emphasize that when filler materials, such as fibers, graphene nanoplatelets, or carbon nanotubes, are added to composite materials, the powder flow behavior changes completely and needs to be characterized before the process begins.[499,529,530]

3.5.2. SLS printed parts in the aerospace and aeronautical sectors. GKN Aerospace, a global multi-technology leader in the aerospace industry, in collaboration with Materialise, one of the biggest companies in the field of 3D printing, designed and

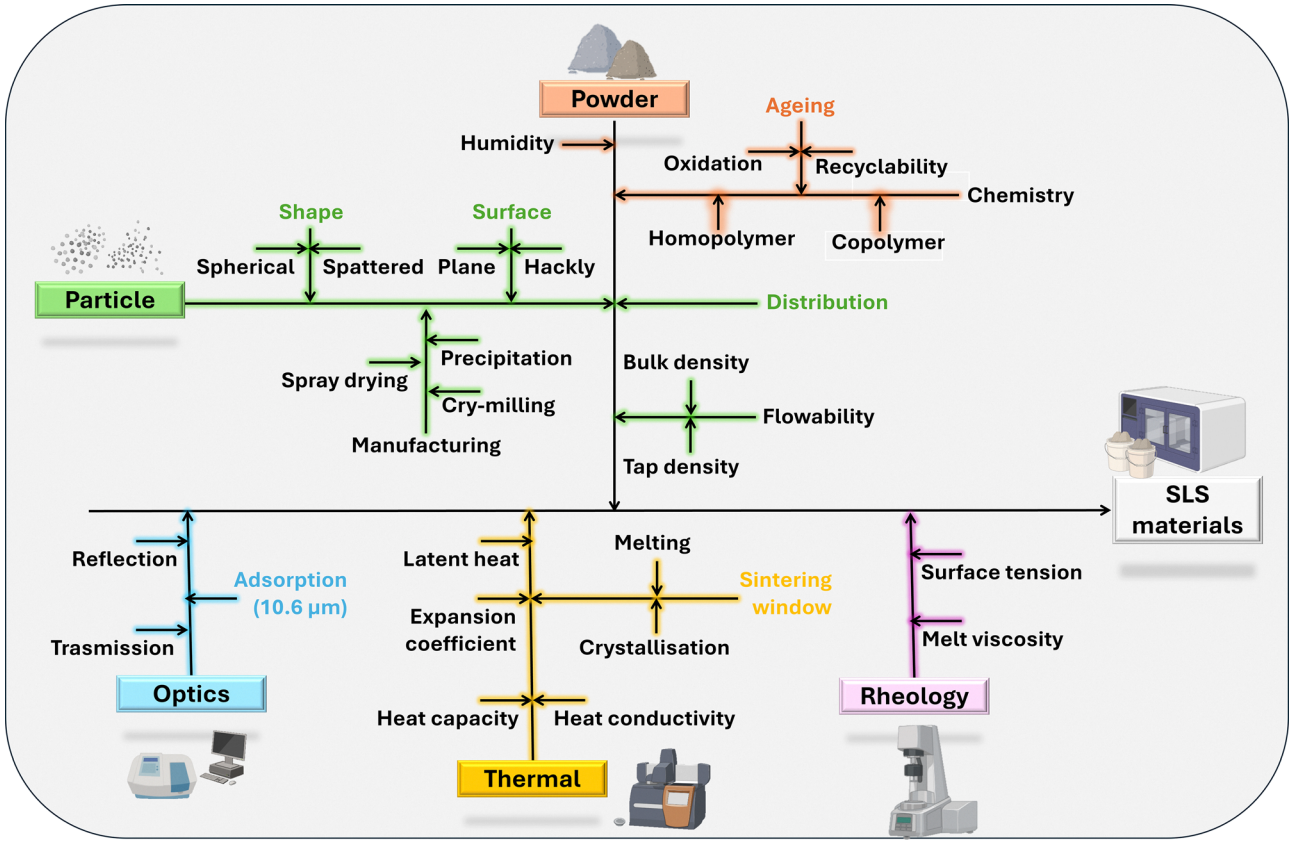

Fig. 24 Intrinsic and extrinsic properties for material selection in the SLS process. Adapted with permission from ref. 459. Copyright 2015 AIP Publishing.

produced the largest fully electric airplane ever flown, Aviation Alice V2. In Fig. 25a, the Alice V2 winglet is reported to highlight its complex geometry and navigation light interface. The necessity to produce this complex structure in a short time and the requirement for a lightweight product drove companies to invest in SLS technology and print it in PA12. Alice V2 is a valid example of the efficiency of the SLS process in producing parts suitable for aeronautical applications. Moreover, this technology offers the possibility to quickly and cost-effectively replace damaged winglets for maintenance purposes.[531]

The integration and rapid development department of The Boeing Company in Mesa stated that SLS technologies enable the reduction of the production cycle time, minimize potential human error, and facilitate digital manufacturing of small quantities. The SLS process minimizes tedious processes, including generating part drawings, creating prototype tooling, producing prototype parts, and performing post-secondary fabrication steps. At the same time, this technology presents a valuable opportunity to produce customized parts in a short timeframe, thereby reducing the cost related to small quantities of production. Most of the SLS-printed pieces by Boeing (*e.g.*, actual parts, functional parts, rapid prototyping, rapid tool development, and rapid manufacturing) are made of commercial DuraForm Polyamide (PA) material and go directly on prototype aircraft, vehicles, and mock-ups.[532] Not only the process but also the development of materials has attracted the attention of Boeing, which in 2010 patented a flame-retardant material for the SLS process composed of polyamide and a brominated hydrocarbon.[533] Solid Concepts, an additive manufacturing service provider, realized a fixed-wing UAV called PTERA *via* SLS printing of powdered nylon. Not only the structure, but also the fuel tank, which is usually built out of steel or other metals, was fabricated *via* SLS and coated inside with a special sealant, resulting in drastically reduced production time and total weight of the tank.[534,535] The image of the real product is reported in Fig. 25b. Similar to the FFF process, SLS allows for the production of interior parts, even using engineered plastics, such as PA. Real components made of composite or nanocomposite polymers are still missing at an industrial scale; however, SLS is suitable for obtaining high-performance strain sensors (both piezoresistive and piezoelectric) that could be a promising application in the near future. Moreover, the peculiar distribution of nanoparticles (*e.g.*, MWCNT) in the material structure allows for tailoring smart functions on the basis of printing parameters. Few works are present in the literature on the recyclability of SLS powder in the same process. New methods to recover high-expense raw powder represent a field to explore.

4. Discussion

3D printing technologies have significantly advanced the aerospace and aeronautical sectors, offering innovative solutions for manufacturing complex components with reduced weight

Table 15 Effect of SLS process parameters on the final printed object

Laser parameters		
Parameters	Effect	Ref.
Energy density	• Improved mechanical properties • Material degradation • Part density • Warpage • Balling defects and cracks (if high energy density is combined with high scan speed) • Surface roughness • Delamination (if energy density is low)	449 and 523–526
Overlay ratio (OL)	• Material consistency and porosity • Mechanical performance • Process duration	527
Building parameters		
Layer thickness	• Process duration • Surface quality	449
Powder compartment temperature (lower than T_g)	• Particles agglomeration • Spreadability of particles	459
Building chamber temperature (within the sintering window)	• Energy needed for melting • Premature crystallization and warpage defect (if then T_c) • Low compactness and surface quality (if lower than T_m) • Cooling rate	459 and 528
Material extrinsic properties		
Particle shape (sphericity) Particle dimension (diameter of 20–80 μm)	• Flowability • Part density • Cost of raw materials • Finishing quality	449 and 459

a) b)

Fig. 25 Examples of SLS applications in the aerospace and aeronautical sectors: (a) Alice V2 winglet;[531] (b) UAV-PTERA images.[534]

and enhanced functionality. Among these, fused filament fabrication (FFF) stands out as the most mature and widely adopted technology, primarily due to its ability to process a broad spectrum of materials with relative simplicity and cost-effectiveness. Its industrial scalability is well established, with manufacturers like Stratasys providing a diverse range of FFF printers suitable for large-scale aerospace applications, including the production of composites and tooling.[536] The process's capacity to incorporate long fibers as reinforcement within the polymer matrix without requiring sophisticated equipment is a notable advantage, leading to stronger, more durable parts. Additionally, FFF's higher printing speeds compared to other technologies translate into shorter production cycles and increased productivity, which are critical factors in aerospace manufacturing. The ability to print fiber-reinforced composites and nanocomposites with minimal issues further underscores its suitability for high-performance applications.

However, despite these advantages, FFF faces limitations, particularly concerning the thermal properties of thermoplastics, which restrict its use in high-temperature environments such as small satellite construction.

Thermosetting materials, with their superior thermal stability, are more appropriate for such applications, especially when electronic components are embedded within the structures. Conversely, technologies like material jetting (MJ), direct ink writing (DIW), and stereolithography (SLA) offer greater versatility in material selection, including thermosets and composites, but often encounter challenges related to filler incorporation, curing efficiency, and process speed. For instance, the presence of fillers such as fibers and nanoparticles can hinder curing and increase the risk of clogging, necessitating careful process control. DIW, in particular, excels in producing high-precision conductive paths for electronic devices, making it valuable for sensor and electronic component manufacturing. Material compatibility and process limitations influence the choice of technology based on specific application requirements. MJ technology's ability to print multiple materials simultaneously facilitates the creation of multifunctional components, although it demands meticulous pre-application material compatibility studies. SLS technology offers the advantage of printing both thermoplastics and thermosets, including elastomers, with high precision and surface

quality, reducing the need for multiple equipment investments. Nonetheless, its high material costs and limited recyclability pose challenges for large-scale production. Overall, the selection of a suitable 3D printing process depends on balancing factors such as material properties, production speed, component complexity, and cost considerations.

Despite technological progress, several limitations hinder the widespread adoption of 3D printing in aerospace applications. Quality control remains a critical concern, with issues like porosity, layer adhesion failures, and dimensional inaccuracies affecting the integrity and safety of printed parts. Regulatory compliance, governed by agencies such as the FAA, often necessitates extensive post-processing, which can be resource-intensive. The high investment costs for industrial-grade 3D printers further restrict access for small and medium-sized enterprises, limiting broader industry adoption. Additionally, the current inability to print large components restricts the manufacturing of sizable aerospace structures, emphasizing the need for ongoing research and development to overcome these barriers. Addressing these challenges is essential for fully realizing the potential of 3D printing technologies to revolutionize aerospace manufacturing, enabling lighter, more efficient, and complex components that meet stringent safety and performance standards. Based on the articles reviewed in this paper and additional references, the accuracy,[537] as well as the general advantages and disadvantages of these technologies and future trends, are summarized in Table 16.[13,439,538] It is worth noting that the accuracy reported in Table 16 may depend on the materials' properties.

Challenges and future perspectives

The use of 3D printing in space exploration is attracting considerable attention for its potential to transform how missions are conducted. By enabling the production of tools, components, and structures directly in space when needed, this technology could significantly reduce the need for expensive and lengthy resupply missions from Earth.

These abilities are crucial for supporting extended missions and establishing a lasting human presence beyond our planet.

In light of the limitations and disadvantages discussed in this review, the main challenge is the improvement of final quality, which opens new future research activities listed here:

• New design methods: to allow the production of multifunctional complex-shaped pieces, enhance designers' freedom, and reduce the use of connectors (such as bolts and screws), which weaken the material integrity.[539]

• New materials: stimuli-responsive, shape memory, and self-healing materials in 3D printing are still in an embryonic state, and not many attempts to use them in combination with fiber reinforcement for high-performance structures are investigated in the literature (A11). These kinds of materials are also suitable for morphing wings or integrated and distributed actuators in UAV applications.[303,540]

• Models for defect predictions: according to material properties and process parameters, simulation tools on an industrial scale could be helpful to predict in advance the defects, reducing limitations due to the poor final quality and inspection time.

• Machine asset: to guarantee larger piece fabrication, improve the manufacturing of nanocomposite materials, facilitate the insertion of fiber reinforcement, broaden the typology of materials that can be used with the same apparatus, improve contactless controllers and sensors for limiting parts defects (*e.g.*, chamber environment controller, temperature sensors for layer by layer temperature profile, cooling phase controller, and crystallinity).

• 3D printing for automated maintenance: although some examples of 3D-printed spare parts for maintenance purposes already exist, the time and costs are still high; an advanced scanning method of the portion to be repaired could facilitate its design phase.[539]

• Combining more than one printing technology: only a few attempts to combine the advantages of singular 3D printing technologies are present in the literature; however, this strategy could facilitate the manufacturing of multifunctional parts in a continuous way, usually requiring different materials and different processes.[410,541,542]

All these challenges and future perspectives refer to "for space" 3D printing. Although it is still in its early stages, "in space" 3D printing is the true challenge of the future. In-orbit manufacturing and maintenance are made possible by 3D printers on space stations and spacecraft. Long-duration missions could greatly benefit from this capacity, as it lessens the need to restock vital components from Earth.[543] M. Hoffmann *et al.*[544] wrote a recent review of "in space" additive manufacturing. The NASA office, in collaboration with the Air Force Space Command, the Air Force Research Laboratory's Space Vehicles Directorate, and the Space Technology Mission Directorate, requested that the US National Research Council (NRC) evaluate the feasibility, risks, and challenges of directly printing on board in space. According to the NASA NCR report,[545] "in space" 3D printing enables the manufacturing of components, recycling, creating sensors or entire satellites, and constructing structures that are difficult to manufacture on Earth or launch, utilizing resources on off-Earth surfaces. This revolutionary approach in the manufacturing system of tools for space missions will lead to a change in the organization and distribution of space on board space shuttles. However, a lot of work still needs to be done.

In comparison to additive manufacturing on Earth, additive manufacturing in space faces significantly greater systems engineering and industrial logistics challenges due to the zero-gravity and vacuum conditions. However, NASA has already developed "in space" verification and validation methods and "in space" materials characterization databases. "In space" 3D printing represents a long-term ambition that requires investments, standardization, certification, and infrastructure, as well as information-sharing (coordination and collaboration among multidisciplinary scientists) to determine

Table 16 Comparison of 3D printing technologies: accuracy, advantages, limitations and future trends

3D printing technology	Accuracy	Advantages	Limitations	Future trends
FFF	±0.5% (± 0.5 mm)	• Low material and process cost	• Limited to thermoplastic polymers	• New material formulations for high- speed production
		• Low printer cost	• Low resolution	• New renewable and bio-based high-performance materials
		• High fabrication speed	• Surface roughness	• Studies of material behavior in microgravity environment
		• Scalability	• Warpage defects	• Development of large format printer
		• Suitable for mass production on a large scale	• Difficulties in dispersing nanoparticles (high concentration of filler to get high electrical conductivity)	• Development of extrudable thermosetting materials (*e.g.* CAN or vitrimers)
		• Suitable for, high-performance composites, nanocomposites, and smart materials	• High anisotropic effects in fiber-reinforced composites	• Advanced thermal modeling and distortion control
DIW	±0.1% (± 0.1 mm)	• High resolution	• Time-consuming	• Development of inks with functional fillers and smart properties (shape memory and self-healing)
		• Suitable for thermoplastic, thermosetting and elastomers	• Low printing speed	• Developing a room-temperature curable ink that eliminates the need for post-processing
		• Good dispersion of higher content of filler to improve electrical properties	• Limited application field (mostly electrical) • Not suitable for composite materials (particles and long fiber-reinforced) • Limited to nanocomposites • Rapid solvent evaporation • Solvent toxicity	• Scale-up for larger, structurally relevant parts • Enlarging the study on DIW in microgravity
SLA	±0.2% (± 0.2 mm)	• High resolution	• High cost	• Developing monomer-free resins to meet health and safety standards.
		• Smooth surface finish	• Limited to thermosets	• Nanocomposite resins for structural enhancement
		• Suitable for flexible and rigid structures	• Issues for nanocomposite and composite materials	• Addressing challenges for microgravity SLA printing
		• Suitable for high-temperature resistance applications	• Not suitable for composite materials (long fiber-reinforced) • Toxicity of uncured resin and photoinitiator • Size limitation	
MJ	±0.05–0.1 mm	• High resolution	• High fabrication cost for large volumes	• Multi-material jetting with localized property control
		• Smooth surface finish	• Interface material defects	• Enlarge the materials catalogue
		• Suitable for multifunctional components	• Not suitable for composite materials (long fiber-reinforced)	• Study of materials compatibility
		• Possibility to simultaneously print multiple materials		• Study on smart materials
		• High fabrication speed		
SLS	±0.3% (± 0.3 mm)	• No need for material support	• High cost of raw materials	• Promising results for printing high-performance polymers (PEEK, PEI)
		• Good strength of the final object	• Surface defects	• Study of SLS with fiber, ceramic, or nanoparticle reinforcements
		• Suitable for thermosetting, thermoplastic and elastomeric polymers	• Warpage defects	• Powder reuse strategies for sustainability
		• Suitable for nanocomposites	• Incomplete melting and cracks • Oxidation and degradation • Not suitable for composite materials (long fiber-reinforced) • Not suitable for mass production	• Increase in certifiable structural aerospace components

the roadmap.[545] Furthermore, considering the applications in the biotech sector, NASA is working on 3D bioprinting research, with many different intended applications, ranging from creating human tissues for medical purposes to the development of bio-based materials for space exploration. This requires using living cells, proteins, and nutrients as initial materials to potentially print human tissues for treating injuries and diseases, as well as fabricating entire organs. NASA is also exploring the potential application of 3D printing for creating bioreactors and other tools for in-space manufacturing and resource utilization. Although 3D bioprinting may seem far removed from the aerospace field, it offers the unique potential for creating cell and tissue models for basic space research, examining the effects of cosmic radiation and microgravity on various human tissue types. Furthermore, bioprinting can create clinically useful tissue grafts for astronauts' autonomous medical treatment options in long-term and far space missions to come.[546]

Author contributions

F. Aliberti: conceptualization, investigation, writing – original draft, visualization, writing – review and editing. R. Longo: methodology, investigation, visualization, and resources. M. Raimondo: methodology, investigation, visualization, and resources. R. Pantani: methodology, investigation, and supervision. L. Vertuccio: methodology, investigation, visualization, and resources. L. Guadagno: conceptualization, investigation, writing – review and editing, supervision, funding acquisition, and project administration.

Conflicts of interest

There are no conflicts to declare.

Data availability

No primary research results, software or code have been included and no new data were generated or analysed as part of this review.

Acknowledgements

This research was funded by the Italian Ministry of University and Research – PRIN 2022 project "Integration of Continuous Fibers and Self-healing agents in 3D printed thermoplastic composites (INFINITE)" (Prot. 2022AK TCPH).

References

1 D. Xu, W. Yang and P. Cao, *Composites, Part B*, 2025, **299**, 112443.
2 W. Xu, S. Jambhulkar, Y. Zhu, D. Ravichandran, M. Kakarla, B. Vernon, D. G. Lott, J. L. Cornella, O. Shefi, G. Miquelard-Garnier, Y. Yang and K. Song, *Composites, Part B*, 2021, **223**, 109102.
3 F. Zhang, S. Zhou, H. You, G. Zhang, J. Yang and Y. Shi, *Composites, Part B*, 2025, **297**, 112335.
4 S. A. M. Tofail, E. P. Koumoulos, A. Bandyopadhyay, S. Bose, L. O'Donoghue and C. Charitidis, *Mater. Today*, 2018, **21**, 22–37.
5 I. Karakurt and L. Lin, *Curr. Opin. Chem. Eng.*, 2020, **28**, 134–143.
6 W. Gao, Y. Zhang, D. Ramanujan, K. Ramani, Y. Chen, C. B. Williams, C. C. L. Wang, Y. C. Shin, S. Zhang and P. D. Zavattieri, *Comput.-Aided Des.*, 2015, **69**, 65–89.
7 P. Spiros and T. Konstantinos, *Revolutionizing Aircraft Materials and Processes*, Springer International Publishing, 2020.
8 L. Rueschhoff, *Ceramic Additive for Aerospace*, Springer International Publishing, 2021, pp. 119–133, DOI: 10.1007/978-3-030-70736-1_10.
9 M. Pant, P. Pidge, L. Nagdeve and H. Kumar, *Rev. Compos. Mater. Av.*, 2021, **31**, 109–115.
10 C. W. J. Lim, K. Q. Le, Q. Lu and C. H. Wong, *IEEE Potentials*, 2016, **35**, 18–22.
11 M. C. Halbig and M. Singh, *Additive Manufacturing of SiC Based Ceramics and Ceramic Matrix Composites*, Vancouver, British Columbia, 2015.
12 J. E. Grady, M. C. Halbig and M. Singh, *Advanced CMCs, Additive Manufacturing, and Joining/Integration Technologies*, NASA Glenn Research Center, Cleveland, OH, 2019.
13 A. D. Valino, J. R. C. Dizon, A. H. Espera, Q. Chen, J. Messman and R. C. Advincula, *Prog. Polym. Sci.*, 2019, **98**, 101162.
14 P. Kumar, K. K. Sadasivuni, B. Al Mangour and M. S. A. bin Majid, *High-Performance Composite Structures*, Springer, Singapore, 2022.
15 A. Bhat, S. Budholiya, S. Aravind Raj, M. T. H. Sultan, D. Hui, A. U. Md Shah and S. N. A. Safri, *Nanotechnol. Rev.*, 2021, **10**, 237–253.
16 D. Lehmhus, M. Busse, A. Von Hehl and E. Jägle, *MATEC Web Conf.*, 2018, **188**, 03013.
17 S. Salifu, O. Ogunbiyi and P. A. Olubambi, *Int. J. Adv. Des. Manuf. Technol.*, 2022, **122**, 577–600.
18 M. C. Halbig, *Additive Manufacturing Technologies for Aerospace Applications*, NASA Glenn Research Center, 2019.
19 B. Chang, P. Parandoush, X. Li, S. Ruan, C. Shen, R. A. Behnagh, Y. Liu and D. Lin, *Polym. Compos.*, 2020, **41**, 4706–4715.
20 Fiber-Metal Laminate Manufacturing Technique https://technology.nasa.gov/patent/LAR-TOPS-170.
21 A. Ghobadian, I. Talavera, A. Bhattacharya, V. Kumar, J. A. Garza-Reyes and N. O'Regan, *Int. J. Prod. Econ.*, 2020, **219**, 457–468.
22 J. C. Najmon, S. Raeisi and A. Tovar, *Additive manufacturing for the aerospace industry*, 2019, pp. 7–31.
23 S. C. Altıparmak and B. Xiao, *J. Manuf. Process.*, 2021, **68**, 728–738.

24 S. Antony Jose, J. Jackson, J. Foster, T. Silva, E. Markham and P. L. Menezes, *J. Manuf. Mater. Process.*, 2025, **9**, 84.
25 A. Raza and A. Schaffer, *Design Optimization and Polymer Material Selection for Enhancing Structural Integrity in 3D Printed Aerospace Components*, 2024, DOI: **10.13140/RG.2.2.29493.28649**.
26 W. M. Van Den Brink, F. Van Der Klift, R. Bruins and M. J. M. Hermans, Design and optimization method for 3D printed carbon reinforced aircraft components, in *21st International Conference on Composite Materials, ICCM, 2017*, International Committee on Composite Materials, 2017, p. 3193.
27 D. Bhate, *Design for Additive Manufacturing: Concepts and Considerations for the Aerospace Industry*, SAE International, 2018.
28 S. Raja, H. M. Al-Tmimi, G. K. Ghadir, M. A. Mustafa, Z. K. Alani, M. A. Rusho and N. Rajeswari, *Appl. Chem. Eng.*, 2024, **7**, 1875.
29 H. I. Medellin-Castillo and J. Zaragoza-Siqueiros, *Chin. J. Mech. Eng.*, 2019, 32.
30 Y. Chen, Q. Wang, C. Wang, P. Gong, Y. Shi, Y. Yu and Z. Liu, *Appl. Sci.*, 2021, **11**, 6671.
31 A. A. Shapiro, J. P. Borgonia, Q. N. Chen, R. P. Dillon, B. McEnerney, R. Polit-Casillas and L. Soloway, *J. Spacecr. Rockets*, 2016, **53**, 952–959.
32 A. Alfaify, M. Saleh, F. M. Abdullah and A. M. Al-Ahmari, *Sustainability*, 2020, **12**, 7936.
33 A. Kumar, P. Kumar, N. Sharma and A. K. Srivastava, *3D printing technologies: digital manufacturing, artificial intelligence, industry 4.0*, Walter de Gruyter GmbH & Co KG, 2024.
34 D. Goto, R. Matsuzaki and A. Todoroki, *Adv. Compos. Mater.*, 2024, **33**, 1175–1190.
35 S. Rahmani Dabbagh, O. Ozcan and S. Tasoglu, *Methods*, 2022, **206**, 27–40.
36 Y. Yang, Y. Wang, B. Xue, C. Wang and B. Yang, *Aerospace*, 2025, **12**, 38.
37 G. Kévin, F. Eric, G. Pierre-Loïc, J. R. Julian, D. B. John, G. Martha and H. Kerianne, *Logic in Computer Science*, 2017, DOI: **10.48550/arxiv.1705.00960**.
38 T. S. Tamir, G. Xiong, Q. Fang, Y. Yang, Z. Shen, M. Zhou and J. Jiang, *Int. J. Comput. Integr. Manuf.*, 2023, **36**, 1362–1378.
39 G. D. Goh, S. L. Sing and W. Y. Yeong, *Artif. Intell. Rev.*, 2021, **54**, 63–94.
40 I. Rojek, D. Mikołajewski, M. Kempiński, K. Galas and A. Piszcz, *Appl. Sci.*, 2025, **15**, 1781.
41 A. K. Adeleke, D. J. P. Montero, O. A. Lottu, N. Ninduwezuor-Ehiobu and E. C. Ani, *World J. Adv. Res. Rev.*, 2024, **21**, 1149–1160.
42 C. Radhika, R. Shanmugam, M. Ramoni and G. Bk, *Mater. Res. Exp.*, 2024, **11**, 022001.
43 V. Danylenko and V. Lipovskyi, *J. Rocket-Space Technol.*, 2025, **34**, 21–30.
44 M. S. Karkun and S. Dharmalinga, *Int. J. Aviat. Aeronaut. Aerosp.*, 2022, **9**(2), 4, DOI: **10.15394/ijaaa.2022.1708**.
45 A. Kausar, *Adv. Mater. Sci.*, 2024, **24**, 67–96.
46 F. Mami, J. P. Revéret, S. Fallaha and M. Margni, *J. Ind. Ecol.*, 2017, **21**, S37–S48.
47 D. W. Martinez, M. T. Espino, H. M. Cascolan, J. L. Crisostomo and J. R. C. Dizon, *Key Eng. Mater.*, 2022, **913**, 27–34.
48 P. Mishra, S. Sood, V. Bharadwaj, A. Aggarwal and P. Khanna, *Polymers*, 2023, **15**, 546.
49 D. Romero-Fierro, M. Bustamante-Torres, F. Bravo-Plascencia, A. Esquivel-Lozano, J.-C. Ruiz and E. Bucio, *Polymers*, 2022, **14**, 4084.
50 Z. Wawryniuk, E. Brancewicz-Steinmetz and J. Sawicki, *Int. J. Adv. Des. Manuf. Technol.*, 2024, **134**(7), 3083–3105.
51 S. C. Ligon, R. Liska, J. Stampfl, M. Gurr and R. Mülhaupt, *Chem. Rev.*, 2017, **117**, 10212–10290.
52 C. Ajinjeru, V. Kishore, P. Liu, J. Lindahl, A. A. Hassen, V. Kunc, B. Post, L. Love and C. Duty, *Addit. Manuf.*, 2018, **21**, 125–132.
53 R. O. Ebewele, 2000, DOI: **10.1201/9781420057805**.
54 D. V. A. Ceretti, M. Edeleva, L. Cardon and D. R. D'Hooge, *Molecules*, 2023, **28**, 2344.
55 S. R. Subramaniam, M. Samykano, S. K. Selvamani, W. K. Ngui, K. Kadirgama, K. Sudhakar and M. S. Idris, 3D printing: overview of PLA progress, in *AIP conference proceedings*, AIP Publishing LLC, 2019, vol. 2059(1), p. 020015.
56 H. Baqasah, F. He, B. A. Zai, M. Asif, K. A. Khan, V. K. Thakur and M. A. Khan, *Polymers*, 2019, **11**, 2079.
57 N. Verma, P. Awasthi, A. Gupta and S. S. Banerjee, *Macromol. Mater. Eng.*, 2023, **308**, 2200421.
58 N. Vidakis, M. Petousis and J. D. Kechagias, *Prog. Addit. Manuf.*, 2022, **7**, 713–722.
59 A. Costanzo, U. Croce, R. Spotorno, S. E. Fenni and D. Cavallo, *Polymers*, 2020, **12**, 2980.
60 A. L. Slonov, A. A. Khashirov, A. A. Zhansitov, E. V. Rzhevskaya and S. Y. Khashirova, *Rapid Prototyp. J.*, 2018, **24**, 1124–1130.
61 N. H. Obaeed and W. Hamdan, *Adv. Sci. Technol. Res. J.*, 2024, **18**, 349–359.
62 D. Acierno and A. Patti, *Materials*, 2023, **16**, 7664.
63 A. Jandyal, I. Chaturvedi, I. Wazir, A. Raina and M. I. Ul Haq, *Sustainable Oper. Comput.*, 2022, **3**, 33–42.
64 H. C. Kim, R. Tu and H. A. Sodano, *Composites, Part B*, 2024, **279**, 111444.
65 K. Vijay, S. Kashma, S. Rakesh and K. Susheel, *Conjugated Polymers for Next-Generation Applications. Synthesis, Properties and Optoelectrochemical Devices*, Woodhead Publishing, 2022.
66 D. V. Rosato and D. V. Rosato, Injection molding, in *Plastics Processing Data Handbook*, Springer Netherlands, Dordrecht, 1990, pp. 38–90.
67 G. Holden, *Thermoplastic Elastomers*, Elsevier, 2024, pp. 97–113, DOI: **10.1016/b978-0-323-88667-3.00020-5**.
68 M. Picard, A. K. Mohanty and M. Misra, *RSC Adv.*, 2020, **10**, 36058–36089.
69 S. Chen, J. Lu and J. Feng, *Ind. Eng. Chem. Res.*, 2018, **57**, 3923–3931.
70 G. Cicala, G. Ognibene, S. Portuesi, I. Blanco, M. Rapisarda, E. Pergolizzi and G. Recca, *Materials*, 2018, **11**, 285.

71 Y. Geng, H. He, H. Liu and H. Jing, *Polym. Adv. Technol.*, 2020, **31**, 2848–2862.
72 J. Yang, R. Su, H. Ying, L. Hu and X. Ruan, *Mater. Today Commun.*, 2023, **36**, 106764.
73 M. Rinaldi, T. Ghidini, F. Cecchini, A. Brandao and F. Nanni, *Composites, Part B*, 2018, **145**, 162–172.
74 D. P. Simunec, J. Jacob, A. E. Z. Kandjani, A. Trinchi and A. Sola, *Eur. Polym. J.*, 2023, **201**, 112553.
75 E. Padovano, M. Galfione, P. Concialdi, G. Lucco and C. Badini, *Appl. Sci.*, 2020, **10**, 3170.
76 S. Guessasma, S. Belhabib and H. Nouri, *Macromol. Mater. Eng.*, 2019, **304**, 1800793.
77 S. Guessasma, S. Belhabib and H. Nouri, *J. Appl. Polym. Sci.*, 2021, **138**, 50162.
78 S. Kobenko, D. Dejus, J. Jātnieks, D. Pazars and T. Glaskova-Kuzmina, *Polymers*, 2022, **14**, 1538.
79 A. Kafi, H. Wu, J. Langston, O. Atak, H. Kim, S. Kim, W. P. Fahy, R. Reber, J. Misasi, S. Bateman and J. H. Koo, *J. Appl. Polym. Sci.*, 2020, **137**, 49117.
80 M. R. Vengatesan, A. M. Varghese and V. Mittal, *Thermal properties of thermoset polymers*, Elsevier, 2018, pp. 69–114, DOI: **10.1016/b978-0-08-101021-1.00003-4**.
81 **https://texasinjectionmolding.com/injection-molded-composites-outperform-thermoset-composites-on-price-and-performance/**.
82 S. Utekar, V. K. Suriya, N. More and A. Rao, *Composites, Part B*, 2021, **207**, 108596.
83 W. Wu Klingler, A. Bifulco, C. Polisi, Z. Huang and S. Gaan, *Composites, Part B*, 2023, **258**, 110667.
84 L. Guadagno, R. Longo, M. Raimondo, L. Vertuccio, F. Aliberti, L. Bonadies, S. Morciano, L. Longo, R. Pantani and E. Calabrese, *Polymers*, 2025, **17**, 1241.
85 Y. Liu, Z. Yu, B. Wang, P. Li, J. Zhu and S. Ma, *Green Chem.*, 2022, **24**, 5691–5708.
86 N. Ramawat, N. Sharma, P. Yamba and M. A. T. Sanidhi, *Mater. Today: Proc.*, 2023, DOI: **10.1016/j.matpr.2023.05.386**.
87 W. Post, A. Susa, R. Blaauw, K. Molenveld and R. J. I. Knoop, *Polym. Rev.*, 2020, **60**, 359–388.
88 D. K. Schneiderman and M. A. Hillmyer, *Macromolecules*, 2017, **50**, 3733–3749.
89 A. Durand-Silva, K. P. Cortés-Guzmán, R. M. Johnson, S. D. Perera, S. D. Diwakara and R. A. Smaldone, *ACS Macro Lett.*, 2021, **10**, 486–491.
90 Y. Zhang, L. Zhang, G. Yang, Y. Yao, X. Wei, T. Pan, J. Wu, M. Tian and P. Yin, *J. Mater. Sci. Technol.*, 2021, **92**, 75–87.
91 R. Abedin, X. Feng, J. Pojman, S. Ibekwe, P. Mensah, I. Warner and G. Li, *ACS Appl. Polym. Mater.*, 2022, **4**, 1183–1195.
92 A. Li, A. Challapalli and G. Li, *Sci. Rep.*, 2019, 9.
93 A. Li, J. Fan and G. Li, *J. Mater. Chem. A*, 2018, **6**, 11479–11487.
94 Z. Jiang, B. Diggle, M. L. Tan, J. Viktorova, C. W. Bennett and L. A. Connal, *Adv. Sci.*, 2020, **7**, 2001379.
95 Y. Hong, I. Azcune, A. Rekondo and E. Saiz, *Mater. Des.*, 2024, **246**, 113344.
96 M. Mukhtarkhanov, A. Perveen and D. Talamona, *Micromachines*, 2020, **11**, 946.
97 W. A. Green, 2010, DOI: **10.1201/9781439827468**.
98 A. Bagheri and J. Jin, *ACS Appl. Polym. Mater.*, 2019, **1**, 593–611.
99 E. J. Murphy, R. E. Ansel and J. J. Krajewski, *US Pat.*, 4942001, 1990.
100 **https://www.tctmagazine.com/additive-manufacturing-in-the-aircraft-cabin/**.
101 V. S. D. Voet, T. Strating, G. H. M. Schnelting, P. Dijkstra, M. Tietema, J. Xu, A. J. J. Woortman, K. Loos, J. Jager and R. Folkersma, *ACS Omega*, 2018, **3**, 1403–1408.
102 R. Palucci Rosa and G. Rosace, *Macromol. Mater. Eng.*, 2021, **306**, 2100345.
103 J. Casado, O. Konuray, A. Roig, X. Fernández-Francos and X. Ramis, *Eur. Polym. J.*, 2022, **173**, 111256.
104 I. Cazin, K. Plevová, W. Alabiso, E. Vidović and S. Schlögl, *Adv. Eng. Mater.*, 2024, 26.
105 R. Yu, X. Yang, Y. Zhang, X. Zhao, X. Wu, T. Zhao, Y. Zhao and W. Huang, *ACS Appl. Mater. Interfaces*, 2017, **9**, 1820–1829.
106 J. P. Moore and C. B. Williams, *Rapid Prototyp. J.*, 2015, **21**, 675–685.
107 M. León-Calero, S. C. Reyburn Valés, Á. Marcos-Fernández and J. Rodríguez-Hernandez, *Polymers*, 2021, **13**, 3551.
108 B. B. Sahu, S. Moharana and P. K. Behera, *Elastomeric-Based Composite Materials for Engineering Applications*, Springer Nature, Singapore, 2024, pp. 329–355, DOI: **10.1007/978-981-97-2075-0_11**.
109 A. Dasgupta and P. Dutta, *J. Rubber Res.*, 2024, **27**, 137–157.
110 R. Setter and K. Wudy, *Polym. Test.*, 2024, **132**, 108366.
111 J. Herzberger, J. M. Sirrine, C. B. Williams and T. E. Long, *Prog. Polym. Sci.*, 2019, **97**, 101144.
112 X. Chen, C. E. Zawaski, G. A. Spiering, B. Liu, C. M. Orsino, R. B. Moore, C. B. Williams and T. E. Long, *ACS Appl. Mater. Interfaces*, 2020, **12**, 32006–32016.
113 S. M. Desai, R. Y. Sonawane and A. P. More, *Polym. Adv. Technol.*, 2023, **34**, 2061–2082.
114 J. Fei, Y. Rong, L. Zhu, H. Li, X. Zhang, Y. Lu, J. An, Q. Bao and X. Huang, *Macromol. Rapid Commun.*, 2023, **44**, 2300211.
115 T. White and R. Verduzco, *Soft Matter*, 2017, **13**, 4320.
116 K. A. Etling, *US Pat.*, 8342447, 2013.
117 M. R. Khorrami, D. P. Lockard, J. B. Moore, J. Su, T. L. Turner, J. C. Lin, K. M. Taminger, S. K. Kahng and S. A. Verden, *Elastically Deformable Side-Edge Link for Trailing-Edge Flap Aeroacoustic Noise Reduction*, NASA Glenn Research Center, 2014.
118 P. K. Penumakala, J. Santo and A. Thomas, *Composites, Part B*, 2020, **201**, 108336.
119 S. Singh and R. Singh, *Rapid Prototyp. J.*, 2020, **26**, 225–237.
120 C. Kaynak and S. D. Varsavas, *J. Thermoplast. Compos. Mater.*, 2019, **32**, 501–520.
121 F. Stan, N.-V. Stanciu, A.-M. Constantinescu and C. Fetecau, *J. Eng. Ind.*, 2021, **143**, 1–33.
122 C. Carradero Santiago, C. Randall-Posey, A.-A. Popa, L. Duggen, B. Vuksanovich, P. Cortes and E. Macdonald, *IEEE Access*, 2020, **8**, 41394–41402.

123 J. F. Christ, C. J. Hohimer, N. Aliheidari, A. Ameli, C. Mo and P. Pötschke.
124 R. Yadav, M. Tirumali, X. Wang, M. Naebe and B. Kandasubramanian, *Def. Technol.*, 2020, **16**, 107–118.
125 A. B. Rashid, M. Haque, S. M. M. Islam and K. M. R. Uddin Labib, *Heliyon*, 2024, **10**, e24692.
126 K. Ayesha, *Polymeric nanocomposites with carbonaceous nanofillers for aerospace applications*, Woodhead Publishing, 2022.
127 P. Mazurek, S. Vudayagiri and A. L. Skov, *Chem. Soc. Rev.*, 2019, **48**, 1448–1464.
128 C. Luo, C. Chung, N. A. Traugutt, C. M. Yakacki, K. N. Long and K. Yu, *ACS Appl. Mater. Interfaces*, 2021, **13**, 12698–12708.
129 J. A. Butenegro, M. Bahrami, J. Abenojar and M. Á. Martínez, *Materials*, 2021, **14**, 6401.
130 L. Samant, F. A. O. Fernandes, S. Jose and R. J. Alves De Sousa, *Natural Composites in Aircraft Structures*, Springer International Publishing, 2022, pp. 113–126, DOI: 10.1007/978-3-030-91873-6_5.
131 R. Dermanaki Farahani and M. Dubé, *Adv. Eng. Mater.*, 2018, **20**, 1700539.
132 D. Ponnamma, Y. Yin, N. Salim, J. Parameswaranpillai, S. Thomas and N. Hameed, *Composites, Part B*, 2021, **204**, 108493.
133 A. Sudhin, M. Remanan, G. Ajeesh and K. Jayanarayanan, *Mater. Today: Proc.*, 2020, **24**, 453–462.
134 K. Yu and M. L. Dunn, *Langmuir*, 2024, **40**, 8751–8759.
135 D.-K. Lee, J. Yoo, H. Kim and S.-H. Park, *Carbon Lett.*, 2024, **34**, 133–140.
136 F. Aliberti, L. Vertuccio, R. Longo, A. Sorrentino, R. Pantani, L. Guadagno and M. Raimondo, *Nanomaterials*, 2025, **15**, 994.
137 E. Lorenzi, R. Arrigo and A. Frache, *Polymers*, 2024, **16**, 858.
138 V. T. Rathod, J. S. Kumar and A. Jain, *Appl. Nanosci.*, 2017, **7**, 519–548.
139 M. Jalali, S. Dauterstedt, A. Michaud and R. Wuthrich, *Composites, Part B*, 2011, **42**, 1420–1426.
140 S. Dul, L. Fambri and A. Pegoretti, *Nanomaterials*, 2018, **8**, 49.
141 X. Wei, D. Li, W. Jiang, Z. Gu, X. Wang, Z. Zhang and Z. Sun, *Sci. Rep.*, 2015, **5**, 11181.
142 L. Lei, Z. Yao, J. Zhou, B. Wei and H. Fan, *Compos. Sci. Technol.*, 2020, **200**, 108479.
143 L. Guadagno, C. Naddeo, M. Raimondo, G. Gorrasi and V. Vittoria, *Polym. Degrad. Stab.*, 2010, **95**, 1614–1626.
144 L. Guadagno, M. Raimondo, C. Naddeo, A. Di Bartolomeo and K. Lafdi, *J. Polym. Sci., Part B: Polym. Phys.*, 2012, **50**, 963–975.
145 C. Naddeo, L. Vertuccio, G. Barra and L. Guadagno, *Materials*, 2017, **10**, 943.
146 C. Naddeo, L. Guadagno, S. De Luca, V. Vittoria and G. Camino, *Polym. Degrad. Stab.*, 2001, **72**, 239–247.
147 C. Naddeo, L. Guadagno and V. Vittoria, *Polym. Degrad. Stab.*, 2004, **85**, 1009–1013.
148 A. Salas, H. Pazniak, J. Gonzalez-Julian, S. Bianco, J. Amici, T. Ouisse, I. Roppolo and M. Cocuzza, *Composites, Part B*, 2023, **263**, 110854.
149 W. Bi, G. Gao, C. Li, G. Wu and G. Cao, *Prog. Mater. Sci.*, 2024, **142**, 101227.
150 Z. Rezaei and E. Prince, *Chem. Sci.*, 2025, **16**, 14839–14864.
151 Z. X. Khoo, J. E. M. Teoh, Y. Liu, C. K. Chua, S. Yang, J. An, K. F. Leong and W. Y. Yeong, *Virtual Phys. Prototyp.*, 2015, **10**, 103–122.
152 R. Longo, L. Guadagno, F. Aliberti, L. Schiavo, M. Oliviero, A. Sorrentino, M. Fiorentino and L. Vertuccio, *Appl. Mater. Today*, 2025, **46**, 102882.
153 M. Su and Y. Song, *Chem. Rev.*, 2022, **122**, 5144–5164.
154 G. Donati, A. De Nicola, G. Munaò, M. Byshkin, L. Vertuccio, L. Guadagno, R. Le Goff and G. Milano, *Nanoscale Adv.*, 2020, **2**, 3164–3180.
155 L. Guadagno, F. Foglia, R. Pantani, M. D. Romero-Sanchez, B. Calderón and L. Vertuccio, *Nanomaterials*, 2020, **10**, 1343.
156 L. Guadagno, L. Vertuccio, F. Foglia, M. Raimondo, G. Barra, A. Sorrentino, R. Pantani and E. Calabrese, *Composites, Part B*, 2021, **224**, 109208.
157 L. Vertuccio, F. De Santis, R. Pantani, K. Lafdi and L. Guadagno, *Composites, Part B*, 2019, **162**, 600–610.
158 W. Bauhofer and J. Z. Kovacs, *Compos. Sci. Technol.*, 2009, **69**, 1486–1498.
159 I. Balberg and N. Binenbaum, *Phys. Rev. A: At., Mol., Opt. Phys.*, 1987, **35**, 5174–5177.
160 L. Berhan and A. M. Sastry, *Phys. Rev. E: Stat., Nonlinear, Soft Matter Phys.*, 2007, **75**, 041120.
161 R. Longo, L. Vertuccio, F. Aliberti, M. Raimondo, R. Pantani, S. Russo, G. Iannuzzo and L. Guadagno, *Adv. Compos. Hybrid Mater.*, 2025, **8**, 268.
162 L. Guadagno, L. Vertuccio, F. Aliberti, E. Calabrese, M. Raimondo, R. Pantani and R. Longo, *Compos., Part C: Open Access*, 2025, **17**, 100609.
163 L. Guadagno, L. Vertuccio, F. Aliberti, R. Pantani, M. Raimondo, M. Catauro and R. Longo, *Composites, Part B*, 2025, **292**, 112079.
164 J. Wang, J. Frantz, E. Chumbley, A. Samad and H. Hu, *Molecules*, 2025, **30**, 3472.
165 L. Zhou, X. Yi and Q. Liu, *Drones*, 2023, **7**, 709.
166 F. Aliberti, L. Guadagno, R. Longo, M. Raimondo, R. Pantani, A. Sorrentino, M. Catauro and L. Vertuccio, *Nanomaterials*, 2024, **14**, 1761.
167 L. Guadagno, F. Aliberti, R. Longo, M. Raimondo, R. Pantani, A. Sorrentino, M. Catauro and L. Vertuccio, *Mater. Des.*, 2023, **225**, 111507.
168 L. Vertuccio, L. Guadagno, G. Spinelli, P. Lamberti, V. Tucci and S. Russo, *Composites, Part B*, 2016, **107**, 192–202.
169 N. Hu, Y. Karube, M. Arai, T. Watanabe, C. Yan, Y. Li, Y. Liu and H. Fukunaga, *Carbon*, 2010, **48**, 680–687.
170 T. Nguyen, T. Dinh, H.-P. Phan, T. A. Pham, V. T. Dau, N.-T. Nguyen and D. V. Dao, *Mater. Horiz.*, 2021, **8**, 2123–2150.
171 F. Ksica, Z. Hadas and J. Hlinka, Application of piezoelectric sensors for structural health monitoring in aerospace, in *2018 5th IEEE International Workshop on*

Metrology for AeroSpace, MetroAeroSpace, IEEE, 2018, pp. 596–601.
172 A. A. Basheer, *Aircr. Eng.*, 2020, **92**, 1027–1035.
173 R. Kar-Gupta and T. A. Venkatesh, *Acta Mater.*, 2008, **56**, 3810–3823.
174 H. Kim, F. Torres, D. Villagran, C. Stewart, Y. Lin and T. L. B. Tseng, *Macromol. Mater. Eng.*, 2017, **302**, 1700229.
175 A. Aabid, B. Parveez, M. A. Raheman, Y. E. Ibrahim, A. Anjum, M. Hrairi, N. Parveen and J. Mohammed Zayan, *Actuators*, 2021, **10**, 101.
176 J. Käsgen and D. Mayer, *Appl. Mech. Mater.*, 2007, **7–8**, 295–300.
177 K. P. Duffy, B. A. Lerch, N. G. Wilmoth, N. Kray and G. Gemeinhardt, *Mechanical and Vibration Testing of Carbon Fiber Composite Material with Embedded Piezoelectric Sensors*, 2013.
178 A. Megdich, M. Habibi and L. Laperrière, *Mater. Today Commun.*, 2023, **35**, 105541.
179 D. G. Bekas, K. Tsirka, D. Baltzis and A. S. Paipetis, *Composites, Part B*, 2016, **87**, 92–119.
180 E. Calabrese, L. Guadagno, M. Raimondo, A. Sorrentino, S. Russo, P. Longo and A. Mariconda, *Macromol. Mater. Eng.*, 2023, **308**, 2200500.
181 L. Guadagno, C. Naddeo, L. Vertuccio, E. Calabrese, G. Barra, M. Raimondo, S. Russo and G. Iannuzzo, *US Pat.*, 17/908,029, 2023.
182 L. Guadagno, M. Raimondo, R. Longo, F. Aliberti, J. Passaro, A. Piccirillo and E. Calabrese, *Macromol. Symp.*, 2023, **411**, 2200157.
183 L. Vertuccio, E. Calabrese, M. Raimondo, M. Catauro, A. Sorrentino, C. Naddeo, R. Longo and L. Guadagno, *Aerospace*, 2023, **10**, 476.
184 L. Guadagno, C. Naddeo, M. Raimondo, G. Barra, L. Vertuccio, A. Sorrentino, W. H. Binder and M. Kadlec, *Composites, Part B*, 2017, **128**, 30–38.
185 L. Guadagno, L. Vertuccio, C. Naddeo, G. Barra, M. Raimondo, A. Sorrentino, W. H. Binder, P. Michael, S. Rana and E. Calabrese, *Mater. Today: Proc.*, 2021, **34**, 243–249.
186 L. Guadagno, L. Vertuccio, C. Naddeo, E. Calabrese, G. Barra, M. Raimondo, A. Sorrentino, W. H. Binder, P. Michael and S. Rana, *Composites, Part B*, 2019, **157**, 1–13.
187 L. Guadagno, M. Raimondo, M. Catauro, A. Sorrentino and E. Calabrese, *J. Therm. Anal. Calorim.*, 2022, **147**, 5463–5472.
188 L. Guadagno, L. Vertuccio, G. Barra, C. Naddeo, A. Sorrentino, M. Lavorgna, M. Raimondo and E. Calabrese, *Polymer*, 2021, **223**, 123718.
189 S. Wang and M. W. Urban, *Nat. Rev. Mater.*, 2020, **5**, 562–583.
190 S. K. Pandey, S. Mishra, S. Ghosh, R. Rohan and P. K. Maji, *Polym. Eng. Sci.*, 2024, **64**, 951–987.
191 M. R. Islam, S. Afroj, J. Yin, K. S. Novoselov, J. Chen and N. Karim, *Adv. Sci.*, 2024, **11**, 2304140.
192 Y. Liu, L. Wang, Y. Liu, F. Zhang and J. Leng, *Composites Commun.*, 2024, **51**, 102062.
193 X. Mu and G. Li, *Chem. Eng. J.*, 2024, **500**, 157358.
194 S. Grauzeliene, A.-S. Schuller, C. Delaite and J. Ostrauskaite, *Eur. Polym. J.*, 2023, **198**, 112424.
195 V. Sereikaite, A. Navaruckiene, V. Raudoniene, D. Bridziuviene, P. Cerkauskas, S. Lileikis, K. Pamakstys, E. Rainosalo, A.-S. Schuller, C. Delaite and J. Ostrauskaite, *Biomacromolecules*, 2025, **26**, 4584–4594.
196 U. Shaukat, A. Thalhamer, E. Rossegger and S. Schlögl, *Addit. Manuf.*, 2024, **79**, 103930.
197 A. Yadav, S. K. Singh, S. Das, S. Kumar and A. Kumar, *Polym. Compos.*, 2025, DOI: **10.1002/pc.29707**.
198 O. A. Alo, D. Mauchline and I. O. Otunniyi, *Adv. Eng. Mater.*, 2022, **24**, 2101219.
199 G. M. Vasquez, C. E. Majewski, B. Haworth and N. Hopkinson, *Addit. Manuf.*, 2014, **1–4**, 127–138.
200 Z. D. Pritchard, M. P. De Beer, R. J. Whelan, T. F. Scott and M. A. Burns, *Adv. Mater. Technol.*, 2019, **4**, 1900700.
201 A. Andreu, H. Lee, J. Kang and Y. J. Yoon, *Adv. Funct. Mater.*, 2024, **34**, 2315046.
202 K. Yu, A. Xin, H. Du, Y. Li and Q. Wang, *NPG Asia Mater.*, 2019, **11**, 7.
203 O. S. Carneiro, A. F. Silva and R. Gomes, *Mater. Des.*, 2015, **83**, 768–776.
204 W. Zhong, F. Li, Z. Zhang, L. Song and Z. Li, *Mater. Sci. Eng. A*, 2001, **301**, 125–130.
205 J. Yin, C. Lu, J. Fu, Y. Huang and Y. Zheng, *Mater. Des.*, 2018, **150**, 104–112.
206 A. S. De Leòn, A. Domìnguez-Calvo and S. I. Molina, *Mater. Des.*, 2019, **182**, 108044.
207 C. R. Rocha, A. R. Torrado Perez, D. A. Roberson, C. M. Shemelya, E. Macdonald and R. B. Wicker, *J. Mater. Res.*, 2014, **29**, 1859–1866.
208 F. Aliberti, M. Oliviero, R. Longo, L. Guadagno and A. Sorrentino, *Polymers*, 2025, **17**, 156.
209 P. Geng, J. Zhao, W. Wu, W. Ye, Y. Wang, S. Wang and S. Zhang, *J. Manuf. Process.*, 2019, **37**, 266–273.
210 M. Golab, S. Massey and J. Moultrie, *Heliyon*, 2022, **8**, e11592.
211 N. Beattie, N. Bock, T. Anderson, T. Edgeworth, T. Kloss and J. Swanson, *J. Mater. Eng. Perform.*, 2021, **30**, 5059–5065.
212 S. R. Rajpurohit and H. K. Dave, *Rapid Prototyp. J.*, 2018, **24**, 1317–1324.
213 P. Czyżewski, D. Marciniak, B. Nowinka, M. Borowiak and M. Bieliński, *Polymers*, 2022, **14**, 356.
214 P. Ferretti, C. Leon-Cardenas, G. M. Santi, M. Sali, E. Ciotti, L. Frizziero, G. Donnici and A. Liverani, *Polymers*, 2021, **13**, 2190.
215 T. D. Ngo, A. Kashani, G. Imbalzano, K. T. Q. Nguyen and D. Hui, *Composites, Part B*, 2018, **143**, 172–196.
216 I. J. Solomon, P. Sevvel and J. Gunasekaran, *Mater. Today: Proc.*, 2021, **37**, 509–514.
217 M. Lalegani Dezaki and M. K. A. Mohd Ariffin, *Polymers*, 2020, **12**, 2792.
218 F. Aliberti, A. Sorrentino, B. Palmieri, L. Vertuccio, G. De Tommaso, R. Pantani, L. Guadagno and A. Martone, *Compos., Part C: Open Access*, 2024, **15**, 100527.
219 B. G. Çakan, *J. Mech. Sci. Technol.*, 2021, **35**, 3347–3353.

220 K. Benié, T. Barrière, V. Placet and A. Cherouat, *Addit. Manuf.*, 2023, **69**, 103538.
221 K. L. Snapp, A. E. Gongora and K. A. Brown, *J. Eng. Ind.*, 2021, **143**, 1–20.
222 S. F. Costa, F. M. Duarte and J. A. Covas, *Virtual Phys. Prototyp.*, 2015, **10**, 35–46.
223 A. El Moumen, M. Tarfaoui and K. Lafdi, *Int. J. Adv. Des. Manuf. Technol.*, 2019, **104**, 1661–1676.
224 Y. Zhou, T. Nyberg, G. Xiong and D. Liu, Temperature Analysis in the Fused Deposition Modeling Process, *2016 3rd International Conference on Information Science and Control Engineering (ICISCE)*, Beijing, China, 2016, pp. 678–682, DOI: **10.1109/ICISCE.2016.150**, **https://ieeexplore.ieee.org/document/7726247**.
225 F. Tamburrino, S. Graziosi and M. Bordegoni, *Virtual Phys. Prototyp.*, 2019, **14**, 316–332.
226 A. Das, E. L. Gilmer, S. Biria and M. J. Bortner, *ACS Appl. Polym. Mater.*, 2021, **3**, 1218–1249.
227 D. D. Phan, Z. R. Swain and M. E. Mackay, *J. Rheol.*, 2018, **62**, 1097–1107.
228 P. Beesetty, A. Kale, B. Patil and M. Doddamani, *Compos. Struct.*, 2020, **247**, 112442.
229 F. Ning, W. Cong, J. Qiu, J. Wei and S. Wang, *Composites, Part B*, 2015, **80**, 369–378.
230 D. Zhu, Y. Ren, G. Liao, S. Jiang, F. Liu, J. Guo and G. Xu, *J. Appl. Polym. Sci.*, 2017, **134**, 45332.
231 J. Deepak, H. Adarsha, R. Keshavamurthy and N. P. Ramkumar, *J. Inst. Eng. (India): Ser. D*, 2024, **105**, 425–437.
232 X. Wang, M. Jiang, Z. Zhou, J. Gou and D. Hui, *Composites, Part B*, 2017, **110**, 442–458.
233 P. Wang, B. Zou, S. Ding, C. Huang, Z. Shi, Y. Ma and P. Yao, *Composites, Part B*, 2020, **198**, 108175.
234 K. Yang, J. C. Grant, P. Lamey, A. Joshi-Imre, B. R. Lund, R. A. Smaldone and W. Voit, *Adv. Funct. Mater.*, 2017, **27**, 1700318.
235 H. K. Dave and S. T. Patel, *Introduction to Fused Deposition Modeling Based 3D Printing Process*, Springer International Publishing, 2021, pp. 1–21, DOI: **10.1007/978-3-030-68024-4_1**.
236 K. M. M. Billah, J. Heineman, P. Mhatre, A. Roschli, B. Post, V. Kumar, S. Kim, G. Haye, J. Jackson, Z. Skelton, V. Kunc and A. A. Hassen, *Addit. Manuf.*, 2021, **47**, 102282.
237 H. Pei, Y. Xie, Y. Xiong, Q. Lv and Y. Chen, *Composites, Part B*, 2021, **225**, 109312.
238 M. Karabal, R. Yuksel, F. Kayginok, A. Yildiz and H. Cebeci, Embedded Piezoresistive Sensors Printed by FFF for Aerospace Applications, in *AIAA SCITECH 2023 Forum*, 2023, p. 0318.
239 V. V. Shinde, G. Taylor, A.-D. N. Celestine and B. S. Beckingham, *ACS Appl. Polym. Mater.*, 2022, **4**, 3324–3332.
240 W. Ye, H. Dou, Y. Cheng and D. Zhang, *Mater. Lett.*, 2022, **317**, 132077.
241 C. Luan, X. Yao, C. Zhang, J. Fu and B. Wang, *Compos. Sci. Technol.*, 2020, **188**, 107986.
242 A. Kontiza and I. A. Kartsonakis, *Polymers*, 2024, **16**, 2115.
243 D. Carou, *Aerospace and digitalization: A transformation through key industry 4.0 technologies*, Springer Nature, 2021.
244 3D Printing and Space Exploration: How NASA Will Use Additive Manufacturing - Tech Briefs Available online: **https://www.techbriefs.com/component/content/article/35871-3d-printing-and-space-exploration-how-nasa-will-use-additive-manufacturing**.
245 Space Station 3-D Printer Builds Ratchet Wrench To Complete First Phase Of Operations - NASA Available online: **https://www.nasa.gov/missions/station/space-station-3-d-printer-builds-ratchet-wrench-to-complete-first-phase-of-operations/**.
246 F. Bourseau, S. Grugeon, U. Lafont and L. Dupont, *J. Phys.: Energy*, 2024, **6**, 012001.
247 A. Zocca, J. Wilbig, A. Waske, J. Günster, M. P. Widjaja, C. Neumann, M. Clozel, A. Meyer, J. Ding, Z. Zhou and X. Tian, *Chin. J. Mech. Eng.*, 2022, **1**, 100018.
248 K. A. Hamzah, C. K. Yeoh, M. M. Noor, P. L. Teh, Y. Y. Aw, S. A. Sazali and W. M. A. Wan Ibrahim, *J. Thermoplast. Compos. Mater.*, 2022, **35**, 3–16.
249 J. Mogan, L. Sandanamsamy, W. S. W. Harun, I. Ishak, F. R. M. Romlay, K. Kadirgama and D. Ramasamy, *Mater. Today: Proc.*, 2024, **109**, 120–125.
250 V. F. Moritz, H. Prévost, J. S. Crespo, C. A. Ferreira and D. M. Devine, *Designs*, 2023, **7**, 133.
251 M. Nabipour, B. Akhoundi and A. Bagheri Saed, *J. Appl. Polym. Sci.*, 2020, **137**, 48717.
252 O. Ulkir, *Rapid Prototyp. J.*, 2024, **30**, 2113–2122.
253 V. S. Vakharia, L. Kuentz, A. Salem, M. C. Halbig, J. A. Salem and M. Singh, *Polymers*, 2021, **13**, 3545.
254 A. Goulas, J. R. McGhee, T. Whittaker, D. Ossai, E. Mistry, W. Whittow, B. Vaidhyanathan, I. M. Reaney, J. C. Vardaxoglou and D. S. Engstrøm, *Addit. Manuf.*, 2022, **55**, 102844.
255 D. Froš and P. Veselý, Thermomechanical Assessment of Novel Composites Intended for Fused Deposition Modeling, 2022 45th International Spring Seminar on Electronics Technology (ISSE), Vienna, Austria, 2022, pp. 1–8, DOI: **10.1109/ISSE54558.2022.9812709**, **https://ieeexplore.ieee.org/document/9812709**.
256 P. Veselý, D. Froš, T. Hudec, J. Sedláček, P. Ctibor and K. Dušek, *Virtual Phys. Prototyp.*, 2023, **18**, e2170253.
257 D. Kodali, C. O. Umerah, M. O. Idrees, S. Jeelani and V. K. Rangari, *J. Compos. Mater.*, 2021, **55**, 4575–4584.
258 F. Calignano, M. Lorusso, I. Roppolo and P. Minetola, *Machines*, 2020, **8**, 52.
259 V. Durga Prasada Rao, P. Rajiv and V. Navya Geethika, *Mater. Today: Proc.*, 2019, **18**, 2012–2018.
260 A. Gupta, I. Fidan, S. Hasanov and A. Nasirov, *Int. J. Adv. Des. Manuf. Technol.*, 2020, **107**, 3185–3205.
261 E. Lobov, A. Dobrydneva, I. Vindokurov and M. Tashkinov, *Polymers*, 2023, **15**, 2011.
262 C. Pandelidi, S. Bateman, M. Maghe, S. Piegert and M. Brandt, *Prog. Addit. Manuf.*, 2022, **7**, 1093–1109.
263 S. Pei, K. Wang, C.-B. Chen, J. Li, Y. Li, D. Zeng, X. Su and H. Yang, *J. Manuf. Process.*, 2021, **64**, 544–556.

264 S. Pervaiz, T. A. Qureshi, G. Kashwani and S. Kannan, *Materials*, 2021, **14**, 4520.
265 W. Seok, E. Jeon and Y. Kim, *Polymers*, 2023, **15**, 3110.
266 T. Yap, N. Heathman, T. Phillips, J. Beaman and M. Tehrani, *Composites, Part B*, 2023, **266**, 111019.
267 M. Ateeq, M. Shafique, A. Azam and M. Rafiq, *J. Mater. Res. Technol.*, 2023, **26**, 2291–2309.
268 M. M. Garmabi, A. Jalali, A. Manzoor, R. Malik and M. Sain, *Prog. Addit. Manuf.*, 2025, **10**, 2397–2409.
269 N. Li, G. Link and J. Jelonnek, *Compos. Sci. Technol.*, 2020, **187**, 107939.
270 H. Zhang, A. Li, J. Wu and D. Yang, *Composites, Part B*, 2025, **298**, 112373.
271 Z. Zhang, Y. Long, Z. Yang, K. Fu and Y. Li, *Composites, Part A*, 2022, **162**, 107162.
272 P. Zhuo, S. Li, I. A. Ashcroft and I. A. Jones, *Compos. Sci. Technol.*, 2022, **221**, 109341.
273 A. Amiri, A. Zolfaghari and M. Shakeri, *Polym. Compos.*, 2022, **43**, 6287–6299.
274 K. Chen, L. Yu, Y. Cui, M. Jia and K. Pan, *Thin Wall Struct.*, 2021, **164**, 107717.
275 J. Saroia, Y. Wang, Q. Wei, M. Lei, X. Li, Y. Guo and K. Zhang, *Int. J. Adv. Des. Manuf. Technol.*, 2020, **106**, 1695–1721.
276 S. Antony, A. Cherouat and G. Montay, *Appl. Compos. Mater.*, 2020, **27**, 935–953.
277 D. Deb and J. M. Jafferson, *Mater. Today: Proc.*, 2021, **46**, 1308–1318.
278 C. H. Lee, F. N. B. M. Padzil, S. H. Lee, Z. M. A. A. Ainun and L. C. Abdullah, *Polymers*, 2021, **13**, 1407.
279 Kusmono and P. P. Aji, *AIP Conf. Proc.*, 2021, **2338**, 040024.
280 N. Vidakis, M. Petousis, E. Velidakis, M. Spiridaki and J. D. Kechagias, *Fibers*, 2021, **9**, 74.
281 Z. Zhang, W. Wang, Y. Li, K. Fu, X. Tong, B. Cao and B. Chen, *Composites Commun.*, 2023, **43**, 101731.
282 A. Moutsopoulou, M. Petousis, N. Michailidis, N. Mountakis, A. Argyros, V. Papadakis, M. Spiridaki, C. Charou, I. Ntintakis and N. Vidakis, *J. Compos. Sci.*, 2023, **7**, 393.
283 N. Vidakis, A. Moutsopoulou, M. Petousis, N. Michailidis, C. Charou, N. Mountakis, A. Argyros, V. Papadakis and E. Dimitriou, *Polymers*, 2023, **15**, 3883.
284 Y. Wu, Y. Cao, Y. Wu and D. Li, *Materials*, 2020, **13**, 4475.
285 R. C. Martins, S. P. D. S. Ribeiro, M. J. C. Rezende, R. S. V. Nascimento, M. A. C. Nascimento, M. Batistella and J.-M. Lopez-Cuesta, *Polymers*, 2022, **14**, 1702.
286 X. Luo, H. Cheng and X. Wu, *Polymers*, 2023, **15**, 2980.
287 S. S. Banerjee, S. Burbine, N. Kodihalli Shivaprakash and J. Mead, *Polymers*, 2019, **11**, 347.
288 H. Jeon, Y. Kim, W.-R. Yu and J. U. Lee, *Composites, Part B*, 2020, **189**, 107912.
289 Additive Manufacturing (3D Printing) Aircraft Parts and Tooling at the Maintenance Group Level Available online: **https://apps.dtic.mil/sti/citations/AD1054244**.
290 What Are SmallSats and CubeSats? - NASA Available online: **https://www.nasa.gov/what-are-smallsats-and-cubesats/**.
291 3D Printed Satellite Exterior | NASA Case Study | Stratasys Direct Available online: **https://www.stratasys.com/en/stratasysdirect/resources/case-studies/3d-printed-satellite-exterior-nasa-jet-propulsion-laboratory/**.
292 A. Kwas, E. MacDonald, D. Muse, R. Wicker, C. Kief, J. Aarestad, M. Zemba, B. Marshall, C. Tolbert and B. Connor, *Enabling Technologies for Entrepreneurial Opportunities in 3D printing of SmallSats, Report 20140011334*, NASA Glenn Research Center Cleveland, OH United States, 2014.
293 W. M. Marshall, J. D. Stegeman, M. Zemba, E. Macdonald, C. Shemelya, R. Wicker, A. Kwas and C. Kief, Using additive manufacturing to print a cubesat propulsion system, in *51st AIAA/SAE/ASEE Joint Propulsion Conference*, 2015, p. 4184.
294 M. Rinaldi, F. Cecchini, L. Pigliaru, T. Ghidini, F. Lumaca and F. Nanni, *Polymers*, 2020, **13**, 11.
295 K. C. Chuang, J. E. Grady, R. D. Draper, E.-S. E. Shin, C. Patterson and T. D. Santelle, *Additive Manufacturing and Characterization of Ultem Polymers and Composites, Report 20160001352*, NASA Glenn Research Center Cleveland, OH United States, 2015.
296 W. M. Marshall, M. Zemba, C. Shemelya, R. Wicker, D. Espalin, E. MacDonald and A. Kwas, *Using Additive Manufacturing to Print a CubeSat Propulsion System*, Glenn Research Center, 2015.
297 C. M. S. Vicente, M. Sardinha, L. Reis, A. Ribeiro and M. Leite, *Prog. Addit. Manuf.*, 2023, **8**, 1257–1280.
298 How 3D Printing Is Shaping the Future of Aircraft Maintenance, Repair & Overhaul - TCT Magazine Available online: **https://www.tctmagazine.com/additive-manufacturing-3d-printing-news/additive-manufacturing-aerospace-maintenance-repair/**.
299 V. Acanfora, A. Sellitto, A. Russo, M. Zarrelli and A. Riccio, *Aerosp. Sci. Technol.*, 2023, **137**, 108276.
300 E. Balasubramanian, N. V. S. S. Sagar, U. Chandrasekhar and S. Salunkhe, *Int. J. Mater. Prod. Technol.*, 2019, **59**, 229.
301 A. Sanchez Ramirez, M. E. Islán Marcos, F. Blaya Haro, R. D'Amato, R. Sant and J. Porras, *Rapid Prototyp. J.*, 2019, **25**, 781–791.
302 S. Brischetto, A. Ciano and C. G. Ferro, *Curved and Layered Structures*, 2016, vol. 3.
303 G. D. Goh, S. Agarwala, G. L. Goh, V. Dikshit, S. L. Sing and W. Y. Yeong, *Aerosp. Sci. Technol.*, 2017, **63**, 140–151.
304 H. Guo, R. Lv and S. Bai, *Nano Mater. Sci.*, 2019, **1**, 101–115.
305 J. Bonada, E. Xuriguera, L. Calvo, L. Poudelet, R. Cardona, J. A. Padilla, M. Niubó and F. Fenollosa, *Proc. Manuf.*, 2019, **41**, 666–673.
306 A. Haake, R. Tutika, G. M. Schloer, M. D. Bartlett and E. J. Markvicka, *Adv. Mater.*, 2022, **34**, 2200182.
307 M. A. S. R. Saadi, A. Maguire, N. T. Pottackal, M. S. H. Thakur, M. M. Ikram, A. J. Hart, P. M. Ajayan and M. M. Rahman, *Adv. Mater.*, 2022, **34**, 2108855.
308 H. Wang, C. Chen, F. Yang, Y. Shao and Z. Guo, *Mater. Today Commun.*, 2021, **26**, 102037.

309 I. Buj-Corral, A. Domínguez-Fernández and A. Gómez-Gejo, *Materials*, 2020, **13**, 2157.
310 L. Del-Mazo-Barbara and M.-P. Ginebra, *J. Eur. Ceram. Soc.*, 2021, **41**, 18–33.
311 J. A. Lewis, J. E. Smay, J. Stuecker and J. Cesarano, *J. Am. Ceram. Soc.*, 2006, **89**, 3599–3609.
312 A. M'Barki, L. r Bocquet and A. Stevenson, *Sci. Rep.*, 2017, 7.
313 A. Shahzad and I. Lazoglu, *Composites, Part B*, 2021, **225**, 109249.
314 S. B. Balani, S. H. Ghaffar, M. Chougan, E. Pei and E. Ăžahin, *Results Eng.*, 2022, **13**, 100308.
315 P. D'Angelo and D. Vurro, *Direct Writing: Inkjet and Aerosol-Jet Printing*, Springer International Publishing, 2022, pp. 105–129, DOI: 10.1007/978-3-031-13779-2_5.
316 G.-K. Lau and M. Shrestha, *Micromachines*, 2017, **8**, 194.
317 P. Cooley, D. Wallace and B. Antohe, *JALA*, 2002, **7**, 33–39.
318 J. Alamán, R. Alicante, J. Peña and C. Sánchez-Somolinos, *Materials*, 2016, **9**, 910.
319 J. A. Lewis, *Adv. Funct. Mater.*, 2006, **16**, 2193–2204.
320 P. Wei, H. Leng, Q. Chen, R. C. Advincula and E. B. Pentzer, *ACS Appl. Polym. Mater.*, 2019, **1**, 885–892.
321 R. L. Truby and J. A. Lewis, *Nature*, 2016, **540**, 371–378.
322 J. Mancilla-De-La-Cruz, M. Rodriguez-Salvador, J. An and C. K. Chua, *Int. J. Bioprint.*, 2022, **8**, 622.
323 S. Agarwala, G. L. Goh and W. Y. Yeong, *IOP Conf. Ser.: Mater. Sci. Eng.*, 2017, **191**, 012027.
324 A. Motealleh, S. Eqtesadi, A. Pajares and P. Miranda, *J. Mech. Behav. Biomed. Mater.*, 2018, **84**, 35–45.
325 T. Y. Ansell, *J. Manuf. Mater. Process.*, 2021, **5**, 31.
326 E. Shang, G. Li, Z. Zhao, N. Zhang, D. Fan and Y. Liu, *Adv. Mater. Interfaces*, 2023, 10.
327 M. A. Skylar-Scott, S. Gunasekaran and J. A. Lewis, *Proc. Natl. Acad. Sci. U. S. A.*, 2016, **113**, 6137–6142.
328 J. K. Wilt, D. Gilmer, S. Kim, B. G. Compton and T. Saito, *MRS Commun.*, 2021, **11**, 106–121.
329 G. Rivers, J. S. Austin, Y. He, A. Thompson, N. Gilani, N. Roberts, P. Zhao, C. J. Tuck, R. J. M. Hague, R. D. Wildman and L. Turyanska, *Addit. Manuf.*, 2023, **66**, 103452.
330 J. M. Hoey, A. Lutfurakhmanov, D. L. Schulz and I. S. Akhatov, *J. Nanotechnol.*, 2012, **2012**, 1–22.
331 S. Lamnini, H. Elsayed, Y. Lakhdar, F. Baino, F. Smeacetto and E. Bernardo, *Heliyon*, 2022, **8**, e10651.
332 T. V. Neumann and M. D. Dickey, *Adv. Mater. Technol.*, 2020, **5**, 2000070.
333 W. H. Herschel and R. Bulkley, *Kolloid-Z.*, 1926, **39**, 291–300.
334 J. Wang, Y. Liu, Z. Fan, W. Wang, B. Wang and Z. Guo, *Adv. Compos. Hybrid Mater.*, 2019, **2**, 1–33.
335 J. E. Fromm, *IBM J. Res. Dev.*, 1984, **28**, 322–333.
336 M. Kasraie, A. S. Krieg, A. C. Abbott, A. Gawde, T. C. Eisele, J. A. King, G. M. Odegard, J. W. Baur and P. Pour Shahid Saeed Abadi, *Composites, Part B*, 2024, **282**, 111583.
337 P. Wei, C. Cipriani, C.-M. Hsieh, K. Kamani, S. Rogers and E. Pentzer, *J. Appl. Phys.*, 2023, **134**, 100701.
338 A. Stiles, T.-A. Tison, L. Pruitt and U. Vaidya, *Polymers*, 2022, **14**, 2708.
339 J. Zhu, Q. Zhang, T. Yang, Y. Liu and R. Liu, *Nat. Commun.*, 2020, **11**, 3462.
340 R. Raj and A. R. Dixit, *3D Print. Addit. Manuf.*, 2023, **10**, 828–854.
341 J. M. Löwe, J. Plog, Y. Jiang, Y. Pan and A. L. Yarin, *J. Appl. Phys.*, 2019, **126**, 035302.
342 L. Friedrich and M. Begley, *J. Colloid Interface Sci.*, 2018, **529**, 599–609.
343 C. Li, C. Feng, L. Zhang, L. Zhang and L. Wang, *Polym. Eng. Sci.*, 2025, **65**, 431–454.
344 J. R. C. Dizon, C. C. L. Gache, H. M. S. Cascolan, L. T. Cancino and R. C. Advincula, *Technologies*, 2021, **9**, 61.
345 K. T. Estelle and B. A. Gozen, *Addit. Manuf.*, 2022, **59**, 103183.
346 Q. Zheng, B. Xie, Z. Xu and H. Wu, *Int. J. Extreme Manuf.*, 2023, **5**, 035002.
347 F. Jiang, A. Wörz, M. Romeis and D. Drummer, *Polym. Test.*, 2022, **105**, 107428.
348 Z.-L. Wu, Y.-N. Qi, X.-J. Yin, X. Yang, C.-M. Chen, J.-Y. Yu, J.-C. Yu, Y.-M. Lin, F. Hui, P.-L. Liu, Y.-X. Liang, Y. Zhang and M.-S. Zhao, *Polymers*, 2019, **11**, 553.
349 Y. Tu, J. A. Arrieta-Escobar, A. Hassan, U. K. U. Zaman, A. Siadat and G. Yang, *3D Print. Addit. Manuf.*, 2023, **10**, 816–827.
350 X. Zhang, X. Jia and X. Wang, *Direct ink writing of polymers and their composites, and related applications*, Elsevier, 2020, pp. 391–408, DOI: 10.1016/b978-0-12-819535-2.00013-2.
351 L. Li, Q. Lin, M. Tang, A. J. E. Duncan and C. Ke, *Chem. – Eur. J.*, 2019, **25**, 10768–10781.
352 A. White, I. Little, A. Artyuk, N. McKibben, F. Rajabi Kouchi, C. Chen, D. Estrada and Z. Deng, *Smart Mater. Struct.*, 2024, **33**, 055053.
353 K. Gao, J. Gong, P. Cao, Z. Tang, T. Wang, L. Tao, X. Zhang, J. Zhang, Q. Wang and Y. Zhang, *ACS Appl. Polym. Mater.*, 2023, **5**, 8833–8844.
354 C. Duan, F. Long, X. Shi, Y. Wang, J. Dong, S. Ying, Y. Li, Y. Cheng, J. Guo, G. Xu and A. Sun, *Micromachines*, 2023, **14**, 815.
355 M. Abshirini, P. Marashizadeh, M. C. Saha, M. C. Altan and Y. Liu, *ACS Appl. Mater. Interfaces*, 2023, **15**(11), 14810–14825.
356 M. Charara, M. Abshirini, M. C. Saha, M. C. Altan and Y. Liu, *J. Intell. Mater. Syst. Struct.*, 2019, **30**, 1216–1224.
357 M. G. Rasul, M. Cheng, Y. Jiang, Y. Pan and R. Shahbazian-Yassar, *ACS Nanoscience Au*, 2022, **2**, 297–306.
358 S. J. Talley, B. Branch, C. F. Welch, C. H. Park, J. Watt, L. Kuettner, B. Patterson, D. M. Dattelbaum and K.-S. Lee, *Compos. Sci. Technol.*, 2020, **198**, 108258.
359 T. Xiao, C. Qian, R. Yin, K. Wang, Y. Gao and F. Xuan, *Adv. Mater. Technol.*, 2021, **6**, 2000745.
360 J. Liu, L. McKeon, J. Garcia, S. Pinilla, S. Barwich, M. Möbius, P. Stamenov, J. N. Coleman and V. Nicolosi, *Adv. Mater.*, 2022, **34**, 2106253.

361 Z. Yang, E. Medora, Z. Ren, M. Cheng, S. Namilae and Y. Jiang, *Compos. Sci. Technol.*, 2024, **256**, 110782.
362 H. Liu, D. Mei, S. Yu, S. Qian and Y. Wang, *J. Eur. Ceram. Soc.*, 2023, **43**, 235–244.
363 N. Nawafleh, F. K. E. Elibol, M. Aljaghtham, E. Oflaz, A. J. Ciciriello, C. M. Dumont, E. Dauer, R. M. Gorguluarslan, T. Demir and E. Celik, *J. Mater. Sci.*, 2020, **55**, 11284–11295.
364 C. Yang, E. Zhou, S. Miyanishi, K. Hashimoto and K. Tajima, *ACS Appl. Mater. Interfaces*, 2011, **3**, 4053–4058.
365 A. Pique and D. B. Chrisey, *Direct-write technologies for rapid prototyping applications: sensors, electronics, and integrated power sources*, Academic press, 2002.
366 3D Printed Polymer Aerogels | T2 Portal Available online: **https://technology.nasa.gov/patent/LEW-TOPS-171**.
367 C. Lin, X. Jia, C. Chen, C. Yang, X. Li, M. Shao, Y. Yu and Z. Zhang, *Opt. Express*, 2023, **31**, 11913.
368 C. C. Ho, J. W. Evans and P. K. Wright, Direct-write dispenser-printed energy storage devices, in *Micro-and Nanotechnology Sensors, Systems, and Applications II*, SPIE, 2020, vol. 7679, pp. 583–591, DOI: **10.1117/12.850561**.
369 S. Raja, *PhD Thesis*, Loughborough University, 2014.
370 H. He, M. Akbari, L. Sydänheimo, L. Ukkonen and J. Virkki, *Int. J. Antennas Propag.*, 2017, **2017**, 1–5.
371 E. Demirkal, K. Sierros, D. Banerjee, J. Burke, K. Sabolsky and E. Sabolsky, *ECS Meeting Abstracts*, 2023, **MA2023-01**, 2723.
372 NASA TechPort - Project Data Available online: **https://techport.nasa.gov/view/102205**.
373 A. Marnot, L. Konzelman, J. M. Jones, C. Hill and B. Brettmann, *ACS Appl. Mater. Interfaces*, 2023, **15**, 50378–50390.
374 J. Huang, Q. Qin and J. Wang, *Processes*, 2020, **8**, 1138.
375 J. Huang, Q. Qin, J. Wang and F. Hui, *Int. J. Mater., Mech. Manuf.*, 2018, **6**, 332–336.
376 A. Bertsch, S. Zissi, J. Y. Jezequel, S. Corbel and J. C. Andre, *Microsyst. Technol.*, 1997, **3**, 42–47.
377 K. Hane and M. Sasaki, *Micro-Mirrors*, Elsevier, 2008, pp. 1–63, DOI: **10.1016/b978-044452190-3.00032-x**.
378 J. R. Tumbleston, D. Shirvanyants, N. Ermoshkin, R. Janusziewicz, A. R. Johnson, D. Kelly, K. Chen, R. Pinschmidt, J. P. Rolland, A. Ermoshkin, E. T. Samulski and J. M. Desimone, *Science*, 2015, **347**, 1349–1352.
379 L. Stüwe, M. Geiger, F. Röllgen, T. Heinze, M. Reuter, M. Wessling, S. Hecht and J. Linkhorst, *Adv. Mater.*, 2024, **36**, 2306716.
380 B. E. Kelly, I. Bhattacharya, H. Heidari, M. Shusteff, C. M. Spadaccini and H. K. Taylor, *Science*, 2019, **363**, 1075–1079.
381 Z. Huang, G. Chi-Pong Tsui, Y. Deng and C.-Y. Tang, *Nanotechnol. Rev.*, 2020, **9**, 1118–1136.
382 I. Boudene and Y. Bougdid, *J. Mater. Chem. C*, 2025, **13**, 18597–18630.
383 H. Cho, W.-S. Lee and W. S. Chang, *JMST Adv.*, 2024, **6**, 371–377.
384 Y. Mao, T. Miyazaki, K. Sakai, J. Gong, M. Zhu and H. Ito, *Polymers*, 2018, **10**, 1117.
385 J. Z. Manapat, Q. Chen, P. Ye and R. C. Advincula, *Macromol. Mater. Eng.*, 2017, **302**, 1600553.
386 S. Zakeri, M. Vippola and E. Levänen, *Addit. Manuf.*, 2020, **35**, 101177.
387 N. D. Borra and V. S. N. Neigapula, *Rapid Prototyp. J.*, 2023, **29**, 166–184.
388 A. Kafle, E. Luis, R. Silwal, H. M. Pan, P. L. Shrestha and A. K. Bastola, *Polymers*, 2021, **13**, 3101.
389 V. S. D. Voet, J. Guit and K. Loos, *Macromol. Rapid Commun.*, 2021, **42**, 2000475.
390 G. Zhu, H. A. Houck, C. A. Spiegel, C. Selhuber-Unkel, Y. Hou and E. Blasco, *Adv. Funct. Mater.*, 2024, **34**, 2300456.
391 V. Bijalwan, S. Rana, G. J. Yun, K. P. Singh, M. Jamil and S. Schlögl, *Polym. Rev.*, 2024, **64**, 36–79.
392 S. Pruksawan, Y. T. Chong, W. Zen, T. J. E. Loh and F. Wang, *Chem. Asian J.*, 2024, **19**, e202400183.
393 O. W. Saadi and K. A. Khan, *Virtual Phys. Prototyp.*, 2025, 20.
394 Z. Zhang, N. Corrigan and C. Boyer, *Angew. Chem.*, 2022, 134.
395 H. Kim, L. C. D. Manriquez, M. T. Islam, L. A. Chavez, J. E. Regis, M. A. Ahsan, J. C. Noveron, T.-L. B. Tseng and Y. Lin, *MRS Commun.*, 2019, **9**, 1115–1123.
396 L. Wang, Y. Ma, K. Wang, Y. Ma, K. Wang, B. Lu, L. Niu and X. Li, *Sens. Actuators, A*, 2023, **362**, 114586.
397 M. M. Bazyar, S. A. A. B. Tabary, D. Rahmatabdi, K. Mohammadi and R. Hashemi, *J. Manuf. Process.*, 2023, **103**, 136–143.
398 M. Shah, A. Ullah, K. Azher, A. Ur Rehman, N. Akturk, W. Juan, C. S. Tüfekci and M. U. Salamci, *Crystals*, 2023, **13**, 285.
399 D. Kokkinis, M. Schaffner and A. R. Studart, *Nat. Commun.*, 2015, **6**, 8643.
400 L. Lu, E. Baynojir Joyee and Y. Pan, *J. Micro Nano-Manuf.*, 2018, **6**, 010904.
401 L. Lu, P. Guo and Y. Pan, *J. Eng. Ind.*, 2017, **139**, 071008.
402 Y. Yang, Z. Chen, X. Song, Z. Zhang, J. Zhang, K. K. Shung, Q. Zhou and Y. Chen, *Adv. Mater.*, 2017, **29**, 1605750.
403 L. Lu, X. Tang, S. Hu and Y. Pan, *3D Print. Addit. Manuf.*, 2018, **5**, 151–159.
404 K. Markandan and C. Q. Lai, *Composites, Part B*, 2023, **256**, 110661.
405 Y. Yang, X. Li, M. Chu, H. Sun, J. Jin, K. Yu, Q. Wang, Q. Zhou and Y. Chen, *Sci. Adv.*, 2019, **5**, eaau9490.
406 Y. Sano, R. Matsuzaki, M. Ueda, A. Todoroki and Y. Hirano, *Addit. Manuf.*, 2018, **24**, 521–527.
407 Z. Miller, B. Stidham, T. Fairbanks and C. Maldonado, The Use of Stereolithography (SLA) Additive Manufacturing in Space-Based Instrumentation, *2023 IEEE Aerospace Conference*, Big Sky, MT, USA, 2023, pp. 1–10, DOI: **10.1109/AERO55745.2023.10115988**, **https://ieeexplore.ieee.org/document/10115988**.
408 NASA TechPort - Project Data Available online: **https://techport.nasa.gov/view/146082**.
409 T. Sheri and M. Matthew, *Characterization and Testing of Copper-Nickel Electroplated 3D Printed Parts for Space Flight Applications*, Goddard Space Flight Center Greenbelt, Maryland, United States, 2023.

410 https://3dprint.com/98377/utep-america-makes-grant/.
411 E. Macdonald, R. Salas, D. Espalin, M. Perez, E. Aguilera, D. Muse and R. B. Wicker, *IEEE Access*, 2014, **2**, 234–242.
412 M. T. Getachew, M. Z. Shiferaw and B. S. Ayele, *Adv. Mater. Sci. Eng.*, 2023, **2023**, 1–13.
413 T. Waddell, J. Toombs, A. Reilly, T. Schwab, C. Castaneda, I. Shan, T. Lewis, P. Mohnot, D. Potter and H. Taylor, *Acta Astronaut.*, 2023, **211**, 474–482.
414 PolyJet Technology for 3D Printing | Stratasys Available online: https://www.stratasys.com/en/guide-to-3d-printing/technologies-and-materials/polyjet-technology/.
415 J. Sanders, X. Wei and Z. Pei, Experimental investigation of polyjet 3D printing process: Effects of orientation and layer thickness on thermal glass transition temperature, in *ASME International Mechanical Engineering Congress and Exposition*, American Society of Mechanical Engineers, 2019, vol. 59377, p. V02AT02A064.
416 A. Pugalendhi, R. Ranganathan and M. Chandrasekaran, *Int. J. Adv. Des. Manuf. Technol.*, 2020, **108**, 1049–1059.
417 N. A. Meisel and C. B. Williams, Design for additive manufacturing: An investigation of key manufacturing considerations in multi-material polyjet 3D printing, in *25th Annual International Solid Freeform Fabrication Symposium An Additive Manufacturing Conference*, SFF 2014, 2014.
418 N. Muthuram, P. Sriram Madhav, D. Keerthi Vasan, M. E. Mohan and G. Prajeeth, *Mater. Today: Proc.*, 2022, **68**, 1906–1920.
419 F. I. Ulu and R. V. Mohan, *Prog. Addit. Manuf.*, 2021, **6**, 653–662.
420 C. Bader, D. Kolb, J. C. Weaver, S. Sharma, A. Hosny, J. O. Costa and N. Oxman, *Sci. Adv.*, 2018, **4**, eaas8652.
421 E. L. Doubrovski, E. Y. Tsai, D. Dikovsky, J. M. P. Geraedts, H. Herr and N. Oxman, *Comput.-Aided Des.*, 2015, **60**, 3–13.
422 Illusory Material: Reimagining Product Design with Multi-Material 3D Printing | VoxelMatters - The Heart of Additive Manufacturing Available online: https://www.voxelmatters.com/illusory-material-multi-material-3d-printing/.
423 X. Wei, N. Zou, L. Zeng and Z. Pei, *Ann. 3D Print. Med.*, 2022, **5**, 100049.
424 P. J. Bartolo, Innovative Developments in Virtual and Physical Prototyping: Proceedings of the 5th International Conference on Advanced Research in Virtual and Rapid Prototyping, Leiria, Portugal, CRC Press, 28 September–1 October, 2011.
425 L. B. Bezek and C. B. Williams, *Addit. Manuf.*, 2023, **73**, 103640.
426 X. Chen, I. A. Ashcroft, R. D. Wildman and C. J. Tuck, *Proc. R. Soc. A*, 2015, **471**, 20150477.
427 P. Gay, D. Blanco, F. Pelayo, A. Noriega and P. Fernandez, *Proc. Eng.*, 2015, **132**, 70–77.
428 O. Gülcan, K. Günaydin and A. Tamer, *Polymers*, 2021, **13**, 2829.
429 H. Kim, Y. Lin and T.-L. B. Tseng, *Rapid Prototyp. J.*, 2018, **24**, 645–669.
430 V. Rajendra Boopathy, A. Sriraman and G. Arumaikkannu, *Rapid Prototyp. J.*, 2019, **25**, 623–629.
431 C. Palanisamy, R. Raman and P. K. Dhanraj, *Polym. Bull.*, 2022, **79**, 7065–7116.
432 O. Gülcan, K. Günaydın and A. Çelik, *Aerospace*, 2022, **9**, 82.
433 A. Pugalendhi and R. Ranganathan, *Examining the Build Properties of PolyJet Printed Multi-material Parts in Additive Manufacturing*, Springer, Singapore, 2022, pp. 11–18, DOI: 10.1007/978-981-16-4222-7_2.
434 R. Udroiu, *Polymers*, 2022, **14**, 371.
435 Y. L. Yap, C. Wang, S. L. Sing, V. Dikshit, W. Y. Yeong and J. Wei, *Precis. Eng.*, 2017, **50**, 275–285.
436 F. Liu, T. Li, X. Jiang, Z. Jia, Z. Xu and L. Wang, *Addit. Manuf.*, 2020, **36**, 101502.
437 V. Slesarenko and S. Rudykh, *Int. J. Eng. Sci.*, 2018, **123**, 62–72.
438 C. Ge, D. Cormier and B. Rice, *J. Cell. Plast.*, 2021, **57**, 517–534.
439 P. Patpatiya, K. Chaudhary, A. Shastri and S. Sharma, *Proc. Inst. Mech. Eng., Part C*, 2022, **236**, 7899–7926.
440 Y. L. Tee, C. Peng, P. Pille, M. Leary and P. Tran, *JOM*, 2020, **72**, 1105–1117.
441 E. Salcedo, D. Baek, A. Berndt and J. E. Ryu, *Addit. Manuf.*, 2018, **22**, 351–359.
442 M. Sugavaneswaran and G. Arumaikkannu, *Mater. Des.*, 2015, **66**, 29–36.
443 G. Chen, Y. Li, P. He, Y. Wei, J. Song, B. Peng and Y. Li, *Addit. Manuf.*, 2025, **100**, 104698.
444 M. Nachimuthu and P. K. Rajesh, *Rapid Prototyp. J.*, 2023, **29**, 437–446.
445 S. K. Moon, Y. E. Tan, J. Hwang and Y.-J. Yoon, *Int. J. Pr. Eng. Manuf.-GT*, 2014, **1**, 223–228.
446 Aeronautical by Benedict Redgrove Available online: https://trendland.com/aeronautical-by-benedict-redgrove/.
447 H. Salem, D. Boutchicha and A. Boudjemai, *Int. J. Interact. Des. Manuf.*, 2018, **12**, 955–967.
448 C. Reinders, Reducing production costs of E-mobility components by using polyjet 3D printing, in *56th AIAA/ASCE/AHS/ASC Structures, Structural Dynamics, and Materials Conference*, 2015, p. 1357.
449 W. Han, L. Kong and M. Xu, *Int. J. Extreme Manuf.*, 2022, **4**, 042002.
450 F. Lupone, E. Padovano, F. Casamento and C. Badini, *Materials*, 2021, **15**, 183.
451 R. Brighenti, M. P. Cosma, L. Marsavina, A. Spagnoli and M. Terzano, *J. Mater. Sci.*, 2021, **56**, 961–998.
452 F. Yang, N. Zobeiry, R. Mamidala and X. Chen, *Mater. Today Commun.*, 2023, **34**, 105279.
453 A. C. Lopes, A. M. Sampaio, C. T. S. Silva and A. N. J. Pontes, *Rapid Prototyp. J.*, 2021, **27**, 496–506.
454 P. C. Gomes, O. G. Piñeiro, A. C. Alves and O. S. Carneiro, *Materials*, 2022, **15**, 5486.
455 L. Wang, A. Kiziltas, D. F. Mielewski, E. C. Lee and D. J. Gardner, *J. Cleaner Prod.*, 2018, **195**, 765–772.
456 M. Uddin, D. Williams and A. Blencowe, *Polymers*, 2021, **13**, 2046.

457 O. Kaba, A. T. Shah, D. Dudaško, N. Jain, T. Bertz, O. Görke and A. Gurlo, *Polym. Compos.*, 2025, **46**, 5964–5981.
458 J. P. Kruth, P. Mercelis, J. Van Vaerenbergh, L. Froyen and M. Rombouts, *Rapid Prototyp. J.*, 2005, **11**, 26–36.
459 M. Schmid, A. Amado and K. Wegener, *AIP Conf. Proc.*, 2015, **1664**, 160009.
460 S. Greiner, K. Wudy, L. Lanzl and D. Drummer, *Polym. Test.*, 2017, **64**, 136–144.
461 D. Drummer, K. Wudy, F. Kühnlein and M. Drexler, *Phys. Proc.*, 2012, **39**, 509–517.
462 L. Dong, A. Makradi, S. Ahzi, Y. Remond and X. Sun, *Polym. Sci., Ser. A*, 2008, **50**, 704–709.
463 A. Mokrane, M. H. Boutaous and S. Xin, *C. R. Mec.*, 2018, **346**, 1087–1103.
464 F. Shen, S. Yuan, C. K. Chua and K. Zhou, *J. Mater. Process. Technol.*, 2018, **254**, 52–59.
465 F. Shen, W. Zhu, K. Zhou and L.-L. Ke, *Acta Mech.*, 2021, **232**, 3635–3653.
466 G. R. Esposito, T. J. Dingemans and R. A. Pearson, *Addit. Manuf.*, 2021, **48**, 102445.
467 N. Lammens, M. Kersemans, I. De Baere and W. Van Paepegem, *Polym. Test.*, 2017, **57**, 149–155.
468 M. R. Omar, M. I. H. C. Abdullah, M. R. Alkahar, R. Abdullah, M. F. Abdollah, M. Subramaniam and R. S. Ibramsa, *J. Mech. Eng.*, 2022, **19**, 57–70.
469 H. C. H. Ho, W. L. Cheung and I. Gibson, *Ind. Eng. Chem. Res.*, 2003, **42**, 1850–1862.
470 X. H. Song, Y. S. Shi, P. H. Song, Q. S. Wei and W. Li, *Adv. Mater. Res.*, 2014, **915–916**, 1000–1004.
471 Z. Bashir, H. Gu and L. Yang, *Polym. Eng. Sci.*, 2018, **58**, 1888–1900.
472 H. Gu, F. Alfayez, T. Ahmed and Z. Bashir, *Polymers*, 2019, **11**, 2041.
473 D. Pezold, M. Wimmer, F. Alfayez, Z. Bashir and F. Döpper, *Polymers*, 2022, **14**, 2095.
474 S. Berretta, K. E. Evans and O. Ghita, *Eur. Polym. J.*, 2015, **68**, 243–266.
475 P. Chen, H. Cai, Z. Li, M. Li, H. Wu, J. Su, S. Wen, Y. Zhou, J. Liu, C. Wang, C. Yan and Y. Shi, *Addit. Manuf.*, 2020, **36**, 101615.
476 Y. Guo, H. Chen, S. Tian, Y. Xu, K. Ma, S. Ma, X. Wang, Y. Zhang and Y. Sun, *Virtual Phys. Prototyp.*, 2023, **18**, e2273298.
477 T. J. Hoskins, K. D. Dearn and S. N. Kukureka, *Polym. Test.*, 2018, **70**, 511–519.
478 A. Patel, V. Venoor, F. Yang, X. Chen and M. J. Sobkowicz, *Polym. Degrad. Stab.*, 2021, **185**, 109502.
479 J. T. Rimell and P. M. Marquis, *J. Biomed. Mater. Res.*, 2000, **53**, 414–420.
480 G. V. Salmoria, C. H. Ahrens, P. Klauss, R. A. Paggi, R. G. Oliveira and A. Lago, *Mater. Res.*, 2007, **10**, 211–214.
481 S. K. Tiwari, S. Pande, S. Agrawal and S. M. Bobade, *Rapid Prototyp. J.*, 2015, **21**, 630–648.
482 X. Zhu and Q. Yang, *Plast., Rubber Compos.*, 2020, **49**, 116–126.
483 L. J. Tan, W. Zhu, K. Sagar and K. Zhou, *Addit. Manuf.*, 2021, **37**, 101610.
484 X. Wang, Z. Wang, S. Xiang, M. Peng, G. Li and Y. Huang, *Addit. Manuf.*, 2024, **86**, 104188.
485 W. Zhu, C. Yan, Y. Shi, S. Wen, C. Han, C. Cai, J. Liu and Y. Shi, *Rapid Prototyp. J.*, 2016, **22**, 621–629.
486 S. Khazaee, A. Kiani, M. Badrossamay and E. Foroozmehr, *J. Mater. Eng. Perform.*, 2021, **30**, 3068–3078.
487 D. Strobbe, S. Dadbakhsh, L. Verbelen, P. Van Puyvelde and J.-P. Kruth, *Plast., Rubber Compos.*, 2018, **47**, 2–8.
488 Z. Zeng, X. Deng, J. Cui, H. Jiang, S. Yan and B. Peng, *Polymers*, 2019, **11**, 956.
489 K. Bharaj, S. Paul, K. A. Mumtaz, M. Chisholm and N. Hopkinson, *Proc. Inst. Mech. Eng., Part B*, 2020, **234**, 118–125.
490 Q. G. Chen and J. C. Zhang, *Adv. Mater. Res.*, 2011, **314–316**, 738–741.
491 C. Jibing, C. Junsheng, Y. Junsheng and W. Yiping, *Iran. Polym. J.*, 2023, **32**, 1537–1550.
492 K. Plummer, M. Vasquez, C. Majewski and N. Hopkinson, *Proc. Inst. Mech. Eng., Part B*, 2012, **226**, 1127–1135.
493 M. M. Rahman, K. A. Ahmed, M. Karim, J. Hassan, R. Roy, B. Bustami, S. M. N. Alam and H. Younes, *J. Manuf. Mater. Process.*, 2023, **7**, 144.
494 F. Shen, S. Yuan, Y. Guo, B. Zhao, J. Bai, M. Qwamizadeh, C. K. Chua, J. Wei and K. Zhou, *Int. J. Appl. Mech.*, 2016, **08**, 1640006.
495 L. Verbelen, S. Dadbakhsh, M. Van Den Eynde, D. Strobbe, J.-P. Kruth, B. Goderis and P. Van Puyvelde, *Addit. Manuf.*, 2017, **15**, 12–19.
496 Y. Zhuang, Y. Guo, J. Li, K. Jiang, Y. Yu, H. Zhang and D. Liu, *RSC Adv.*, 2020, **10**, 23644–23652.
497 Y. Lv, W. Thomas, R. Chalk, A. Hewitt and S. Singamneni, *J. Mater. Res.*, 2020, **35**, 3222–3234.
498 B. O. Sivadas, I. Ashcroft, A. N. Khlobystov and R. D. Goodridge, *Adv. Ind. Eng. Polym. Res.*, 2021, **4**, 277–300.
499 S. Yuan, Y. Zheng, C. K. Chua, Q. Yan and K. Zhou, *Composites, Part A*, 2018, **105**, 203–213.
500 L. A. Chavez, P. Ibave, M. S. Hassan, S. E. Hall-Sanchez, K. M. M. Billah, A. Leyva, C. Marquez, D. Espalin, S. Torres, T. Robison and Y. Lin, *J. Appl. Polym. Sci.*, 2022, **139**, 52290.
501 G. V. Salmoria, V. R. Lauth, M. R. Cardenuto and R. F. Magnago, *Opt. Laser Technol.*, 2018, **98**, 92–96.
502 M. Batistella, A. Regazzi, M. F. Pucci, J.-M. Lopez-Cuesta, O. Kadri, D. Bordeaux and F. Ayme, *Polym. Degrad. Stab.*, 2020, **181**, 109318.
503 X. Gan, G. Fei, J. Wang, Z. Wang, M. Lavorgna and H. Xia, Powder quality and electrical conductivity of selective laser sintered polymer composite components, in *Structure and Properties of Additive Manufactured Polymer Components*, Woodhead Publishing, 2020, pp. 149–185.
504 S. Xi, P. Zhang, Y. Huang, M. Kong, Q. Yang and G. Li, *Polymer*, 2020, **186**, 122044.
505 X. Tian, G. Peng, M. Yan, S. He and R. Yao, *Int. J. Heat Mass Transfer*, 2018, **120**, 379–386.

506 M. U. Azam, I. Belyamani, A. Schiffer, S. Kumar and K. Askar, *J. Mater. Res. Technol.*, 2024, **30**, 9625–9646.
507 M. U. Azam, S. Kumar and A. Schiffer, *Compos., Part C: Open Access*, 2025, **16**, 100566.
508 X. Li, H. Ouyang, S. Sun, J. Wang, G. Fei and H. Xia, *ACS Appl. Polym. Mater.*, 2023, **5**, 2944–2955.
509 Y. Wang, D. Rouholamin, R. Davies and O. R. Ghita, *Mater. Des.*, 2015, **88**, 1310–1320.
510 X. Du, Y. Liu, W. Zhao, L. Fan, S. Mo, L. Zhai, M. He, D. Peng, Q. Mou and G. Wang, *Composites, Part B*, 2025, **298**, 112394.
511 K. C. Chuang, T. Gornet and H. Koerner, *Challenges in Laser Sintering of Melt-Processable Thermoset Imide Resin*, NASA Glenn Research Center Cleveland, OH United States, 2016.
512 K. C. Chuang, T. J. Gornet, K. Schneidau and H. Koerner, *Laser Sintering of Thermoset Polyimide Composites*, NASA Glenn Research Center Cleveland, OH, United States, 2019.
513 M. S. Hassan, K. M. M. Billah, S. E. Hall, S. Sepulveda, J. E. Regis, C. Marquez, S. Cordova, J. Whitaker, T. Robison, J. Keating, E. Shafirovich and Y. Lin, *J. Compos. Sci.*, 2022, **6**, 41.
514 B. Ding, Y. Zhang, J. Wang, S. Mei, X. Chen, S. Li, W. Zhao, X. Zhang, G. Shi, Y. He, Z. Cui, P. Fu, X. Pang and M. Liu, *Composites Commun.*, 2022, **35**, 101280.
515 H. Chung and S. Das, *Mater. Sci. Eng. A*, 2006, **437**, 226–234.
516 S. Kseniya, T. Mikhail, G. Maksim, G. Alexander, K. Alina, R. Natalia, K. Azamat, R. Maxim, C. Igor and M. Valery, *Composites, Part A*, 2025, **193**, 108829.
517 F. Qi, N. Chen and Q. Wang, *Mater. Des.*, 2017, **131**, 135–143.
518 T. Wu, Y. Ren, L. Liang, J. Wen, H. Wu, Y. Tian, W. S. Tey and K. Zhou, *Virtual Phys. Prototyp.*, 2023, **18**, e2150652.
519 S. Song, Y. Li, Q. Wang and C. Zhang, *Composites, Part A*, 2021, **147**, 106452.
520 X. Zhang, W. Wu, T. Zhao and J. Li, *J. Appl. Polym. Sci.*, 2022, **139**, e53051.
521 G. Rollo, A. Ronca, P. Cerruti, X. P. Gan, G. Fei, H. Xia, G. Gorokhov, D. Bychanok, P. Kuzhir, M. Lavorgna and L. Ambrosio, *Polymers*, 2020, **12**, 1841.
522 H. M. Yehia, A. Hamada, T. A. Sebaey and W. Abd-Elaziem, *J. Manuf. Mater. Process.*, 2024, **8**, 197.
523 B. Caulfield, P. E. McHugh and S. Lohfeld, *J. Mater. Process. Technol.*, 2007, **182**, 477–488.
524 A. El Magri, S. E. Bencaid, H. R. Vanaei and S. B. Vaudreuil, *Polymers*, 2022, **14**, 3674.
525 M. Li, Y. Han, M. Zhou, P. Chen, H. Gao, Y. Zhang and H. Zhou, *J. Manuf. Process.*, 2020, **56**, 271–279.
526 F. Lupone, E. Padovano, M. Pietroluongo, S. Giudice, O. Ostrovskaya and C. Badini, *eXPRESS Polym. Lett.*, 2021, **15**, 177–192.
527 M. K. Razaviye, R. A. Tafti and M. Khajehmohammadi, *J. Adv. Manuf. Sci. Technol.*, 2022, **38**, 760–768.
528 C. A. Chatham, T. E. Long and C. B. Williams, *Prog. Polym. Sci.*, 2019, **93**, 68–95.
529 H. Chen, W. Zhu, H. Tang and W. Yan, *Int. J. Mach. Tool Manuf.*, 2021, **163**, 103703.
530 S. Yuan, J. Bai, C. Chua, J. Wei and K. Zhou, *Polymers*, 2016, **8**, 370.
531 GKN Aerospace's Additively Manufactured Winglet Available online: **https://www.materialise.com/en/inspiration/cases/gkn-aerospace-additive-manufacturing-winglet**.
532 Boeing Sees Growing Value & Versatility in SLS System and DuraForm Materials Available online: **https://www.3dsystems.com/learning-center/case-studies/boeing-sees-growing-value-versatility-sls-system-and-duraform-materials**.
533 R. B. Booth, B. C. Thornton, D. L. Vanelli and M. L. Gardiner, *US Pat.*, 8236418, 2012.
534 3D Printed 737 UAV Takes Flight - 3D Insider Available online: **https://3dinsider.com/3d-printed-737-uav-takes-flight/**.
535 D. E. Mouzakis, *Advanced technologies in manufacturing 3D-layered structures for defense and aerospace*, Lamination-theory and application, 2018.
536 FDM 3D Printing - Fused Deposition Modeling Available online: **https://www.stratasys.com/en/guide-to-3d-printing/technologies-and-materials/fdm-technology/**.
537 Tolerances & Accuracy in 3D Printing Technologies | Xometry Pro Available online: **https://xometry.pro/en-eu/articles/3d-printing-tolerances/**.
538 D. C. Sandeep, *Int. J. Latest Trends Eng. Technol.*, 2017, **8**, 264–272.
539 R. Liu, Z. Wang, T. Sparks, F. Liou and J. Newkirk, Aerospace applications of laser additive manufacturing, in *Laser additive manufacturing*, Woodhead Publishing, 2017, pp. 351–371.
540 A. Y. N. Sofla, S. A. Meguid, K. T. Tan and W. K. Yeo, *Mater. Des.*, 2010, **31**, 1284–1292.
541 K. Engel, P. A. Kilmartin and O. Diegel, *Rapid Prototyp. J.*, 2023, **29**, 2164–2175.
542 G. L. Goh, S. Agarwala, G. D. Goh, H. K. J. Tan, L. Zhao, T. K. Chuah and W. Y. Yeong, *Int. J. Adv. Des. Manuf. Technol.*, 2018, **94**, 1309–1316.
543 Space Exploration: NASA's 3D Printing Vision for Additive Manufacturing Available online: **https://www.zeal3dprinting.com.au/additive-manufacturing-in-space-exploration-nasas-vision-for-3d-printing/**.
544 M. Hoffmann and A. Elwany, *J. Eng. Ind.*, 2023, **145**, 1–70.
545 A. Birmingham, *Overview of NASA Initiatives in 3D Print. Additive manufacturing*, Marshall Space Flight Center, 2014.
546 A. Van Ombergen, F. Chalupa-Gantner, P. Chansoria, B. M. Colosimo, M. Costantini, M. Domingos, A. Dufour, C. De Maria, J. R. Groll, T. Jungst, R. Levato, J. Malda, A. Margarita, C. Marquette, A. Ovsianikov, E. Petiot, S. Read, L. Surdo, W. Swieszkowski, G. Vozzi, J. Windisch, M. Zenobi-Wong and M. Gelinsky, *Adv. Healthcare Mater.*, 2023, **12**, 2300443.